Mississippi State University

Scholars Junction

Theses and Dissertations Theses and Dissertations

5-2-2009

Structural testing of an ultralight UAV composite wing and fuselage

Jutima Simsiriwong

Follow this and additional works at: https://scholarsjunction.msstate.edu/td

Recommended Citation

Simsiriwong, Jutima, "Structural testing of an ultralight UAV composite wing and fuselage" (2009). *Theses and Dissertations*. 4086.
https://scholarsjunction.msstate.edu/td/4086

This Graduate Thesis - Open Access is brought to you for free and open access by the Theses and Dissertations at Scholars Junction. It has been accepted for inclusion in Theses and Dissertations by an authorized administrator of Scholars Junction. For more information, please contact scholcomm@msstate.libanswers.com.

STRUCTURAL TESTING OF AN ULTRALIGHT UAV COMPOSITE WING AND FUSELAGE

By

Jutima Simsiriwong

A Thesis
Submitted to the Faculty of
Mississippi State University
in Partial Fulfillment of the Requirements
for the Degree of Master of Science
in Aerospace Engineering
in the Department of Aerospace Engineering

Mississippi State, Mississippi

May 2009

STRUCTURAL TESTING OF AN ULTRALIGHT UAV COMPOSITE WING AND FUSELAGE

By

Jutima Simsiriwong

Approved:

Rani W. Sullivan
Assistant Professor of Aerospace
Engineering (Major Professor)

Masoud Rais-Rohani
Professor of Aerospace Engineering
(Committee Member)

Thomas E. Lacy Jr.
Associate Professor of Aerospace
Engineering (Committee Member)

Mohamad S. Qatu
Professor of Mechanical Engineering
(Committee Member)

Pasquale Cinnella
Professor of Aerospace Engineering
(Graduate Coordinator)

Sarah A. Rajala
Dean of Bagley College of Engineering

Name: Jutima Simsiriwong

Date of Degree: May 2, 2009

Institution: Mississippi State University

Major Field: Aerospace Engineering

Major Professor: Dr. Rani W. Sullivan

Title of Study: STRUCTURAL TESTING OF AN ULTRALIGHT UAV COMPOSITE
WING AND FUSELAGE

Pages in Study: 124

Candidate for Degree of Master of Science

The details of an experimental investigation focusing on obtaining the static and vibration characteristics of a full-scale carbon composite wing and fuselage structural assemblies of an ultralight unmanned aerial vehicle (UAV) are presented. The UAV has a total empty weight of 155-lb and an overall length of approximately 20.6-ft. A three-tier whiffletree system and the tail fixture were designed and used to load the wing and the fuselage in a manner consistent with a high-g flight condition. A shaker-table approach was used for the wing vibration testing, whereas the modal characteristics of the fuselage structure were determined for a free-free configuration. The static responses of the both structures under simulated loading conditions as well as their dynamic properties such as the natural frequency, damping coefficient and associated mode shapes were obtained. The design and implementation of the static and vibration tests along with the experimental results are presented in this thesis.

DEDICATION

I would like to dedicate this work to my family, especially to my dad.

ACKNOWLEDGEMENTS

Foremost, I would like to thank my major professor, Dr. Rani W. Sullivan, for all her endless guidance and constant support.

I also would like to thank the other members of my committee, Dr. Masoud Rais-Rohani, Dr. Thomas E. Lacy Jr., and Dr. Mohamad S. Qatu for their help in reviewing this thesis. I want to extend my gratitude to the staff at Raspet Flight Research Laboratory, especially John Johnson, Rodney Lincoln, Clay Shires, Phil Trasatti, and Matt Fox, for their support of the testing activity. My appreciation is also extended to the ULSP Structural Analysis Group including Dr. Thomas E. Lacy Jr., Dr. Youngkeon Hwang and John Hutchins.

Furthermore, I would like to express my sincere gratitude to the two important professors, the late Dr. Z. U. A. Warsi and the late Dr. Bruce L. Cain, for their kindhearted and compassionate in teaching.

The funding provided for this study by US Army SMDC under Contract No. DASG60-01-C-0038 is gratefully acknowledged.

TABLE OF CONTENTS

Page

DEDICATION ii

ACKNOWLEDGEMENTS iii

LIST OF TABLES vi

LIST OF FIGURES viii

CHAPTER

1. INTRODUCTION 1
    - 1.1 Background Information 1
    - 1.2 Motivation 3
2. LITERATURE REVIEW 7
    - 2.1 Static Testing 8
    - 2.2 Vibration Testing 9
3. DESCRIPTION OF TEST STRUCTURES 11
    - 3.1 Wing Structure 11
    - 3.2 Fuselage/tail Structure 16
    - 3.3 Material Description 19
4. STATIC TESTING 20
    - 4.1 Wing Assembly Testing 20
        - 4.1.1 Loading Methodology 20
        - 4.1.2 Experimental Set Up 23
        - 4.1.3 Instrumentation 25
        - 4.1.4 Results and Discussion 29

        4.1.4.1 Test Fixture Validation 29
        4.1.4.2 Preliminary Testing..31
        4.1.4.3 Test to Failure 33
  4.2 Fuselage/tail Testing 44
    4.2.1 Loading Methodology...44
    4.2.2 Experimental Set Up 45
        4.2.2.1 Preliminary Testing..47
    4.2.3 Instrumentation 49
    4.2.4 Results and Discussion 52
        4.2.4.1 Centric Loading 52
        4.2.4.1 Eccentric Loading 57

5. VIBRATION TESTING..68

  5.1 Analytical Methodology 68
  5.2 Wing Assembly Testing...71
    5.2.1 Experimental Set Up and Procedure 71
    5.2.2 Data Acquisition System..76
    5.2.3 Results and Discussion 77
  5.3 Fuselage/tail Testing 92
    5.3.1 Experimental Set Up and Procedure 92
    5.3.2 Results and Discussion 96

6. CONCLUSIONS..104

REFERENCES 106

APPENDIX

A. APPARATUS 109

B. LABVIEW PROGRAM...112

C. RESULTS FROM CHORDWISE VIBRATION TESTING OF WING STRUCTURE 118

LIST OF TABLES

TABLE Page

3.1 Laminate definition in structural parts shown in Figure 3.3 [19] 15

3.2 Laminate definition in structural parts shown in Figure 3.4 and 3.5 18

3.3 Physical and engineering properties of structure materials 19

4.1 Load distribution at whiffletree loading stations [19]...23

4.2 Left wing deflection from bending stiffness test 32

4.3 Right wing deflection from bending stiffness test 32

4.4 Percent difference between left and right wing strain readings at 1400 lb 40

4.5 Deflection and strength characteristics of the wing structures 41

4.6 Maximum strain readings at 100 lb centric pull-down loading 56

4.7 Maximum strain readings at 100 lb eccentric pull-down loading..........................60

4.8 Maximum strain readings at 100 lb eccentric push-up loading 63

5.1 List of peak frequencies of in-plane channels of Wing #1 82

5.2 List of peak frequencies of out-of-plane channels of Wing #1.............................83

5.3 List of peak frequencies of in-plane channels of Wing #2 84

5.4 List of peak frequencies of out-of-plane channels of Wing #2.............................85

5.5 Vibration characteristics of Wing #1 91

5.6 Vibration characteristics of Wing #2 91

5.7 Vibration characteristics and observed mode shape of fuselage/tail structure 103

A.1 Static testing apparatus 110

A.2 Vibration testing apparatus 111

C.1 List of peak frequencies of in-plane channels of Wing #1 120

C.2 List of peak frequencies of out-of-plane channels of Wing #1............................121

C.3 List of peak frequencies of in-plane channels of Wing #2 123

C.4 List of peak frequencies of out-of-plane channels of Wing #2............................124

LIST OF FIGURES

FIGURE Page

1.1 Cad model of UAV with retracted engine [4]..2

1.2 Illustration of the structure’s response due to wind gust 5

3.1 Wing structural components [4]..12

3.2 Top view of the spar-spar and wing-fuselage attachment region [4].....................13

3.3 Close-up view of individual members near wing root [4] 14

3.4 Fuselage/vertical stabilizer structural components 17

3.5 Fuselage/vertical stabilizer structural components (a) vertical tail close-up (b) wing lift pins close-up 17

4.1 Whiffletree system for wing static testing [19]...22

4.2 UTF and saddle fixture set up 24

4.3 Strain and deflection gauge locations at various wing stations [19]......................27

4.4 Left wing after instrumentation set up 28

4.5 Strain response from carry-through structure a) flight test at 80 KIAS, 4-g pull up maneuver (b) static test..31

4.6 Wing deflection at (a) DS1 of the right and left wing (b) DS2 and DS3 of the left wing 34

4.7 Axial and shear strains at GS1 of the right and left wing (a) fore, (b) main, (c) aft spars..36

4.8 Axial and shear strains at GS2 of the right and left wing main spars....................37

4.9 Comparison of strains at GS1 and GS2 of left wing main spar 38

4.10 Axial and shear strains at GS3 of the right and left wing (a) fore, (b) main, (c) aft spars 39

4.11 Right wing at (a) the limit load, (b) the design limit load, and (c) failure 42

4.12 Wing structure at failure (a) general mode (b) specific location 43

4.13 Fuselage loading configuration 45

4.14 Test fixture for F_1 loading 46

4.15 Test fixture for F_2 loading 46

4.16 Strain gauge location relative to the fiber tows 47

4.17 Strain gauge placement of preliminary testing (a) cross-sectional view of gauges (b) fuselage station 48

4.18 Preliminary static testing results from strain gauges located at gauge station shown in Figure 4.17 49

4.19 Strain gauge configuration (a) gauge placement showing the rosette gauges and the uniaxial gauges (b) cross-sectional view of strain gauge locations at fuselage station 50

4.20 Fuselage strain gauge stations 50

4.21 F_2 push-down loading methodology 51

4.22 F_2 pull-up loading methodology 52

4.23 Strain measurement direction of test structure 53

4.24 Strain measurements from centric pull-down loading at (a) GS2, (b) GS, (c) GS4, and (d) GS5 54

4.25 Measurements of (a) ε_x ,(b) ε_y , and (c) γ_{xy} from centric pull-down loading 55

4.26 Normal strain (in x-direction) along the length 57

4.27 Strain measurements from eccentric pull-down loading at (a) GS2, (b) GS3, (c) GS4, and (d) GS5 58

4.28 Measurements of (a) ε_x ,(b) ε_y , and (c) γ_{xy} from eccentric pull-down loading......59

4.29 Strain measurements from eccentric push-up loading at (a) GS2, (b) GS3, (c) GS4, and (d) GS5 61

4.30 Measurements of (a) ε_x ,(b) ε_y , and (c) γ_{xy} from eccentric push-up loading..........62

4.31 Comparison between the left longitudinal strains from pull-down and the right longitudinal strains from push-up loading..64

4.32 Comparison between the right transverse strains from pull-down loading and the left transverse strains from push-up loading...65

4.33 Comparison between the right shear strains from pull-down loading and left shear strains from push-up loading..66

5.1 Linear model for a FRF...69

5.2 Frequency bandwidth of half power points method 71

5.3 (a) Support fixture (b) Track system for in-plane excitation (c) Track system for out-of-plane excitation 72

5.4 Wing vibration test fixture for (a) in-plane excitation (b) out-of-plane excitation 73

5.5 Vibration test set up with accelerometers location (a) Wing #1 (b) Wing #2 75

5.6 Vibration data acquisition system...76

5.7 Frequency spectrum based on in-plane (chord-wise) acceleration measurements at accelerometer location (a) A1, (b) A2, (c) A5, and (d) A6 of Wing # 1............78

5.8 Frequency spectrum based on out-of-plane acceleration measurements at accelerometer location (a) A1, (b) A2, (c) A5, and (d) A6 of Wing # 1 79

5.9 Frequency spectrum based on in-plane (chord-wise) acceleration measurements at accelerometer location (a) A1, (b) A2, (c) A5, and (d) A6 of Wing # 2............80

5.10 Frequency spectrum based on out-of-plane acceleration measurements at accelerometer location (a) A1, (b) A2, (c) A5, and (d) A6 of Wing # 2 81

5.11 Vibration modes of wing structures at selected natural frequencies......................86

5.12 Vibration modes of Wing #2 at selected natural frequencies using (left) double integration method and (right) FRF method 89

5.13 Fuselage vibration test set up 92

5.14 Fuselage vibration test fixture 93

5.15 Fuselage vibration testing configuration #1 95

5.16 Fuselage vibration testing configuration #2 95

5.17 Fuselage vibration testing configuration #3 96

5.18 Fuselage vibration testing configuration #4 96

5.19 Frequency response function of accelerometer A19 97

5.20 Displacement direction of the test structure 98

5.21 Frequency spectrums for A1, A8, and A10 in the (a) x-direction and (b) y- direction using (c) the coordinate system 99

5.22 Frequency spectrums of A14 and A16 in the (a) x-direction and (b) z- direction using (c) the coordinate system 100

5.23 Frequency spectrums of A17, A18, and A19 in (a) x direction and (b) z-direction using (c) the coordinate system 101

5.24 Red-mode shape at (a) 13.5 Hz (b) 24.6 Hz (c) 36.3 Hz (d) 45.4 Hz Black-mode shape at 0 Hz 102

B.1 LabVIEW program for static testing of wing structure (front panel) 113

B.2 LabVIEW program for static testing of fuselage structure (front panel) 114

B.3 LabVIEW program for static testing (block diagram) 115

B.4 LabVIEW program for vibration testing (front panel) 116

B.5 LabVIEW program for vibration (block diagram) 117

C.1 Frequency spectrum based on out-of-plane acceleration measurements at accelerometer location (a) A1 and (b) A5 of Wing #1 119

C.2 Frequency spectrum based on in-plane (chord-wise) acceleration measurements at accelerometer location (a) A1 and (b) A5 of Wing #1 119

C.3 Frequency spectrum based on out-of-plane acceleration measurements at accelerometer location (a) A1 and (b) A5 of Wing # 2 122

C.3 Frequency spectrum based on in-plane (chord-wise) acceleration measurements at accelerometer location (a) A1 and (b) A5 of Wing # 2............122

CHAPTER 1

INTRODUCTION

Unmanned aerial vehicles (UAVs), also known as unmanned aircraft systems, have gained much attention in recent years in military and civil aviation as well as scientific research. UAVs have found applications for intelligence, surveillance, and aerial reconnaissance missions, particularly those which are impractical for manned aircraft. Additionally, UAVs have been used for homeland security needs and as aerial cell towers during domestic disaster relief operations [1]. The use of UAVs has been expanded and integrated into the daily operations, such as searching for lost hikers, tracking flee criminals, aiding wildfire-fighting efforts, etc. UAVs have lower development and maintenance costs than manned aircrafts. As a result, there has been a rapid growth in design, development, and production of different classes of UAVs ranging from the short-range, remotely-piloted, micro aerial vehicles to the large, jet-powered and autonomous vehicles [2, 3].

1.1 Background Information

The aircraft of interest in this study is part of a larger effort to develop an all composite unmanned ultra-light sensor platform which integrates carbon-fiber reinforced polymer (CRP) composite sailplane and the unmanned systems technology. It is designed to improve U.S. surveillance and communication capabilities for battlefield and border-patrol operations. This aircraft is categorized as a long endurance UAV with high attitude capabilities and it is expected to operate initially at altitudes of 10,000 to 20,000-feet. While most power is provided by thermal updrafts and other atmospheric winds (sailplane features), the aircraft has a small power plant to keep it aloft for long periods of time when needed. Figure 1.1a shows a Computer Aided Design (CAD) model of the high-performance-sailplane inspired ultralight UAV design.

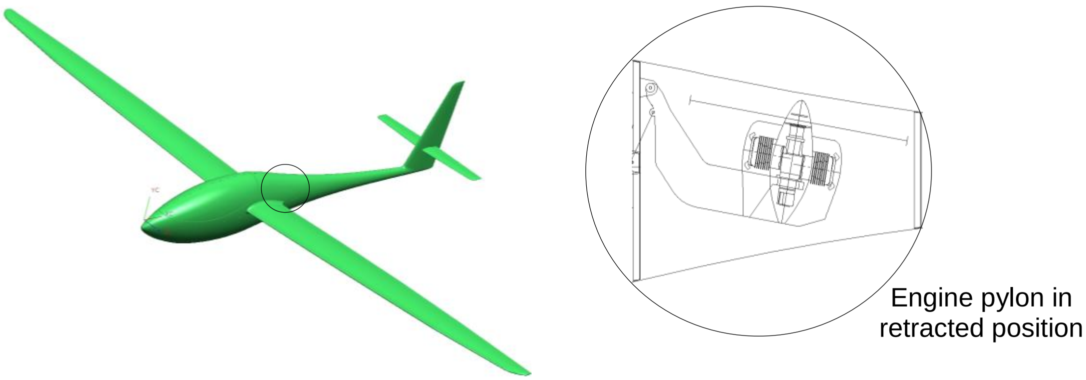

(a) (b)

Figure 1.1

CAD model of UAV with retracted engine [4]

Due to the use of advanced composite materials, this aircraft has a lightweight airframe structure, which allows for a much larger and heavier payload. It can accommodate an autonomous flight control system, generic sensor package, and propulsion system. The propulsion is provided by a single retractable reciprocating engine mounted on a pylon behind the cockpit (sensor bay). The CAD model of the UAV with the propulsion system in retracted position is shown in Figure 1.1b. The fuel supply to the engine comes from sealed tanks inside the wings. The aircraft consists of four primary structures including the fuselage body with an integrated vertical stabilizer, a horizontal stabilizer, and the right and left wings.

1.2 Motivation

Although the UAV in this study falls under the ultralight category of aircraft with an empty weight of approximately 155 lb, its structural components were designed based on FAR Part 23 airworthiness standards for a normal category general aviation airplane. According to Federal Aviation Administration (FAA) regulations, a newly designed aircraft such as this UAV must meet or exceed the required structural specifications, obtained by either analysis and/ or testing. Typically, the overall structural testing is categorized by four stages: component testing, full-scale aircraft static testing, fatigue testing, and flight testing. In this study, a series of tests are performed to measure the static and vibration responses of the aircraft components (i.e., wing and fuselage).

A static test is generally performed by gradually applying the load to the test structure to evaluate the stength and stiffness characteristics and to examine the load paths or the failure modes of the structure. The effective static test is essential, especially to aircraft design, to predict the structural capability necessary to withstand the required load or the maximum expected load. The static test is also performed to ensure the established factor of safety, which is applied to obtain the ultimate load condition, which accounts for structural flaws such as material defects or engineering calculation and manufacturing error. Unlike metal alloy structures, in which the yield point of the metal signifies some yielding prior to final failure, composite structures with brittle fiber systems (e.g., carbon) exhibit minimal or no yielding. Therefore, the safety margin must be established accurately since the failure is usually catastrophic when the ultimate strength is reached.

As part of this effort, the static structural testing to failure is performed on a full-scale composite wing assembly. Each wing is instrumented with 48 strain gauges as well as four deflection gauges to measure normal and shear strains along with the deflection of each wing at critical locations. A whiffletree system is designed and used to simulate the in-flight loads, which are based on a load distribution and intensity corresponding to a high-g (pull-up) maneuver condition.

Aircraft ground testing also includes vibration tests, which provide key information for determining the aeroelastic response of the vehicle. Aircraft components can be damaged or destroyed from flutter or air flow-induced vibration of the wings, horizontal surfaces, or vertical surfaces of the aircraft. As shown in Figure 1.2, dynamic loads due to wind gust can lead to dynamic aeroelastic instability (flutter), which can lead to a catastrophic failure. Knowledge of an aircraft’s dynamic characteristics, such as the vibration frequency, damping and associated mode shapes, is necessary in determining key parameters such as the aircraft, which are used to determine an aircraft’s flight envelope.

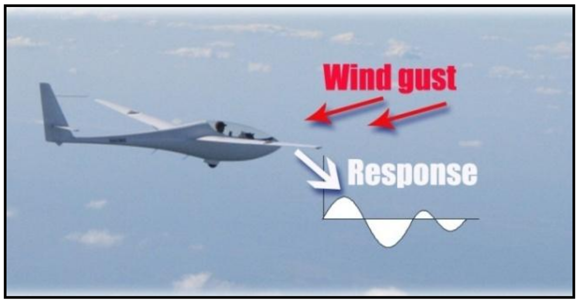

Figure 1.2

Illustration of the structure's response due to wind gust

For this study, vibration testing was performed on the left composite wing and the fuselage of the UAV to determine the corresponding modal characteristics. A slightly modified version of the wing without the aileron cutout was tested using a shaker-table apparatus, whereas the modal characteristics of the fuselage structure were determined for a free-free configuration, which was simulated by suspending the test structure from its wing attachment points through the use of springs. A series of dual-axis accelerometers were mounted at various locations on the wing to record in-plane and out-of-plane accelerations and measurements of its vibration frequencies and mode shapes. For the fuselage vibration test, a centrally located shaker system was used to induce vertical oscillations in the fuselage structure, which was also instrumented with a series of dual-axis accelerometers.

Typically, structural test programs comprise both experimental testing and simulation. The simulation results can guide the experiments while the experimental data can be used to adjust the finite element model and validate its predictions. Although finite element simulations were conducted by others as part of the overall project, this study focuses on the procedure and results obtained from the ground testing of the UAV wing assembly and fuselage structure. A literature review of ground test methods and procedures of aircraft components and full aircraft is presented in Chapter 2. Detailed description of the individual test articles (wing and fuselage/tail structure) including structural geometry, component layout, and material system is given in Chapter 3. Testing methodology and results from the static and vibration testing are presented in Chapters 4 and 5, respectively, followed by conclusions in Chapter 6.

CHAPTER 2

LITERATURE REVIEW

The availability and affordability of high quality test and data acquisition equipment have made it possible to conduct large scale component testing on low budget test programs. Key objectives of structural test programs typically include the following: determining the structure's strength and stiffness characteristics and dynamic response, validating the fabrication methodology, revealing structural anomalies, and refining and validating a numerical model. In this study, a series of experiments were performed to determine the static response and vibration characteristics of the wing assembly and fuselage/vertical tail structures of an ultralight UAV.

Experimental measurements related to structural testing were initially established by Robert Hooke (1635-1703), who conducted experiments to determine the force-deformation relationships in order to describe the elastic behavior of structures [5]. Over the years, a variety of structural tests for both static and vibration characterization have been developed to obtain various response characteristics of the structure under load.

2.1 Static Testing

For experimental measurements of strength and stiffness characteristics of structures, it is imperative that the test article be subjected to the types and magnitudes of loadings that the structure would typically experience. In the case of aircraft structures, the wings must support the severe aerodynamic loads, which is encountered in a critical flight condition. Lead shot bags can be used to apply a distributed load, but often, they are impractical when testing large components to failure. An alternative method to simulate load distributions is to use a device known as a whiffletree.

Often used in structural testing in the aerospace industry, the whiffletree has been used for simulating distributed loads on aircraft components, full-scale air vehicles, and in wind turbine blade testing [6-10]. Depending upon the level of sophistication and intricacy of the whiffletree design, it is possible to fairly accurately simulate the in-flight loads experienced by the structure. For such a system to be used, it is necessary to ensure that the number of point loads employed is sufficient to closely simulate the condition of distributed loading conditions [11]. Smith [6] effectively used a five-tier whiffletree system to evaluate the strength of an ultralight aircraft. Ma and Shiue [7] used the whiffletree device in the static bench testing of an airfoil elevator, where two actuators were utilized to simulate various loading conditions. Using a two-tier whiffletree system, Kosmatka and Valdes [10] did static testing of a full scale UAV hunter composite wing with a 415 in. wing span. For this study, a three-level whiffletree sytem was designed using basic mechanics principles to simulate a distributed load on the wing structure in a safe and effective manner. The load distribution on the wing assembly was determined from the vortex lattice method for the ultimate load condition [12].

2.2 Vibration Testing

Modal or vibration testing has become one of the standard test procedures in the design and development of most engineering systems that may experience dynamic loading. It is most often performed to determine modal characteristics of structures in order to eliminate or reduce unwanted vibrations.

Modern experimental modal analysis was established in the 1960s, with the theoretical formulation of vibration test methodologies and the commercial availability of measuring equipment for dynamic testing [13]. During this period, two methodologies, known as phase resonance and phase separation method, were developed. Phase resonance methods were widely used in the aerospace industry by utilizing multiple sine signals to excite the aircraft into a normal (resonance) mode of vibration. This was achieved by either adjusting the phase or frequency of a set of two or multiple shakers. This method became known as the forced normal method and a good review of this approach can be founded in Ref. [14]. The phase separation method is based on frequency response functions, which are measured either at a discrete frequency or over a range of frequencies. Frequency response functions are commonly used in modal analysis where the vibration response of the structure is measured relative to the force input. The phase separation method is still widely used in various applications including automotive, aerospace as well as machine tool industries. Kennedy and Pancu provide a good description of the phase separation method [15].

Ground vibration testing of full-scale air vehicles, as well as aircraft components, are generally performed using steady-state or transient (impact or burst random) excitation functions [16]. Steady-state function vibration testing is used extensively, particularly in military applications, because it provides continuous frequencies and greater dynamic ranges. Some examples of implementing the steady-state function is the slow sine-sweep and sine-dwell techniques, which have been used in the modal testing of many aircraft structures such as the F-18 Fighter and X-31 thrust vectored airplane [17]. Although the impact excitation technique is used effectively in the vibration testing of small structures, it oftentimes does not provide sufficient excitation to obtain all the modes of interest [18].

In this study, the phase separation method was used because of the availability of the single-input single-output test capability. The steady sine excitation function is incorporated into the test to fully identify the modal characteristics of the structure within its operational frequency range. A shaker table approach was used for the vibration testing of a single wing and a free-free configuration was simulated for the vibration testing of the fuselage body.

CHAPTER 3

DESCRIPTION OF TEST STRUCTURES

All aircraft structural components are made of carbon-fiber reinforced polymer composite materials in the form of woven fabrics as well as uniaxial prepreg fabrics. Individual structural parts are fabricated using precision molds and cured under vacuum at elevated temperature. Low-cost manufacturing is achieved through reduction in part count and a fabrication process that does not require the use of an expensive autoclave. Due to the composite construction and design of the UAV, a shorter wingspan, thinner wing profile, and overall weight reduction is obtained.

3.1 Wing Structure

Typically, aircraft are designed with long wingspan to decrease induced drag. However, the carbon composite wing in this study utilizes five different airfoil shapes tailored to the local span requirement such that the maximum lift to drag ratio is achieved. The wing, weighing 35 lb, consists of three primary structures: a root rib, upper and lower foam core sandwich skin, and the spars, as shown in Figure 3.1. The wing has a length of 217 in., measured from the fuselage centerline to the wing tip. The maximum airfoil thickness of 4 in. is measured at the root section, with a root chord of 29 in.

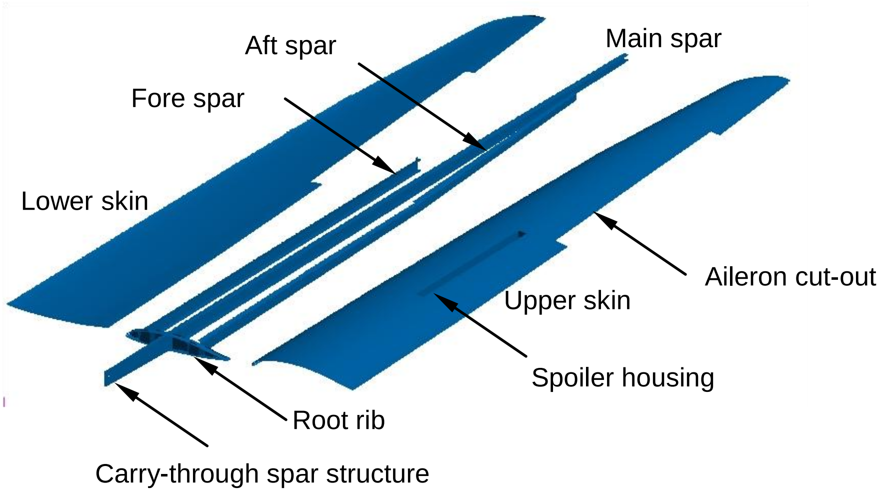
Aft spar
Main spar
Fore spar
Lower skin
Aileron cut-out
Upper skin
Spoiler housing
Root rib
Carry-through spar structure

Figure 3.1

Wing structural components [4]

The three spars (fore, main, and aft) have a channel cross-section with a web dimension of 2.5 in., 3.2 in., and 1.8 in., located at 15%, 40%, and 70% chord, respectively. Unlike the fore and aft spars, the main spar extends from the wing tip to the inside of the fuselage, forming a carry-through structure. As depicted in Figure 3.2, the main spar from each wing transitions at approximately 3.5 in. from the root rib to a tapered solid rectangular cross-section to form the carry-through structure that provides the wing bending rigidity. The shear load transfer is provided by a pair of steel lift pins which create the root rib-fuselage skin interconnection. All spars are straight with the exception of the aft spar, which is straight up to the aileron cutout and then kinks forward to accommodate the aileron placement. Both the aileron and spoiler are removed prior to the vibration and static testing, although their housing can be seen in Figure 3.1.

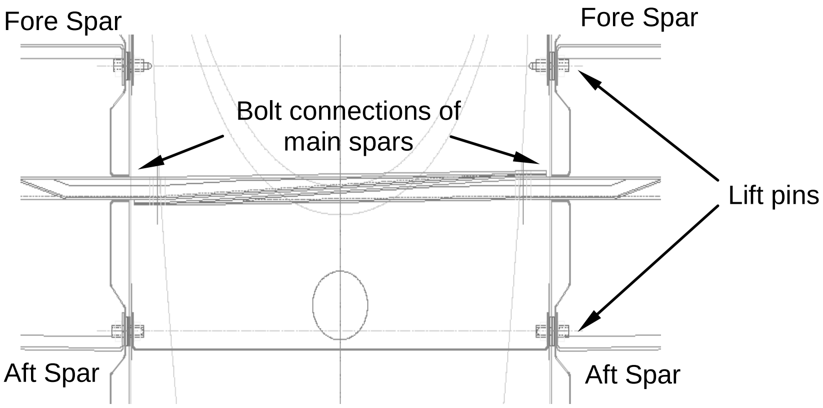

Figure 3.2

Top view of the spar-spar and wing-fuselage attachment region [4]

All structural members of the wing are made of carbon-fiber reinforced polymer (CFRP) composite materials in the form of woven prepreg fabrics (T700G by Toray Composites America Inc.), and unidirectional prepreg fabrics (T700S by Toray Composites America Inc.), with properties given in Table 3.3. Shown in Figure 3.3, the spars and root rib are fabricated from woven graphite–epoxy fabric, whereas the upper and lower wing skins are made of sandwich construction with woven-fabric graphite-epoxy face sheets and a 0.125 in. thick, low-density foam core (Divinycell® HT 50 by DIAB Inc.). The foam core extends over the entire wing surface to about 1.5 in. from the front, side, and rear boundaries. The wings contain no ribs or stringers except a root cap.

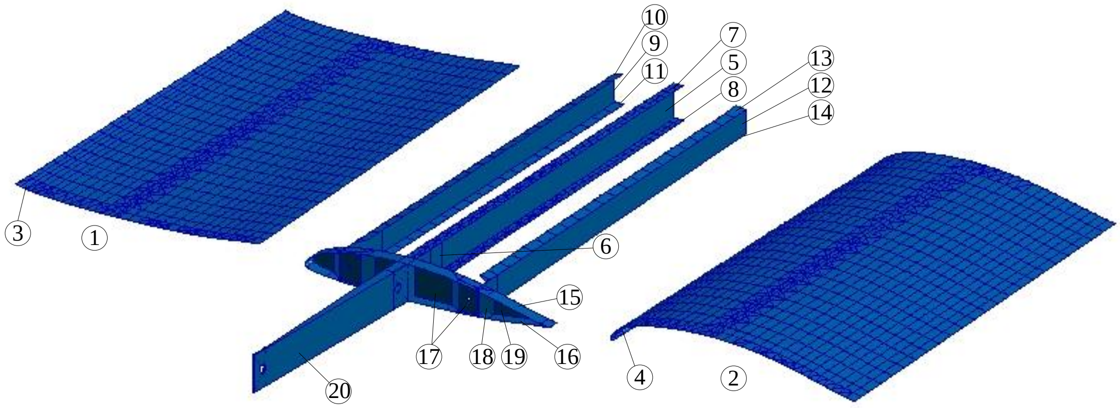

Figure 3.3

Close-up view of individual members near wing root [4]

The laminate ply pattern for individual members near the wing root is given in Table 3.1, with the corresponding members identified in Figure 3.3. As indicated in the table, the flanges of the main spar channel contain the maximum number of plies, with a total of 125 plies and 95 plies for top and bottom flanges, respectively. All structural members are individually fabricated using precision molds and cured under vacuum at elevated temperature prior to being adhesively bonded in an assembly jig. The pair of steel lift pins, shown in Figure 3.2, is mounted on the root rib after the rib fabrication.

Table 3.1

Laminate definition in structural parts shown in Figure 3.3 [19]

Part No.	Description[a]	No. of Plies	Ply Pattern[b]
1	Bottom skin	5	$(45/0/\text{foam}/0/45)_T$
2	Top skin	5	$(45/0/\text{foam}/0/45)_T$
3	Leading edge	4	$(45/0)_s$
4	Leading edge	4	$(45/0)_s$
5	MS web	21	$(0/45)_9/45/45/45$
6	MS at wing root	8	$(45/0/0/45)_s$
7	MS comp.cap	126	$45/45/45/[u0]_4/0/[u0]_{10}/45/[u0]_6/0/[u0]_{12}/45/[u0]_{20}/0/45/[u0]_{13}/0/45/[u0]_{10}/0/45/[u0]_{10}/0/45/[u0]_{10}/0/45/[u0]_5/0/45/0/45$
8	MS ten. Cap	96	$45/45/45/[u0]_4/0/[u0]_6/45/[u0]_4/0/[u0]_8/45/[u0]_{14}/0/45/[u0]_6/0/45/[u0]_6/0/45/[u0]_6/0/45/[u0]_{12}/0/45/[u0]_4/0/45/0/45$
9	FS web	12	$45/0/0/45/45/0/0/45/45_4$
10	FS comp. cap	8	$(45/0/0/45)_s$
11	FS ten. Cap	8	$(45/0/0/45)_s$
12	AS web	12	$(45/0/0/45)_2/45_4$
13	AS comp. Cap	8	$(45/0/0/45)_s$
14	AS ten. Cap	8	$(45/0/0/45)_s$
15	Root rib top	12	$(45/0/0/45/45/0)_s$
16	Root rib bottom	12	$(45/0/0/45/45/0)_s$
17	Root rib web	12	$(45/0/0/45)_2/45_4$
18	Root rib/ AS connection	8	$(45/0/0/45)_s$
19	Root rib web	4	$(45/0)_s$
20	Stub spar	8	$(45/0/0/45)_s$

[a] MS = Main spar, FS = Fore spar, AS = Aft spar

[b] 45 = ±45 fabric, 0 = 0/90 fabric, and [u0] = unidirectional ply

3.2 Fuselage/tail Structure

The fuselage body is comprised of left and right shells plus two frames, which are located behind the sensor bay that encloses the propulsion system. The vertical stabilizer is an integral part of the fuselage whereas the horizontal stabilizer is mounted over a circular tube and two short rods protruding through the vertical stabilizer. The fuselage/tail body measures 247 in. from the fuselage nose to the trailing edge of the vertical stabilizer. From its root to its tip, the vertical stabilizer measures 50.2 in. with a root chord dimension of 12.9 in. and maximum airfoil thickness of 4.4 in. at the root chord.

The fuselage/ tail structure is made from prepreg materials utilizing both unidirectional and woven carbon-fiber reinforced polymer composite fabrics. The semimonocoque fuselage structure is of multi-ply laminate construction except in the area around the sensor bay (denoted as region 10 in Figure 3.4), which is of sandwich construction using a 0.25 in. thick honeycomb (Divinycell® HT 50 by DIAB Inc.). The skins of the vertical stabilizer are also of sandwich construction using 0.125 in. thick, low density foam core. The laminate ply pattern, for the individual members identified in Figure 3.4-3.5, is given in Table 3.2 and the material properties of the CFRP fabric are given in Table 3.3

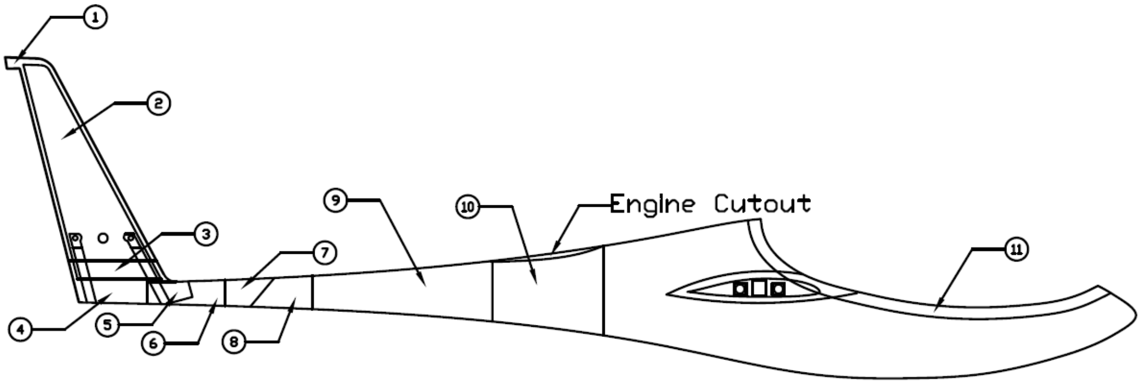

1
2
9
10
Engine Cutout
3
7
11
4
5
6
8

Figure 3.4

Fuselage/vertical stabilizer structural components

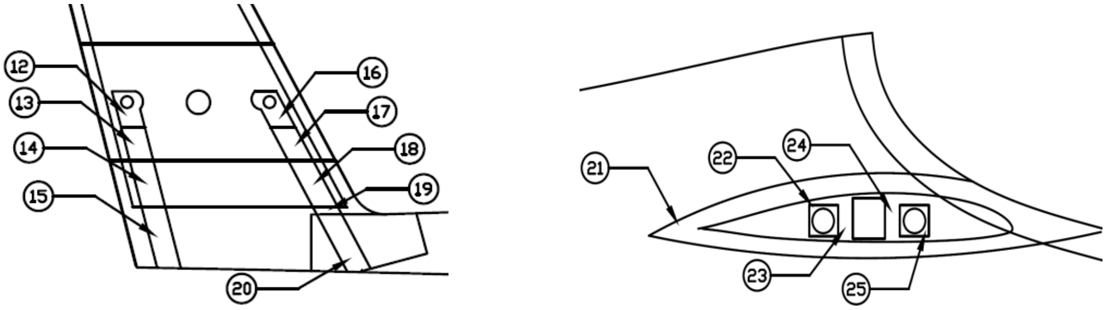

12
13
14
15
16
17
18
19
20
21
22
24
23
25

(a) (b)

Figure 3.5

Fuselage/vertical stabilizer structural components (a) vertical tail close-up
(b) wing lift pins close-up

Table 3.2

Laminate definition in structural parts shown in Figures 3.4 and 3.5

Part No.	**No. of Plies**	**Description**[a]	**Stacking Sequence**[b]
1	4	Upper VT	$(50/15)_s$
2	5	Main VT	$(50/\text{foam}/15/15/50)_T$
3	6	VT Overlap 1	$(50/\text{foam}/15/0/15/50)_T$
4	5	VT Overlap 2	$(50/15/0/15/50)_T$
5	6	AFT Fuselage Overlap 1	$(50/0/15/0/15/50)_T$
6	5	AFT Fuselage Overlap 2	$(50/0/15/0/50)_T$
7	5	AFT Fuselage Overlap 3	$(50/0/15/0/45)_T$
8	4	AFT Fuselage	$(50/0)_s$
9	4	Main Fuselage	$(45/0)_s$
10	9	Engine Cutout Reinforcement	$(45/0_2/45/\text{HC}/45/0_2/45)_T$
11	4	Canopy Cutout Reinforcement	$(45_3/0_2/45)_T$
12	15	AFT VT LP Reinforcement 1	$(50/\text{foam}/15/15/50/0/45_3/0_2/45_3/0)_T$
13	12	AFT VT LP Reinforcement 2	$(50/\text{foam}/15/15/50/0/45_2/0/45_2/0)_T$
14	13	AFT VT LP Reinforcement 3	$(50/\text{foam}/15/0/15/50/0/45_2/0/45_2/0)$
15	12	AFT VT LP Reinforcement 4	$(50/15/0/15/50/0/45_2/0/45_2/0)_T$
16	11	Front VT LP Reinforcement 1	$(50/\text{foam}/15/15/50/0/45/0/45/0/45)_T$
17	8	Front VT LP Reinforcement 2	$(50/\text{foam}/15/15/50/45/0/45)_T$
18	9	Front VT LP Reinforcement 3	$(50/\text{foam}/15/0/15/50/45/0/45)_T$
19	8	Front VT LP Reinforcement 4	$(50/15/0/15/50/45/0/45)_T$
20	9	Front VT LP Reinforcement 5	$(50/0/15/0/15/50/45/0/45)_T$
21	8	Wing Root	$(45/0/0/45)_s$
22	15	AFT Wing LP Reinforcement	$(\text{steel}/0/45_2/0/45/0/45_2/30/60/0_3/45)$
23	14	AFT SS Reinforcement	$(0/45_2/0/45/0/45_2/30/60/0_3/45)_T$
24	15	Front SS Reinforcement	$(45/0/45_2/0_3/45_2/30/60/0_3/45)_T$
25	16	Front Wing LP Reinforcement	$(\text{steel}/45/0/45_2/0_3/45_2/30/60/0_3/45)_T$

[a] VT = vertical tail, LP = lift pin, SS = stub spar

[b] $\theta = \pm\theta$ fabric and HC = honeycomb core

3.3 Material Description

Both wing and fuselage/ tail structures are fabricated using prepreg composite materials to ensure the consistency of fiber volume as well as to provide smoother overlaps when compared to the wet layup fabrication method. The Divinycell foam and honeycomb core are incorporated in some structural members such as the wings and horizontal stabilizer skin to provide additional stiffness. All parts are bonded with Loctite Aerospace Hysol adhesive. The properties of the materials used in both wing and fuselage/tail structure are shown in Table 3.3.

Table 3.3

Physical and engineering properties of structural materials

Material Property	**Woven Fabric**[1]	**Unidirectional Fabric**[1]	**Divinycell Foam**[2]	**HC**
E_{11}, psi	8.03x10^{6}	1.73x10^{7}	1.233x10^{4}	3.50x10^{3}
E_{22}, psi	8.03x10^{6}	1.35x10^{6}	1.233x10^{4}	3.50x10^{3}
G_{12}, psi	6.10x10^{5}	6.10x10^{5}	1.233x10^{4}	5.00x10
G_{13}, psi	6.10x10^{5}	6.10x10^{5}	2.76x10^{3}	5.80x10^{3}
G_{23}, psi	6.10x10^{5}	6.10x10^{5}	2.76x10^{3}	2.00 x10^{4}
ν_{12}	3.00x10^{-2}	3.10x10^{-1}	3.20x10^{-1}	5.00x10^{-1}
ρ, lb/in^{3}	1.40x10^{-4}	1.427x10^{-4}	4.65x10^{-6}	4.49x10^{-6}

[1]Manufactured by Toray Composites America Inc. and [2] DIAB Inc.

CHAPTER 4

STATIC TESTING

A whiffletree system was designed and used for static loading of the wing structure with a distribution based on a high-g flight condition. The wing was loaded incrementally beyond the limit and design ultimate loads to the point of structural failure**.** Utilizing the tail loading fixture, both symmetric and non-symmetric loadings were applied to the fuselage/tail structure. Load-deflection and load-strain data were collected and examined.

4.1 Wing Assembly Testing

4.1.1 Loading Methodology

Since the wings constitute the majority of the aircraft lifting surface when compared to other lifting surfaces, such as the horizontal stabilizer, static testing was performed on the wing assembly. Two plausible critical flight loading conditions were examined. Corresponding to FAR 23.341 criteria [20], the first loading condition occurs when the aircraft is subjected to symmetrical vertical gusts in level flight. As a result, the aircraft withstands loads resulting from either positive (up) or negative (down) gusts on each lifting surface. The next critical loading condition corresponds to a high-g pull-up maneuver. Based on analytical calculations for both cases, the latter condition is found to generate the most aerodynamic load on the wings and therefore chosen as the loading condition for the static testing of the wings.

Due to the unavailability of aerodynamic load data for this aircraft, the vortex lattice method (VLM) was utilized to generate the span and chord-wise pressure distributions on a rigid wing model [4]. In the VLM approach, the lifting surface is assumed to be thin (neglecting the effect of airfoil thickness on aerodynamic forces) and divided into small elements. The continuous distribution of bound vorticity, representing the uniform flow on the wing, is then replaced by a finite number (lattice) of discrete vortices located at each quarter chord of the small lifting element. The angle of attack is assumed to be small and can be simplified using the small angle approximation [12]. In this study, the nearly elliptical lift distribution was divided into four piecewise-linear sections on each wing and the statically equivalent resultant forces applied at the spanwise loading stations.

A three-level whiffletree system, shown in Figure 4.1, was designed and implemented to simulate the load distribution obtained from the VLM analysis [4]. As can be seen, this fixture allows for the application of a distributed load although the actual load is applied at a single location. As the level of intricacy of the whiffletree increases, the level of accuracy also increases. In this way, the in-flight loads experienced by the structure can be simulated in an accurate and effective manner. For this reason, the whiffletree is commonly used in large component structural testing, especially within the aerospace industry.

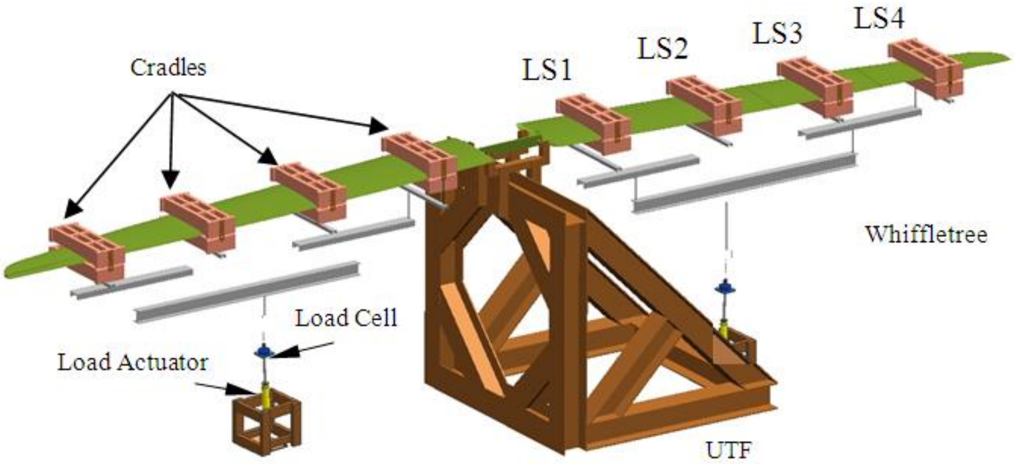

Figure 4.1

Whiffletree system for wing static testing [19]

Table 4.1 lists the load ratios for the limit load (3.8-g) and the ultimate load (5.7-g) conditions. The limit load is the maximum load that the structure may experience during service without producing any permanent deformations whereas the ultimate load or design load is the load carried by the structure up to failure. The conditions are computed based on a gross estimated takeoff weight of 450 lb, with the limit load condition (LLD) and the ultimate load condition (ULD) being equivalent to 855 lb and 1283 lb on each wing, respectively.

Table 4.1

Load distribution at whiffletree loading stations [19]

	LS1	**LS2**	**LS3**	**LS4**
Location (from the fuselage centerline), in	38.5	86.5	134.6	182.6
Load ratio	0.31	0.28	0.23	0.18
LLD, lb	263	239	201	153
ULD, lb	394	359	301	229

Prior to the static test, a comparison study of a box beam under two loading conditions was performed using a finite element model to verify the accuracy of the whiffletree design by Y. Hwang (Private communication). The deflection response of the two cases, one under a distributed load and another under a statically equivalent discretized load applied at station LS1 through LS4, revealed only a 1.2% difference, thereby validating the whiffletree design [4].

4.1.2 Experimental Set Up

The wings are mounted on the universal test fixture (UTF), as shown in Figure 4.1, in an inverted position to facilitate load application in a downward direction using the three-tier whiffletree system. The downward loading requires careful consideration of the structural weight (wings and whiffletree components) as well as the magnitude, direction, and location of the force exerted by the load actuator. As shown in Figure 4.2, both wings are supported by a saddle fixture that is mounted at the center of the top member of UTF. The saddle fixture is designed to resemble the fuselage interface geometry at the wing connection region; therefore, the same technique which is used to connect the wings to the fuselage (by a pair of lift pins at each side of the fuselage) is also used to secure the wings to this fixture. Both wings are bolted together at the center of their stub spars.

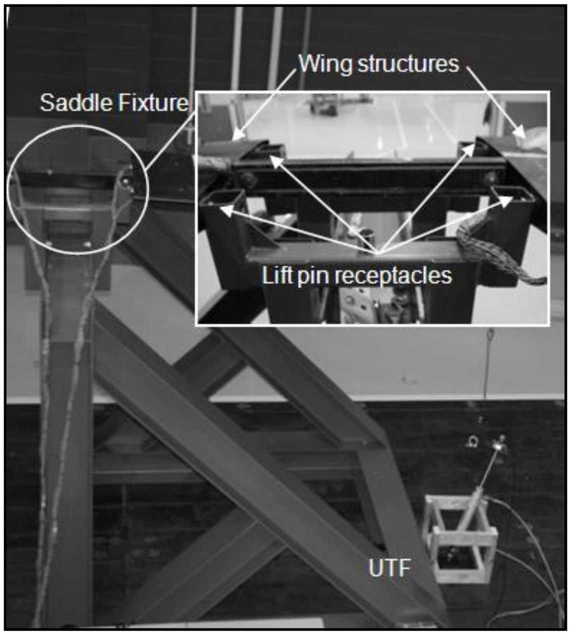

Figure 4.2

UTF and saddle fixture set up

Once the wings are secured to the test fixture, the loading cradles are placed at each loading station, LS1 through LS4 (see Figure 4.1). A loading cradle consists of a set of top and bottom cradles that are fabricated to match the wing contour at the contact surface and then bolted together to prevent slippage at higher loads. These cradles closely match the airfoil shape at the contact surface and are bolted together to prevent slippage during loading of the wing. The top half of each cradle rests on 1 in. wide wooden slats, placed over and near each wing spar in order to distribute the load to prevent local damage to the wing skin. The top cradles are placed on 1 in. thick wooden strips which rest on a non-slip pad. The wooden strips are placed over and around the wing spars to prevent local damage during testing.

Steel connectors are used to connect all levels of the three-tier whiffletree. Aluminum channel sections are used for the first and second tier and a single aluminum I-beam is used as the third tier of the whiffletree. The load actuator is mounted to a base support on the laboratory floor via a ball bearing to allow for rotation of the loading assembly as the wing structure deforms. A steel turnbuckle connects the I-beam at the resultant force location to the load cell. Since the actuator’s maximum stroke is insufficient to produce failure in the structure, the steel turnbuckle pre-loads the assembly to limit load, leaving the actuator to provide the additional load required to induce failure. Each actuator is manually controlled by individual hand pumps. All components of the whiffletree system are designed to withstand a maximum resultant force of 2500 lb per wing.

4.1.3 Instrumentation

A total of 48 strain gauges are installed at the five stations, GS1 through GS5, along the wing as shown in Figure 4.3. The installation of the strain gauges was conducted by the technician prior to the completion of the wings. While the position of GS3 is identical for both wings, those of GS1 and GS2 are not. Therefore, the average dimensions of gauge station GS1 and GS2 for the right and left wings are shown in this figure. Both axial strain gauges and rosette strain gauges are mounted at each station to measure the normal strain at the inner surfaces of both upper and lower spar caps and shear strain in the spar web, respectively. There are six axial and three rosette strain gauges at GS1 and GS3, and two axial and one rosette at GS2. Beside the gauge stations inside the wings, the top and bottom spar caps of the right wing carry-through structure (main spar) as well as the upper surface of the top cap of the left stub spar are also instrumented with strain gauges. Additionally, three locations of interest on the wing skin (two on the right wing and one on the left wing) are identified and equipped with axial strain gauges. The general-purpose axial strain gauges (Vishay Measurements CEA-06-125UR-350) which have a nominal gauge length of 0.125 in. and the rosette strain gauges (Vishay Measurements CEA-10-125UN-350) are tested prior to bonding. The diamond symbol in Figure 4.3 (98.4 in. from the fuselage centerline) represents the location of the resultant force.

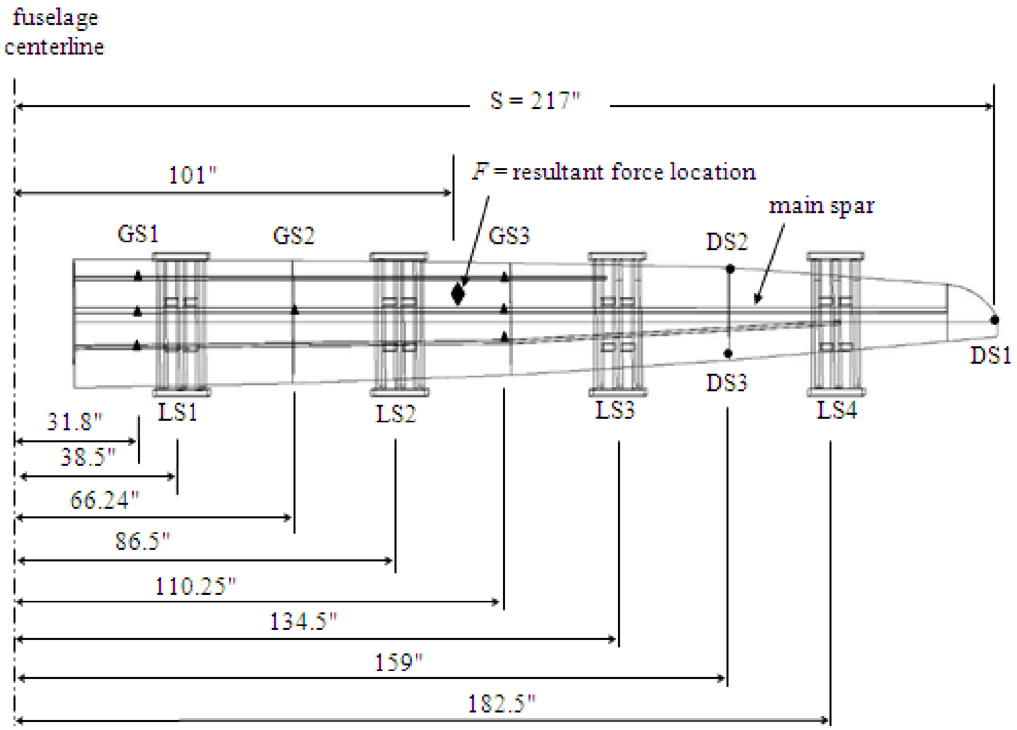
fuselage centerline
S = 217"
101"
F = resultant force location
main spar
GS1
GS2
GS3
DS2
DS1
DS3
LS1
LS2
LS3
LS4
31.8"
38.5"
66.24"
86.5"
110.25"
134.5"
159"
182.5"

Figure 4.3

Strain and deflection gauge locations at various wing stations [19]

Three deflection gauges (Celesco PT1DC cable-extension position transducers), are identified in Figure 4.3 as DS1, DS2, and DS3. These are used to measure the wings' deflection at the wing tip, leading edge, and trailing edge, as illustrated in Figure 4.4. With a maximum stroke length of 50 in., these deflection gauges are used to measure both wing vertical deflection and twist under the load.

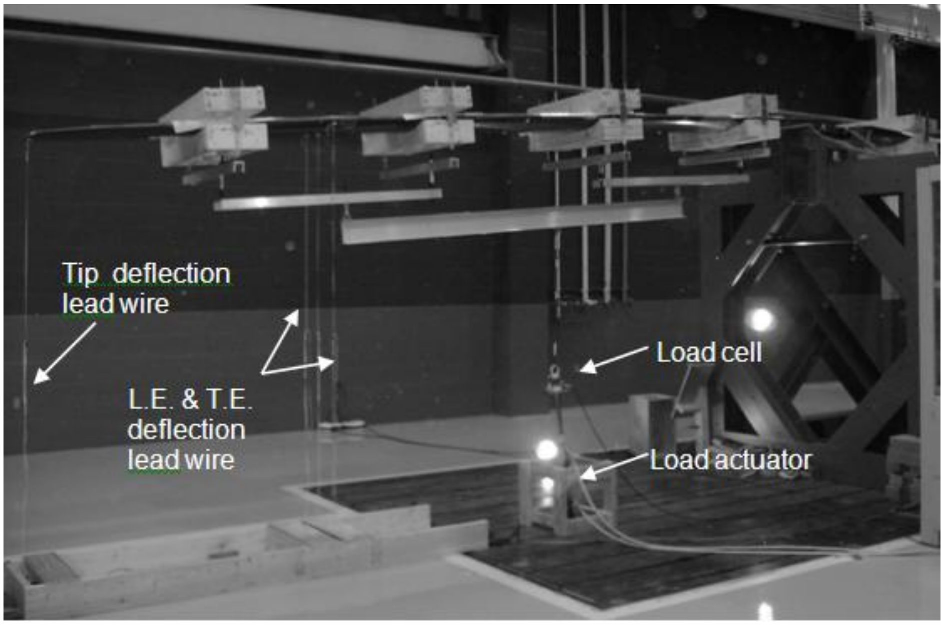

Figure 4.4

Left wing after instrumentation set up

Both load cells and all six deflection gauges are calibrated prior to testing. The initial readings of the strain gauges are taken with the wings resting on the laboratory floor while those of the deflection gauges are obtained with the wing attached to the UTF under its own weight. A total of 80 channels (72 strain channels, six deflection channels, and two load channels) are simultaneously monitored and collected by a computer data acquisition system using LabVIEW® software.

Once the wings are attached to the test fixture, strain deflection readings are taken at each level of assembly of the whiffletree. Once the whiffletree system is completely assembled, the wing structure is loaded in 100 lb increments to the limit load of 855 lb, and it is followed by 50 lb increments to failure. It should be noted that the applied load is the sum of the wing weight, whiffletree weight, and the actuator force.

An 8 ft X 8 ft X 7 ft enclosure was used to house the computer station for the data acquisition system along with the two hydraulic pumps used for the manual application of load to the test assembly. This set up allowed for personnel safety and reduction in equipment damage. A video camera and a 35 mm camera were used to document test progress and events.

4.1.4 Results and Discussion

4.1.4.1 Test Fixture Validation

The strain measurements of the wing assembly obtained from both the static test and the flight test were compared to validate the static testing methodology utilizing the whiffletree system. As mentioned earlier, the high-g pull-up maneuver was considered as the most critical loading condition, and therefore simulated for the static testing of the wing assembly. This configuration essentially induces bending of the wings by placing the top of the wing in tension and the bottom of the wing in compression.

To obtain the true strain responses of the aircraft in such a maneuver, each wing of the flight test aircraft was instrumented with a set of strain gauges at the center of the top and bottom spar caps of the carry-through structure (stub spar, see Figure 3.1). The strain data obtained from two strain gauges at 80 KIAS, 4-g pull-up maneuver, which is considered as the most critical flight maneuver during flight test, is presented in Figure 4.5a. As expected, this figure illustrates the positive (tensile) strain values obtained from the gauge located on the top of the carry-through spar of the left wing, identified as $\varepsilon_{t_{LC}}$, and negative (compressive) strain values obtained from the gauge located on the bottom of the right wing carry-through structure, identified as $\varepsilon_{c_{RC}}$. For comparison, strain gauges are also mounted at the same locations on the carry-through structure of the test wing assembly. The strain data from static testing is presented in Figure 4.5b, where $\varepsilon_{t_{RC}}$ and $\varepsilon_{c_{RC}}$ represent the strains on the top and bottom of the right wing, respectively, and $\varepsilon_{t_{LC}}$ denotes the strains from the top of the left wing carry-through spar. While the maximum strain of approximately 0.002 from both gauges in Figure 4.5a occurs at the highest g-loading, the same strain values in Figure 4.5b experienced by the wings occurs around 700 lb loading, which is well below the limit load value. Therefore, it is observed that the failure load generates far greater strains than those experienced by the aircraft during typical maneuvers. Additionally, from Figure 4.5b, it can be seen that the carry-through structure, although mounted to a rigid fixture such as the UTF, does experience the load transfer, thereby reasonably simulating the transfer of the wing load to the fuselage.

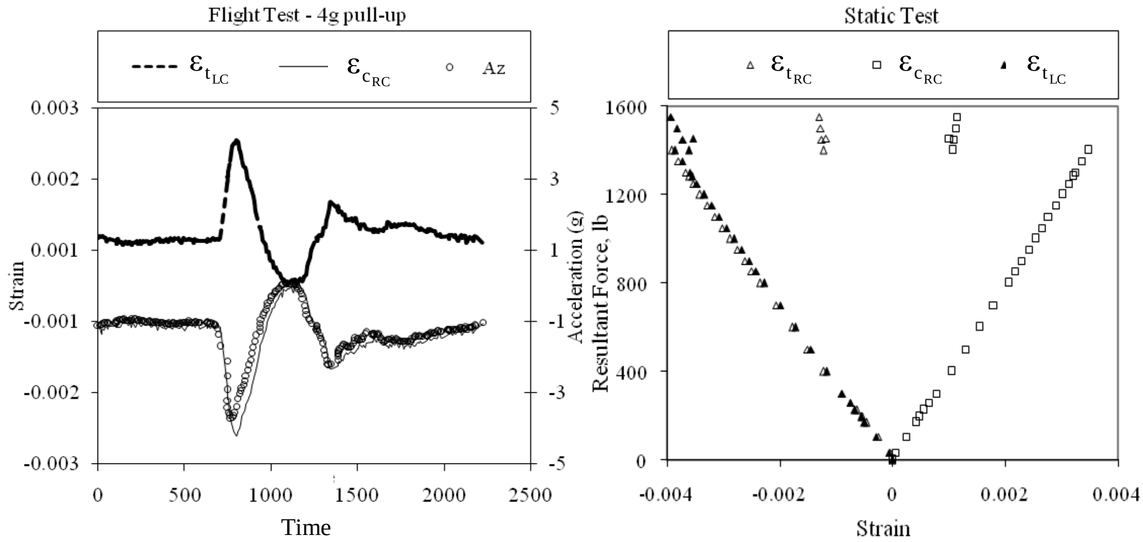

(a) (b)

Figure 4.5

Strain response from carry-through structure (a) flight test at 80 KIAS, 4-g pull-up maneuver (b) static test

4.1.4.2 Preliminary Testing

Prior to testing the wing structure to failure, preliminary testing was performed to obtain the structure's bending stiffness. Both wings were subjected to a concentrated load at a single station, the span-wise location corresponding to DS2 and DS3 locations (shown in Figure 4.3). The load was applied in 10 lb increments up to a total of 60 lb. The deflections for the left wing and the right wing were measured and tabulated in Table 4.2 and 4.3, respectively. Flexural rigidity, EI, was calculated by using an elementary mechanics of materials solution for a cantilever beam with a tip load. The average bending stiffness was found to be 3.36 x10^7 lb-in^2 and 2.91 x10^7 lb-in^2 for left and right wing, respectively, as listed in Tables 4.2 and 4.3.

Table 4.2

Left wing deflection from bending stiffness test

Applied load (lb)	**Leading edge deflection (in)**	**Trailing edge deflection (in)**	**Wing tip deflection (in)**	**Average deflection (in)**	**Flexural rigidity (lb-in^2)**
10	0.429	0.419	0.682	0.424	3.31E+07
20	0.713	0.709	1.170	0.711	3.39E+07
30	1.022	1.003	1.667	1.013	3.37E+07
40	1.312	1.297	2.150	1.305	3.38E+07
50	1.621	1.597	2.638	1.609	3.37E+07
60	1.905	1.886	3.096	1.896	3.39E+07
				Avg	3.36E+07

Table 4.3

Right wing deflection from bending stiffness test

Applied load (lb)	**Leading edge deflection (in)**	**Trailing edge deflection (in)**	**Wing tip deflection (in)**	**Average deflection (in)**	**Flexural Rigidity (lb-in^2)**
10	0.409	0.455	1.988	0.432	2.32E+07
20	0.684	0.726	1.081	0.705	2.85E+07
30	0.993	1.011	1.569	1.002	3.00E+07
40	1.297	1.321	2.068	1.309	3.06E+07
50	1.617	1.627	2.571	1.622	3.09E+07
60	1.921	1.927	3.064	1.924	3.13E+07
				Avg	2.91E+07

Additionally, the wing assembly was tested to its limit load of 855 lb prior to testing to failure. It was noted that the compression loaded skin of both the left and right wings wrinkled (buckled) around 800 lb and visual inspection revealed no evidence of any significant damage in the skin or the carry-through structure. However, after complete removal of the load, the permanent deformation in the skin area between the root section and LS1 was visually observed. Two uniaxial strain gauges were then mounted in the damage zone of the right wing and one on the left wing skin.

4.1.4.3 Test to Failure

Figure 4.6 shows plots of the applied load versus deflection for both wings. All deflection plots show a linear trend. For the ultimate load, the figure indicates the right wing and the left wing achieving a maximum tip deflection (DS1) of approximately 32 in. and 37 in., respectively. Since the deflection obtained from DS2 and DS3 of both wings is nearly identical, only those of the left wing will be shown here. The comparable deflection of the leading and the trailing edge in Figure 4.6b indicates an absence of wing twist even at the higher loads. Additionally, the discontinuity of the data shown at approximately 1450 lb represents the failure point of the right wing. The loading is increased on the left wing until failure is reached.

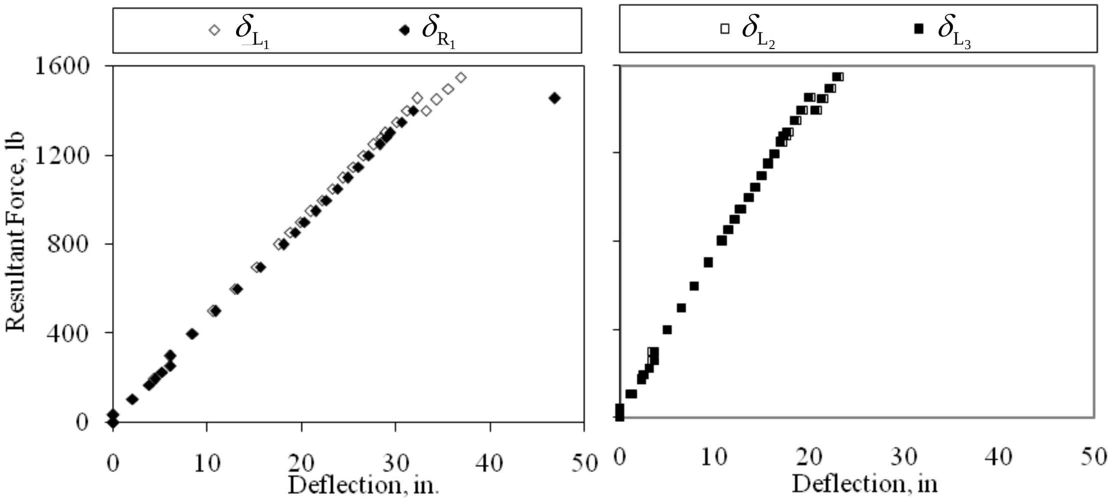

(a) (b)

Figure 4.6

Wing deflection at (a) DS1 of the right and left wing (b) DS2 and DS3 of the left wing

Data from all 80 channels was recorded simultaneously. Due to limitations in the data acquisition capabilities, some data, such as the response from the rosette gauge at GS3 was not recorded. Three normal strain measurements (at 0º, 90º, and 45º) at each web rosette are used to compute the shear strain values, whereas the axial strains are directly obtained from the reading of the cap strain gauges. For ease of comparison, the measured strains from the right and the left wings at the same spar locations are plotted together and presented in Figures 4.7-4.10. In these figures, $\varepsilon_{c_{LC}}$ corresponds to the axial strain at the compression cap of the left wing while $\varepsilon_{c_{RC}}$ corresponds to that of the right wing. Consistent labels are used for the spar caps in tension and spar webs in shear.

The similarity of the strain readings from the left and right wings in these figures demonstrates the consistency in loading the left and right wings, the strain gauge placement, and the resemblance in structural properties of the two wings. On the other hand, the dissimilarity between the compressive and tensile cap strains is primarily due to lack of cross-sectional symmetry, dominated by the airfoil geometry at the fore and aft spar locations and cap laminate thickness at the main spar location. As evident by the results, the strain reading at the midpoint between the inner surface of the upper cap and the lower cap does not necessarily correspond to strain at the location of the neutral axis.

Figure 4.7 illustrates all three strain measurements at GS1 for the three spars. All strains appear to vary linearly for the most part with a slight nonlinearity in the tensile and shear strains beyond the 1200 lb marker. The nonlinearity is due to the discontinuity of measurement signal after the failure of the wing. Compared to the fore and aft spar, the main spar web experiences the most shear deformation at GS1. The magnitude of axial strains at both the compression and the tension cap of all spars are comparable for both wings except those of fore spars, where the axial strains of the right wing are increasingly greater than those of the left wing. The difference in shear strains between the right and the left wing is also noticeable for all three spars.

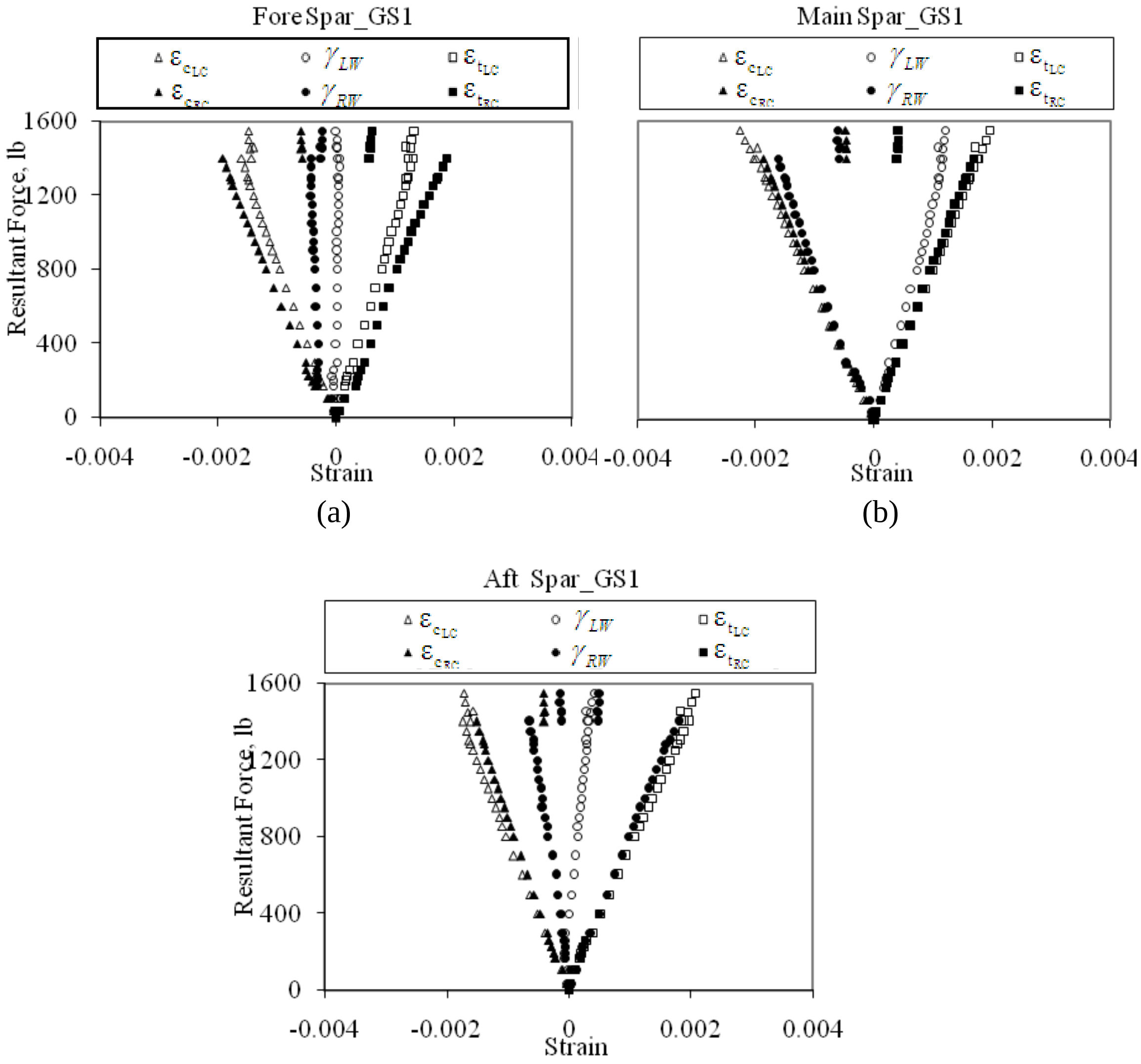

(a) (b)

(c)

Figure 4.7

Axial and shear strains at GS1 of the right and left wing (a) fore, (b) main, (c) aft spars

The strain response at GS2 is shown in Figure 4.8. From the plots, the greatest axial and shear strains occur at this station when compared to other stations. Although the bending moment is larger at GS1, the strain is larger at GS2 due to the change in the wing’s cross sectional dimension. The decrease in the area reduces the moment of inertia such that the ratio of bending moment to moment of inertia is higher at GS2 than at GS1.

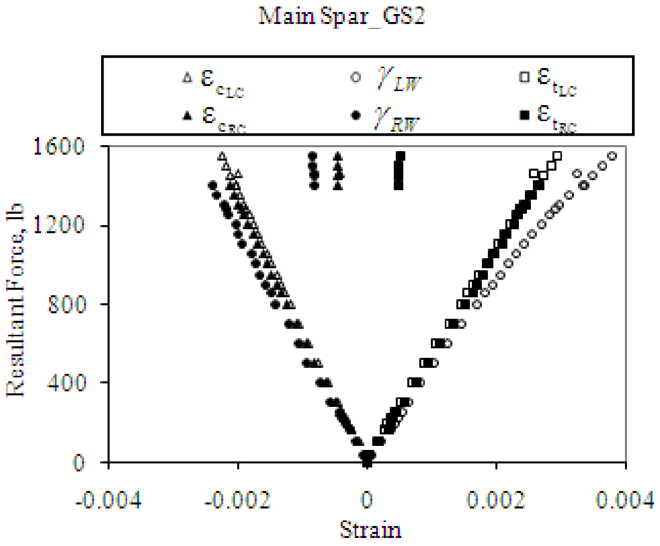

Figure 4.8

Axial and shear strains at GS2 of the right and left wing main spars

Figure 4.9 shows the comparison for the strains from the main spar at GS1 and GS2 for the left wing. Though the compressive strains of both stations are similar, it is seen that the shear and tensile strains at GS2 are significantly larger than those at GS1. Again, this is due to the smaller bending moment at GS2, when compared to that at GS1, that creates the smaller section modulus but higher in strain at GS2. Linear variation is observed for all channels with a slightly nonlinearity beyond the 800 lb load.

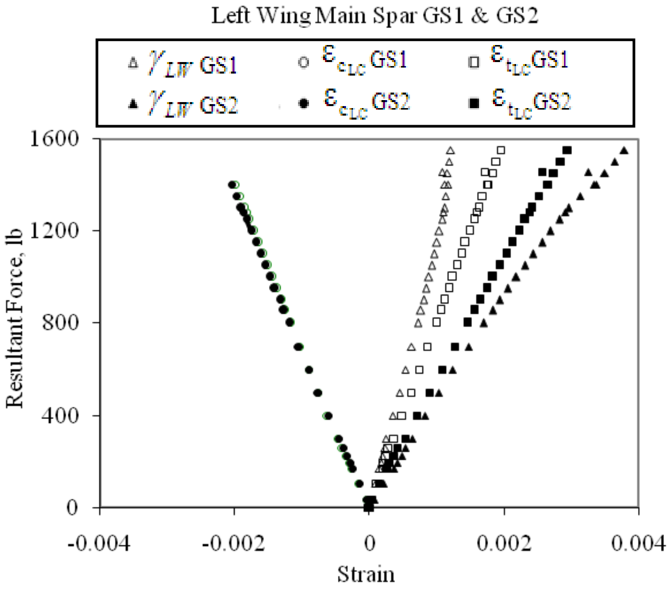

Figure 4.9

Comparison of strains at GS1 and GS2 of left wing main spar

Figure 4.10 shows the strain response at GS3. The axial strains at both compression and tensile cap of the aft spar are practically identical. The same observation also applies for all compression strains for fore and main spar as well as their tensile strains below 400 lb.

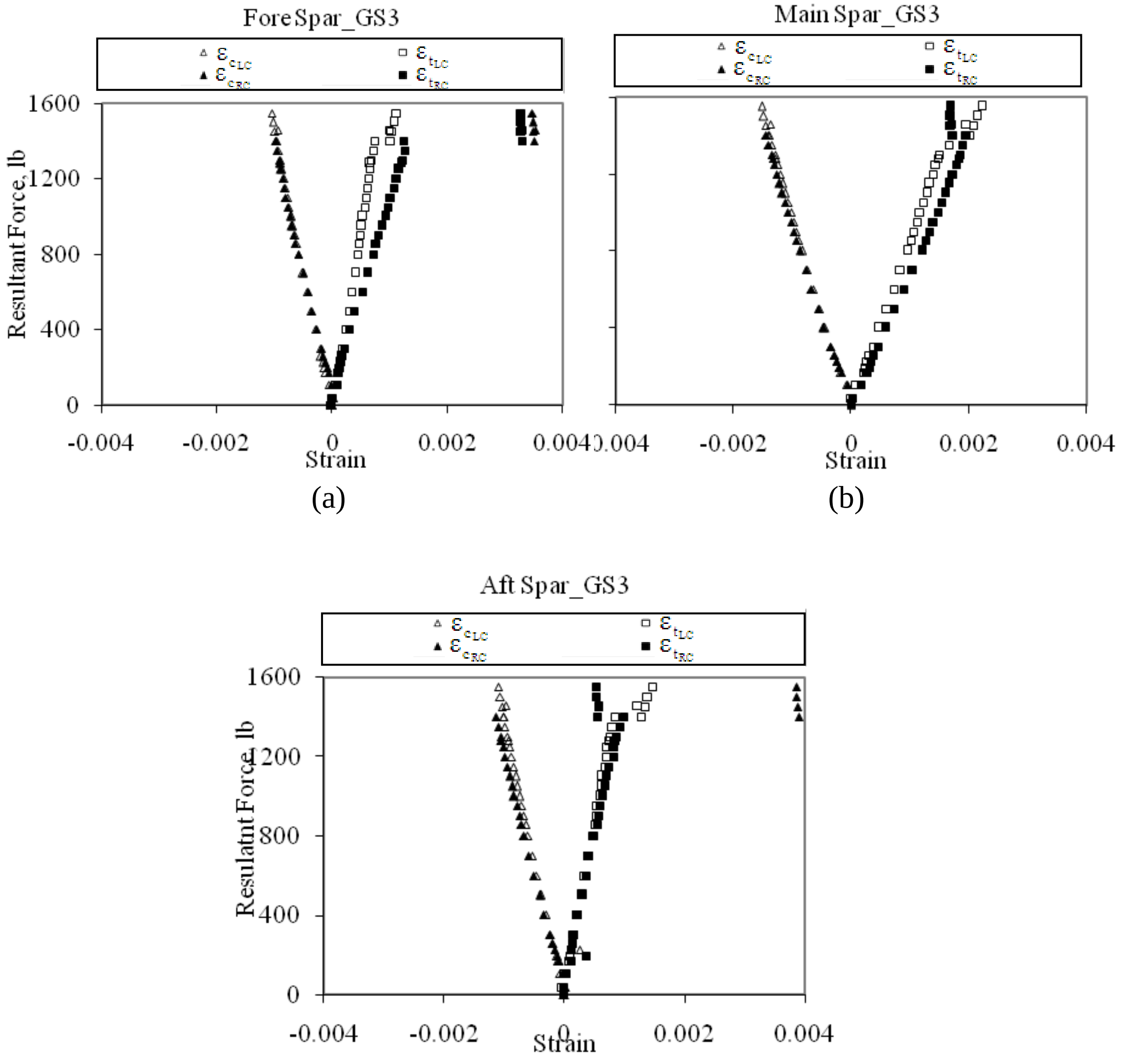

(a) (b)

(c)

Figure 4.10

Axial and shear strains at GS3 of the right and left wing (a) fore, (b) main, (c) aft spars

The percent difference between the right and left wing strain readings at 1400 lb are listed in Table 4.4. As previously mentioned, due to the limited number of channels that could be recorded at the same time, only the main spar at GS2 is monitored and several shear strains are not obtained. The largest variations occur in the fore spar of both GS1 and GS3 in the tension caps with the difference of 30.3% and 40.2%, respectively. As shown in Figure 4.7, the normal strains at GS1 in the main and aft spar caps are almost identical for both wings until 800 lb. As the load increases after 800 lb, the difference in the strain values for both wings also begins to increase. However, for the fore spar (Figure 4.7a), the difference in strain readings for the left and right wings are clearly observed from the beginning. Overall, the similar responses from both wings indicate similar material and structural equivalence as well as symmetric bending of the left and right wing structures.

Table 4.4

Percent difference between left and right wing strain readings at 1400 lb

Stations	**Spar**	**Compression Cap**	**Tension Cap**
GS1	Fore	16.6	30.3
	Main	5.8	3.70
	Aft	15.4	9.30
GS2	Main	3.9	0.03
GS3	Fore	2.6	40.2
	Main	3.9	11.8
	Aft	10.4	15.2

The percent tip deflection (δ) was measured from the initial position of the wing tip over the wing length of 217 in. along with the ratio of applied load to the wing for four loadings: the limit load, design ultimate load, and the load prior to the failure of both wings. The results, listed in Table 4.5, show that the deflection of both wings under various loadings are consistent and hold up to approximately 14% prior to failure for the right wing and 17% prior to failure for the left wing. This data also reveals that both wings are able to withstand more than 40% of their own weight.

Table 4.5

Deflection and strength characteristics of the wing structures

Load Type	**Applied Load (lb)**	**%** $\frac{\delta_R}{L}$	**%** $\frac{\delta_L}{L}$	$\frac{\text{Applied Load}}{\text{W}_{\text{wing}}}$
Limit	855 (3.7 g)	8.67	8.87	24.4
Design Ultimate	1283 (5.7 g)	13.08	13.36	36.7
Right Wing Failure	1456 (6.4 g)	14.37	14.67	41.4
Left Wing Failure	1550 (6.9 g)	-	17.02	44.3

The right wing under the limit load, design limit load, and at its failure is shown in Figure 4.11, whereas the failure of both wings is shown in Figure 4.12. The right wing failed at 1456 lb, with a maximum tip deflection of 31.8 in, whereas the left wing failed at 1550 lb and a maximum tip deflection of 36.9 in, both exceeding the design ultimate load of 1283 lb. The wing structure symmetrically failed on the compression side at the transition of the aileron cutout as shown in Figure 4.12b. The failure location also corresponds to the region of the wing with the highest predicted local strains, based upon material and geometric nonlinear finite element analysis [4].

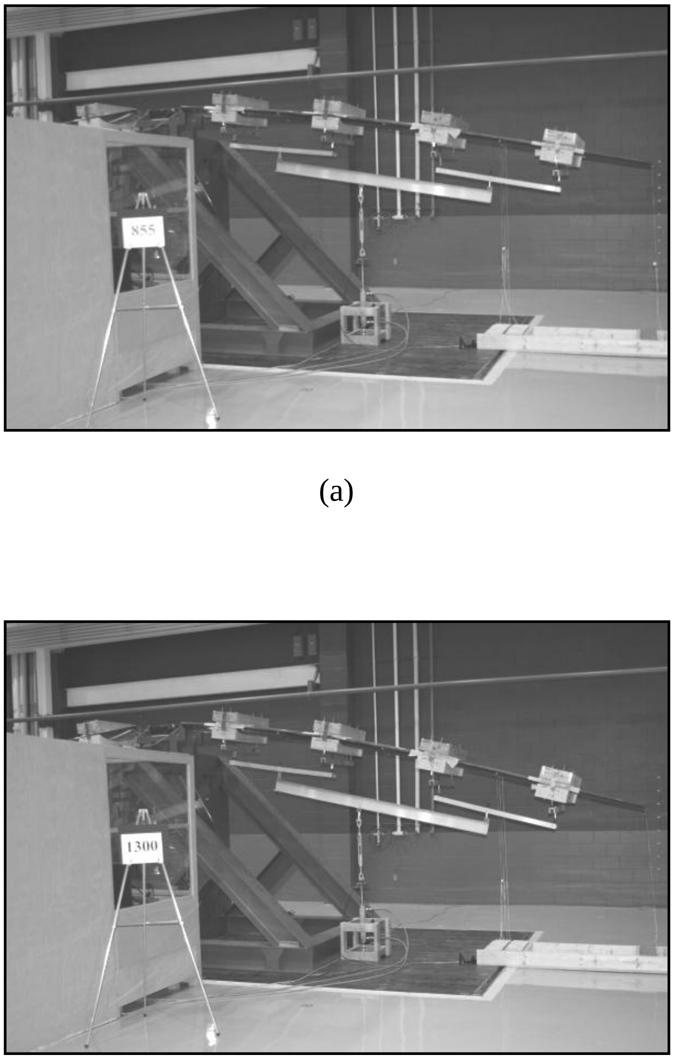

(a)

(b)

Figure 4.11

Right wing at (a) the limit load, (b) the design limit load, and (c) failure

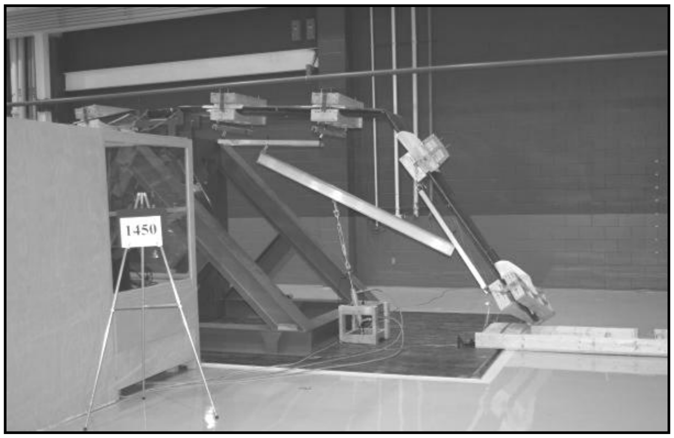

(c)

Figure 4.11 (continued)

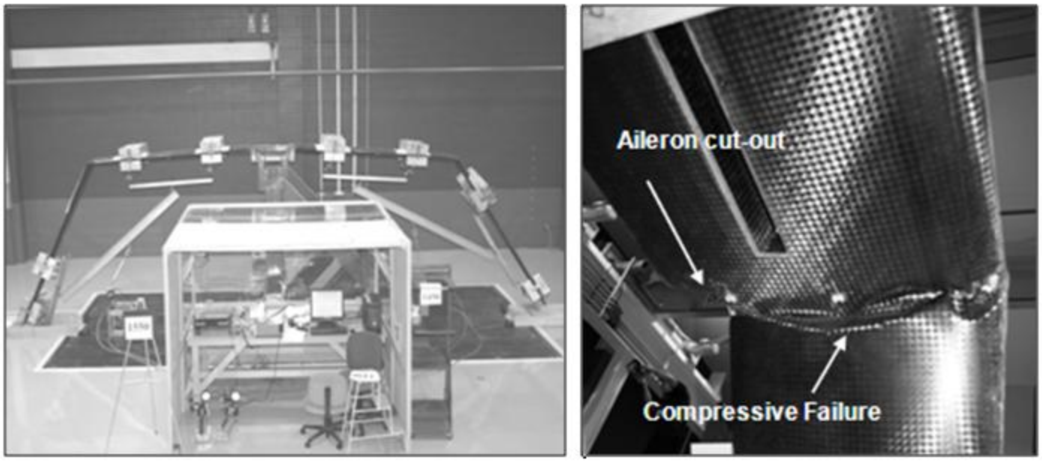
Aileron cut-out
Compressive Failure

(a) (b)

Figure 4.12

Wing structure at failure (a) general mode (b) specific location

4.2 Fuselage/tail Testing

In service, an aircraft fuselage is subjected to various operational loads including aerodynamic loading and internal pressure loading which induces fuselage bending and twisting producing both circumferential and longitudinal stresses to the fuselage body. In this study, the experimental testing and analysis is limited to aerodynamic loading only.

4.2.1 Loading Methodology

Similar to the static testing of the wings, typical critical loading conditions of the fuselage/tail structure were considered. For steady-level flight, an aircraft generates lift equal to its weight and the fuselage is in equilibrium condition. Assuming the wings remain level, when an aircraft encounters positive vertical wind gusts (updrafts), the fuselage is subjected to an abrupt change of aerodynamic load, placing the top of the fuselage in tension. Conversely, negative wind gusts (downdrafts) places the top of the fuselage in compression. Additionally, certain aircraft maneuvers such as banking and rolling produce twist in the fuselage structure. An approach to simulate these three typical loadings (updraft, downdraft, twist) is presented.

The bending and twisting of the fuselage/tail was simulated by applying both symmetric and asymmetric loads by applying various combinations of the concentrated loads F_1 and F_2, as shown in Figure 4.13.

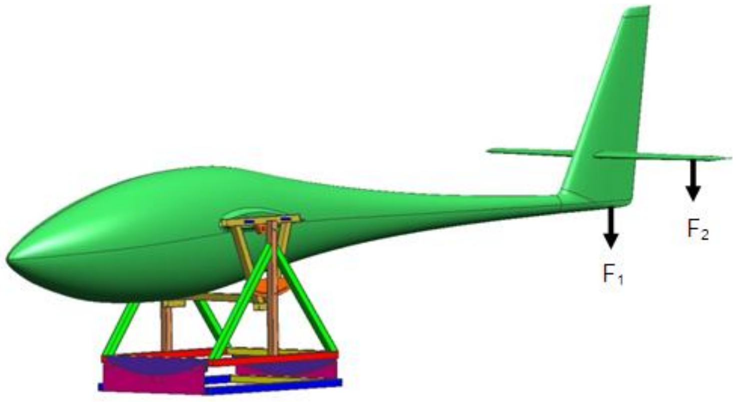

Figure 4.13

Fuselage loading configuration

4.2.2 Experimental Set Up

As mentioned in Chapter 1, the aircraft has an engine that can be retracted inside the fuselage when it operates in glider mode. However, the static and vibration test are performed on the empty fuselage body with both the engine and the pilot seat removed. As shown in Figure 4.13, the fuselage/tail structure is mounted in the test fixture via the wing/ fuselage connection points. Figure 4.14 shows the loading fixture, which is specially designed to facilitate the various loading configurations of the fuselage/ tail structure. This loading fixture is attached to the fuselage through the vertical stabilizer at its horizontal stabilizer attachment points. This enables the loading to be applied in either a downward (placing the top of the fuselage in tension) or upward (placing the top of the fuselage in compression) direction. Additionally, in order to simulate a combined bending/ torsion loading, the fixture is designed such that a cross-member (eccentric load member) can be attached to the bottom horizontal member for application of an eccentric load as shown in Figure 4.15.

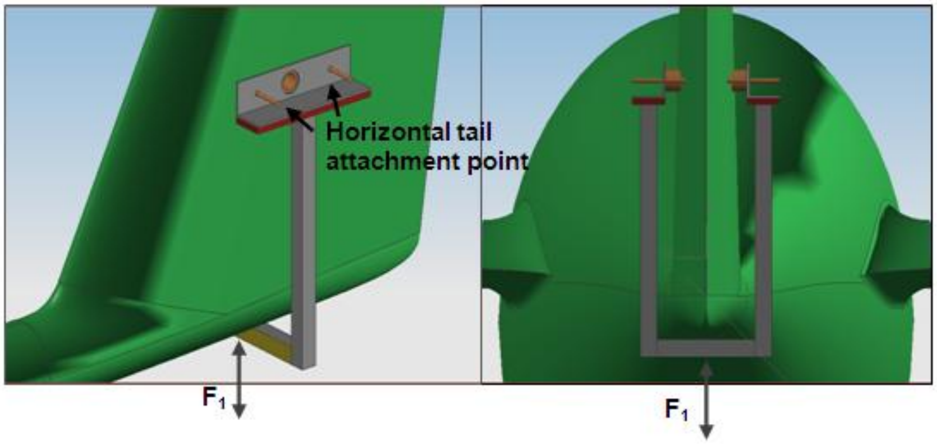
Horizontal tail
attachment point
F_1
F_1

Figure 4.14

Test fixture for F_1 loading

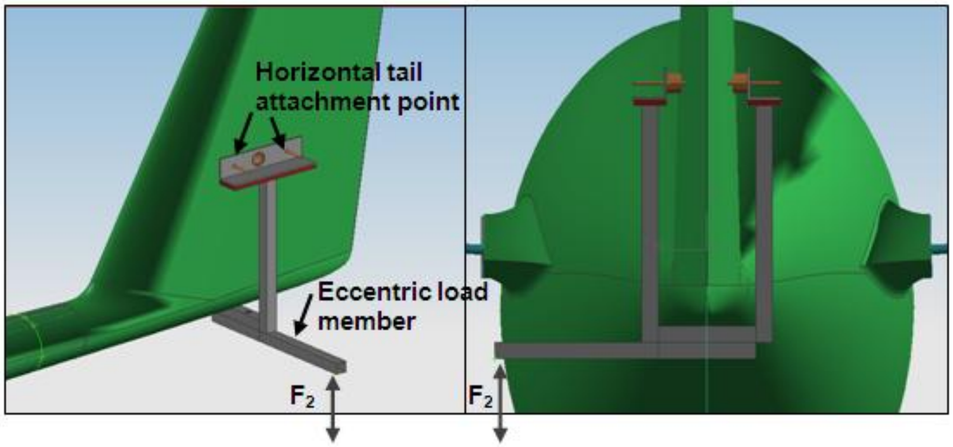
Horizontal tail
attachment point
Eccentric load
member
F_2
F_2

Figure 4.15

Test fixture for F_2 loading

4.2.2.1 Preliminary Testing

Unlike the static testing of the wings, where majority of the strain measurements were taken from the wing spars, the responses from the static testing of the fuselage/tail structure were primarily from the skin surface. Therefore, prior to initiating the actual fuselage/tail static testing, preliminary testing was implemented to understand the effect of strain gauge placement relative to fiber tows (A vs. B) on measured strain values as shown in Figure 4.16.

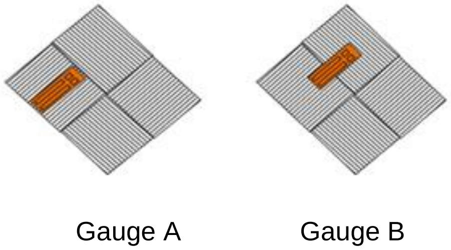

Figure 4.16

Strain gauge location relative to the fiber tows

To set up the test, four uniaxial strain gauges were mounted in various configurations at four fuselage stations. Figure 4.17a shows the cross-sectional view of gauge placements for each station where the circle strain gauges (I1, I3, and J2) depict gauges that are attached at the intersection of the fiber tows (gauge B in Figure 4.16) whereas the diamond strain gauges (J1, J3, and I2) are attached at the center of the fiber tows (gauge A in Figure 4.16). Figure 4.17b shows the gauge placement on the fuselage station, which is 81.5 in. from the wing attachment point.

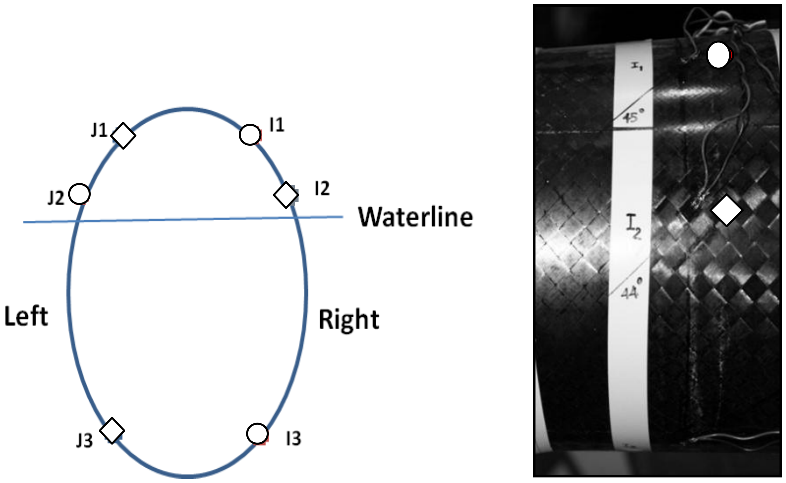

(a) (b)

Figure 4.17

Strain gauge placement of preliminary testing (a) cross-sectional view of gauges (b) fuselage station

A container is suspended centrally from the horizontal member of the loading fixture (Figure 4.14). Pre-weighed lead bags are placed into the container to simulate a downward loading. Using two portable Vishay P3 strain indicator and recorder units (total of 8 strain channels), strain measurements were first taken with the fuselage/tail body under its own weight then with the loading fixture, followed by 10-lb increments up to a total of 70 lb. The data from these strain gauges was compared at various cross-sectional locations at each fuselage station then analyzed to establish strain gauge placement for the remainder of the fuselage testing. By keeping all other parameter fixed, the results from the preliminary testing revealed minimal differences in strain measurements obtained between gauge placement at different locations relative to fiber tows as shown in Figure 4.18.

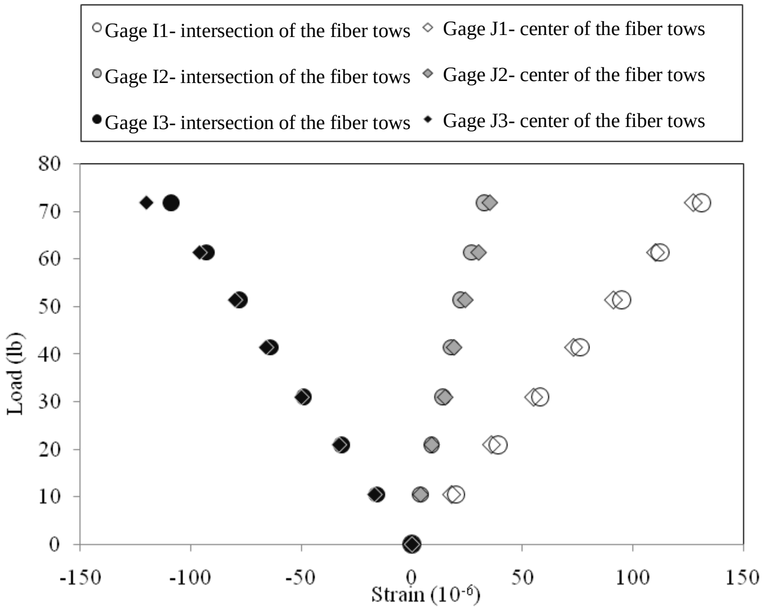

Figure 4.18

Preliminary static testing results from strain gauges located at gauge station shown in Figure 4.17

4.2.3 Instrumentation

Based on the preliminary test results, four strain gauges (two rosette gauges and two uniaxial gauges) are mounted at each gauge station, with the exception of GS1, of the fuselage body in the configuration shown in Figure 4.19. Only two strain gauges, which are identified as L-D and R-D, are mounted at GS1 due to the cockpit cutout section. The location of the strain gauges at each station is determined by utilizing the X-pattern. The X-pattern is designed such that strain gauges are placed at the intersection of the radial line on the fuselage stations. The points where the lines and the outer edge of the fuselage cross section intersect represent strain gauges location. The X-pattern data was obtained from five fuselage strain gauge stations, GS1 through GS5, shown in Figure 4.20. These were carefully selected such that no strain gauge stations were located in abrupt material or geometry transition regions of the structure.

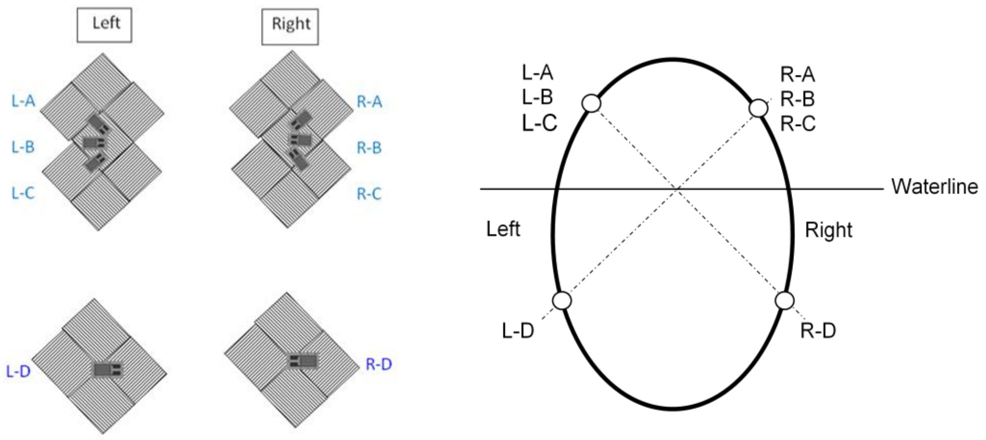
Left
Right
L-A
L-B
L-C
R-A
R-B
R-C
L-D
R-D
L-A
L-B
L-C
R-A
R-B
R-C
Waterline
Left
Right
L-D
R-D

(a) (b)

Figure 4.19

Strain gauge configuration (a) gauge placement showing the rosette gauges and the uniaxial gauges (b) cross-sectional view of strain gauge locations at fuselage station

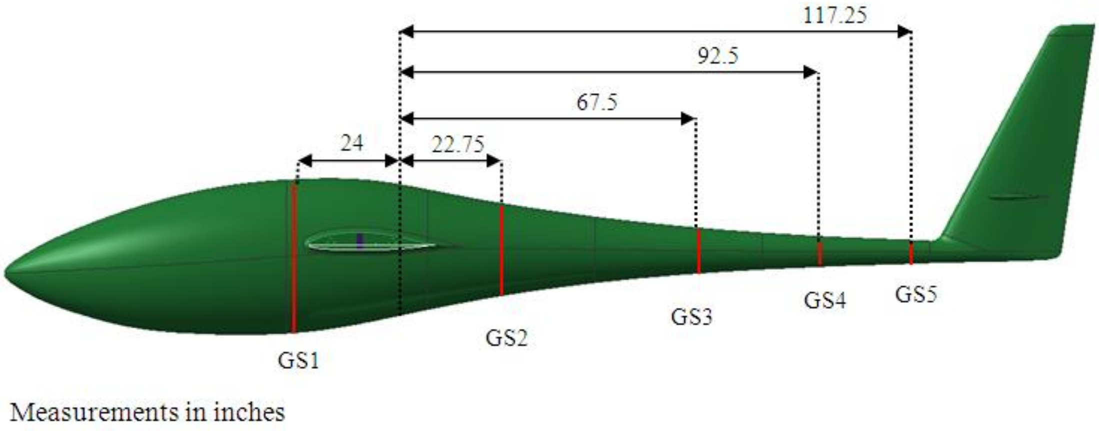
117.25
92.5
67.5
24
22.75
GS1
GS2
GS3
GS4
GS5
Measurements in inches

Figure 4.20

Fuselage strain gauge stations

Actual loading of the structure was similar to that used for the wing assembly tests where the load was manually applied by a load actuator (hydraulic cylinder). To simulate the downward loading, the load actuator was mounted to the surface plate mounted on the laboratory floor and attached to the loading fixture to induce a centric downward loading (F_1) or to the free end of the aluminum bar (eccentric load member) to induce an eccentric loading (F_2) as shown in Figure 4.20. To simulate an upward eccentric loading, the load actuator is suspended from a hoist and attached to the base of the tail loading fixture as shown in Figure 4.21. To obtain the input force to the structure, a load cell is connected in series with the load actuator. The measurement technique is similar to that used in the preliminary test where the strain measurements are first taken with the fuselage/tail body under its own weight then with the loading fixture, followed by 10 lb. increments up to a total of 100 lb. The static responses from the 34 strain channels were taken simultaneously using a LabVIEW® program.

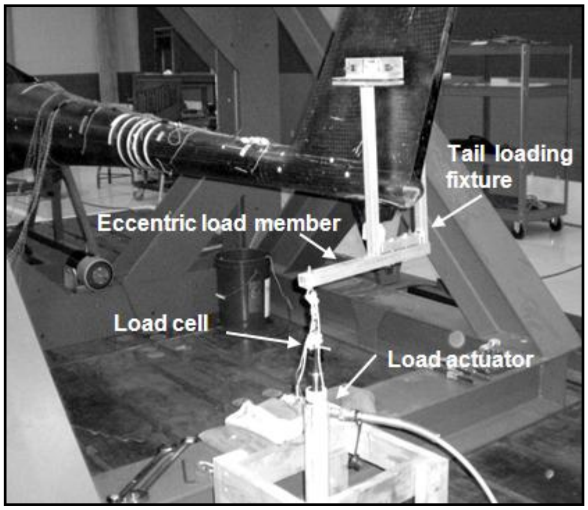

Figure 4.21

F_2 push-down loading methodology

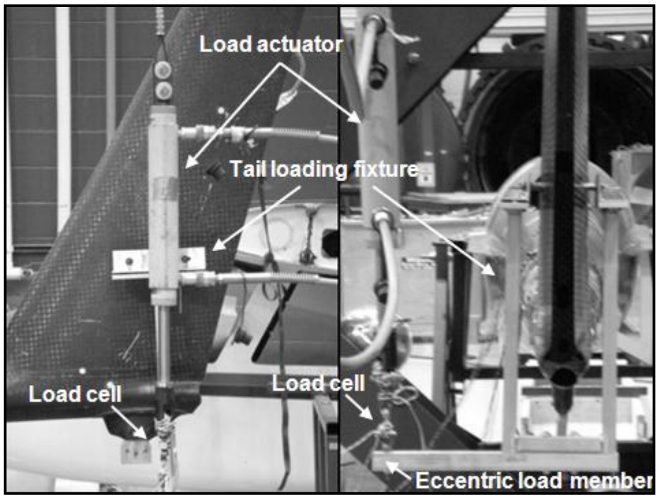

Figure 4.22

F_2 pull-up loading methodology

4.2.4 Results and Discussion

The fuselage/tail structure is subjected to both symmetrical and asymmetrical loading conditions. Loading configurations included centric pull-down, eccentric pull-down, and eccentric push-up. These conditions were achieved by applying the load in the desired direction through the tail loading fixture that was connected to the vertical tail at the horizontal tail attachment points. The following sections present the results associated with the three loading configurations.

4.2.4.1 Centric Loading

Figure 4.23 shows the fuselage body with the selected coordinates parallel (x-axis) and perpendicular (y-axis) to the waterline. Utilizing the strain transformation equations [21], the strain readings from the rosette strain gauges at each gauge station were resolved into longitudinal (ε_x), transverse (ε_y), and a shear strain (γ_{xy}) with respect to the waterline.

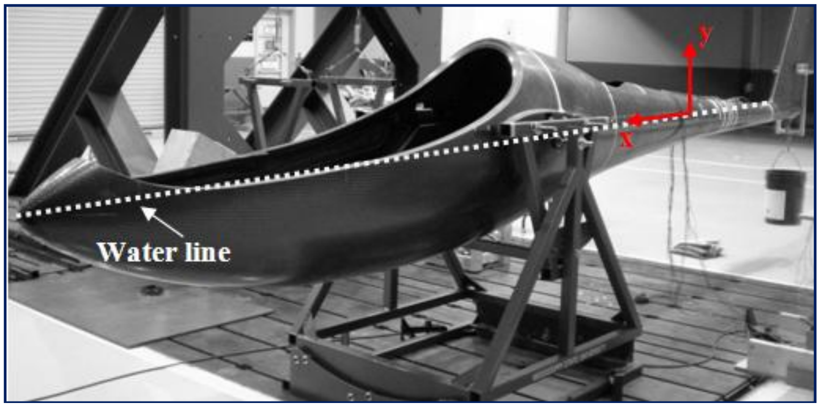

Figure 4.23

Strain measurement direction of test structure

Figure 4.24 and 4.25 show the responses from the rosette strain gauges at the five gauge stations (see Figure 4.20) for centric pull-down loading. The plots in Figure 4.24a through 4.24d correspond to the strain readings at gauge stations 2 to 5, respectively. To study the progress of the responses throughout four gauge stations, the strains were grouped and plotted by the strain type (longitudinal, transverse, and shear) as shown in Figure 4.25. In these figures, the longitudinal strains from the rosette gauges located on the right side of the fuselage are identified as ε_{X_R} , whereas those obtained from rosette gauges located on the left of the fuselage are identified as ε_{X_L} . Consistent labels are used for the transverse and shear strains. The maximum strain value of each strain type for both sides of the fuselage and the gauge station at which the maximum strain occurred are present in Table 4.6.

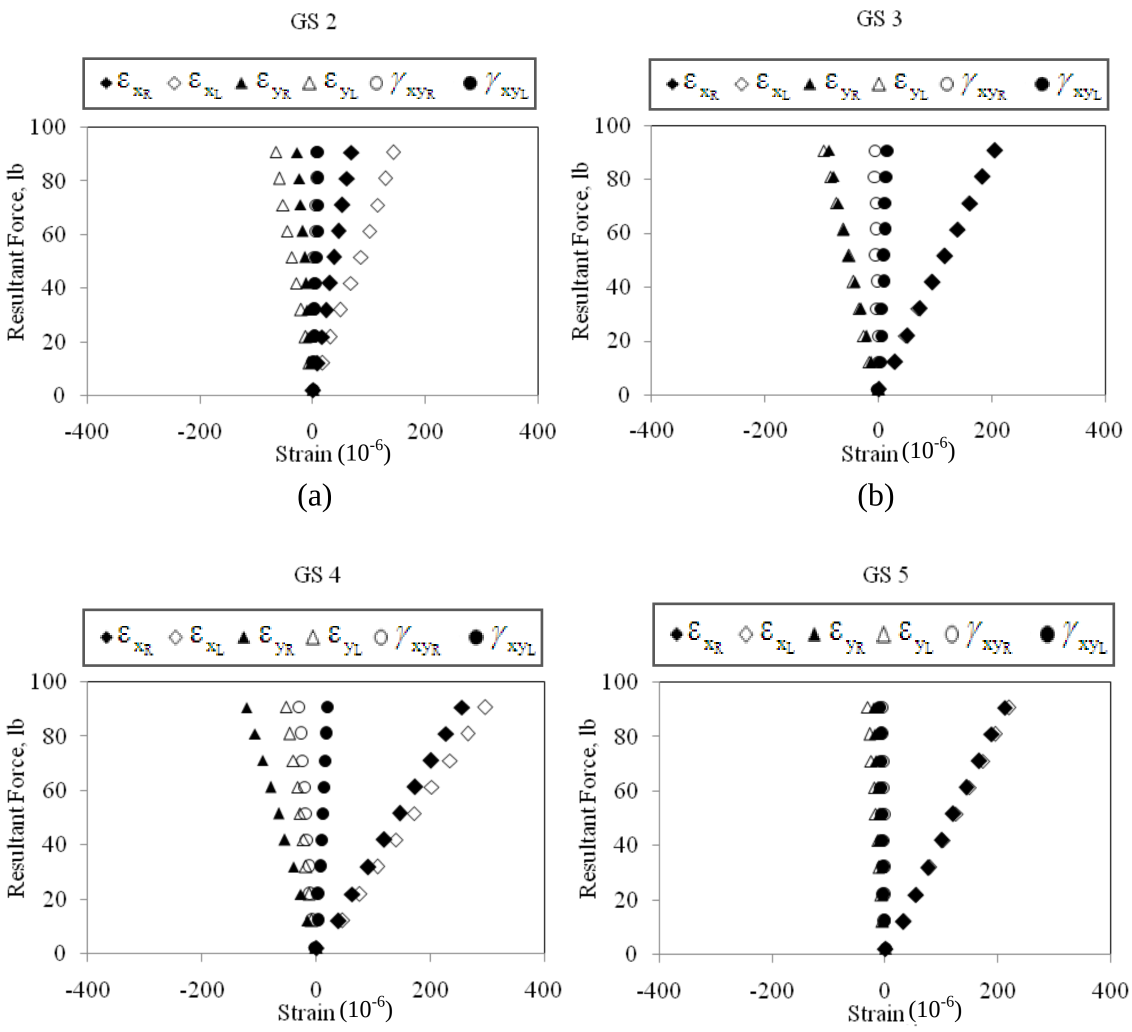

(a) (b)

(c) (d)

Figure 4.24

Strain measurements from centric pull-down loading at (a) GS2, (b) GS3, (c) GS4, and (d) GS5

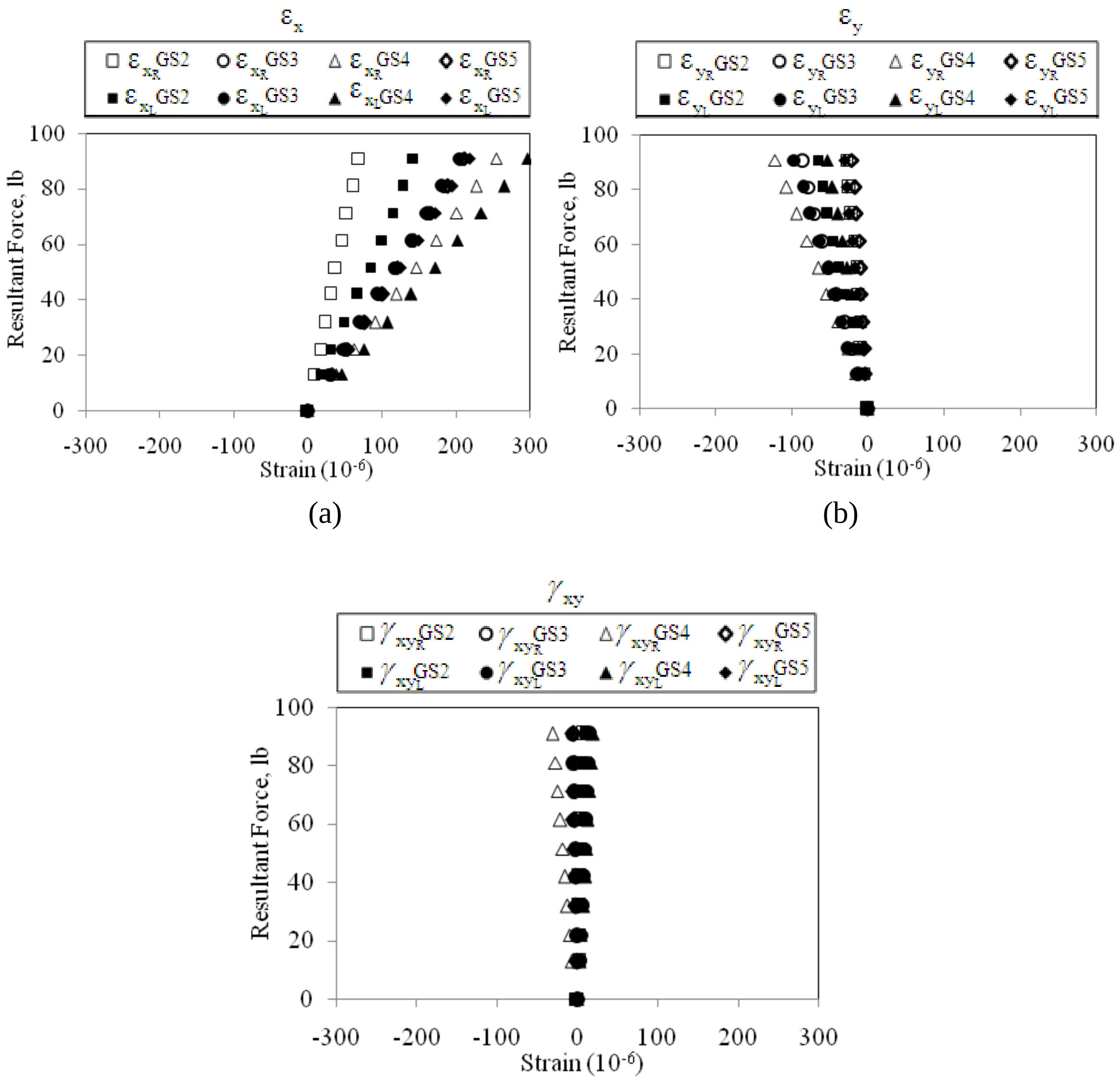

(a) (b)

(c)

Figure 4.25

Measurements of (a) ε_x ,(b) ε_y , and (c) γ_{xy} from centric pull-down loading

Table 4.6

Maximum strain readings at 100 lb centric pull-down loading

Strain		Strain value (10^{-6})	Station
Right	ε_x	280.1	GS4
	ε_y	-133.8	GS4
	γ_{xy}	-33.5	GS4
Left	ε_x	325.5	GS4
	ε_y	-106.1	GS3
	γ_{xy}	21.2	GS4

All gauge station responses, with the exception of GS2, show linear trends and similar longitudinal strains on both the left and right sides of the fuselage. The maximum longitudinal strain of approximately 326×10^{-6} strain was found to occur at the left side of GS4, which from Figure 4.24, is seen to occur quite close to the load application point. To understand this response, a simple strain analysis was performed on a tapered cantilevered beam having a solid circular cross section subjected to a vertical load at its free end. The normal strain (in x direction) was calculated and plotted for the entire length of the member ($0 \leq x \leq L$). Figure 4.26 shows the strain increasing from the free end of the member, achieving a maximum at 22%L, and then gradually decreasing to the fixed support. The result is due to the decreasing moment of inertia toward the load application point, which produces large strain values for a given moment. Therefore, it was concluded that the longitudinal strains of the fuselage body at GS4 are reasonable. The greatest discrepancy of the longitudinal strain between the left and the right side of the fuselage occurs at GS2 (Figures 4.24a and 4.25a). This difference is attributed to the slightly off alignment of the strain gage placement in either side of the fuselage at GS2.

It is observed that the transverse strain on the right side progresses toward the negative range as the transverse strain response of the left side moves more toward the positive range. The shear strains from both sides are found to be in good agreement, especially at GS3 and GS5.   There seems to be minimal shear strain on the left side of the fuselage, whereas the right side shear strain behaves much like the right side transverse strain, and attains its largest value at GS4.

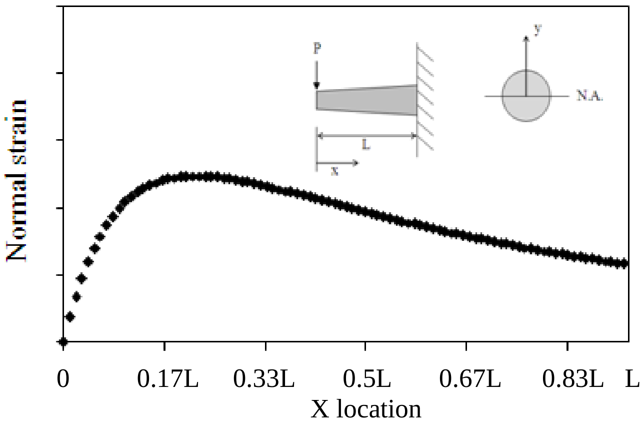

Figure 4.26

Normal strain (in x-direction) along the length

4.2.4.1 Eccentric Loading

The strain response from the five gauge stations for the eccentric pull-down loading is shown in Figure 4.27 and 4.28. Table 4.7 lists the maximum strain values at approximately 100 lb eccentric pull-down loading.

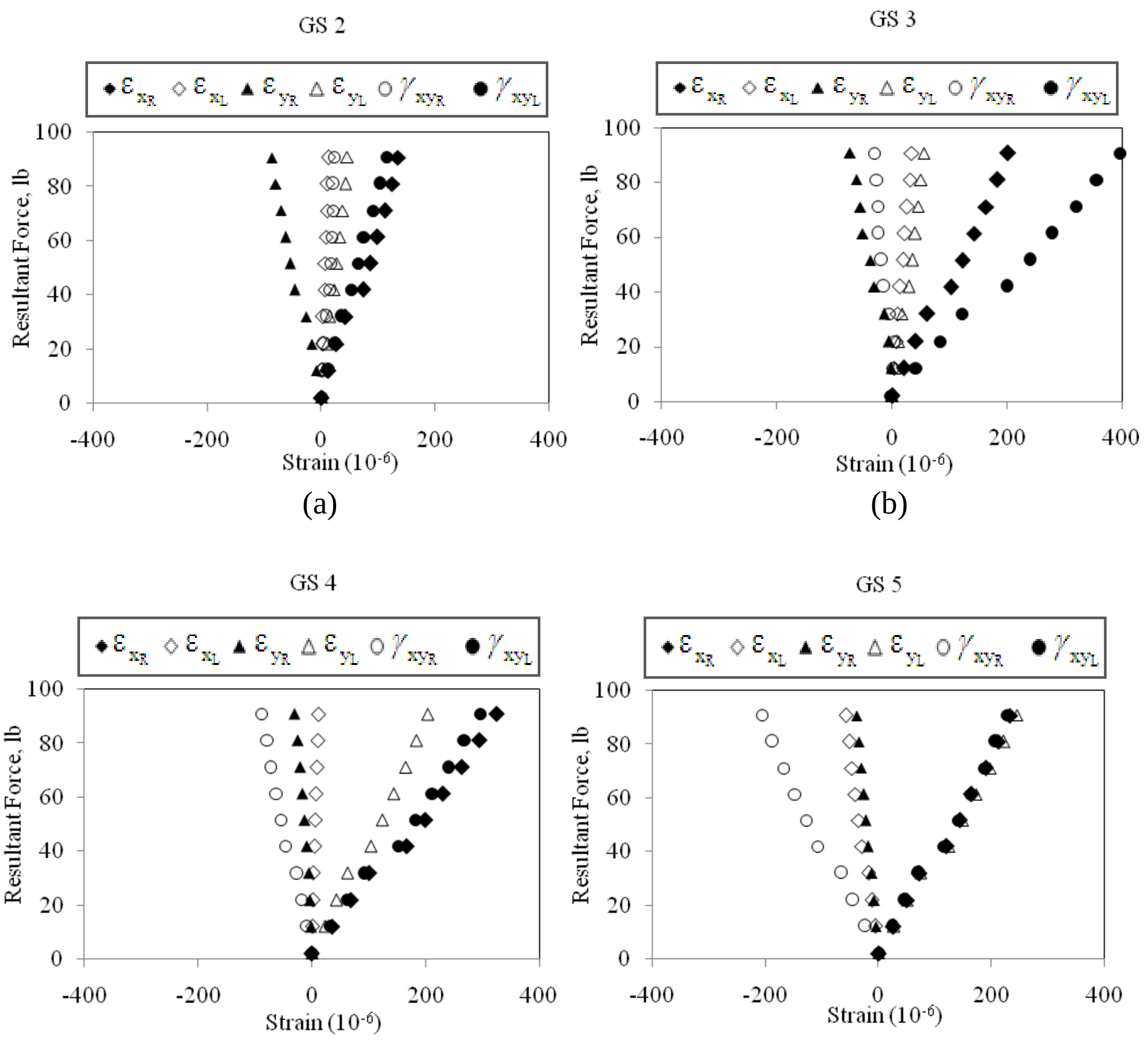

(a) (b)

(c) (d)

Figure 4.27

Strain measurements from eccentric pull-down loading at (a) GS2, (b) GS3, (c) GS4, and (d) GS5

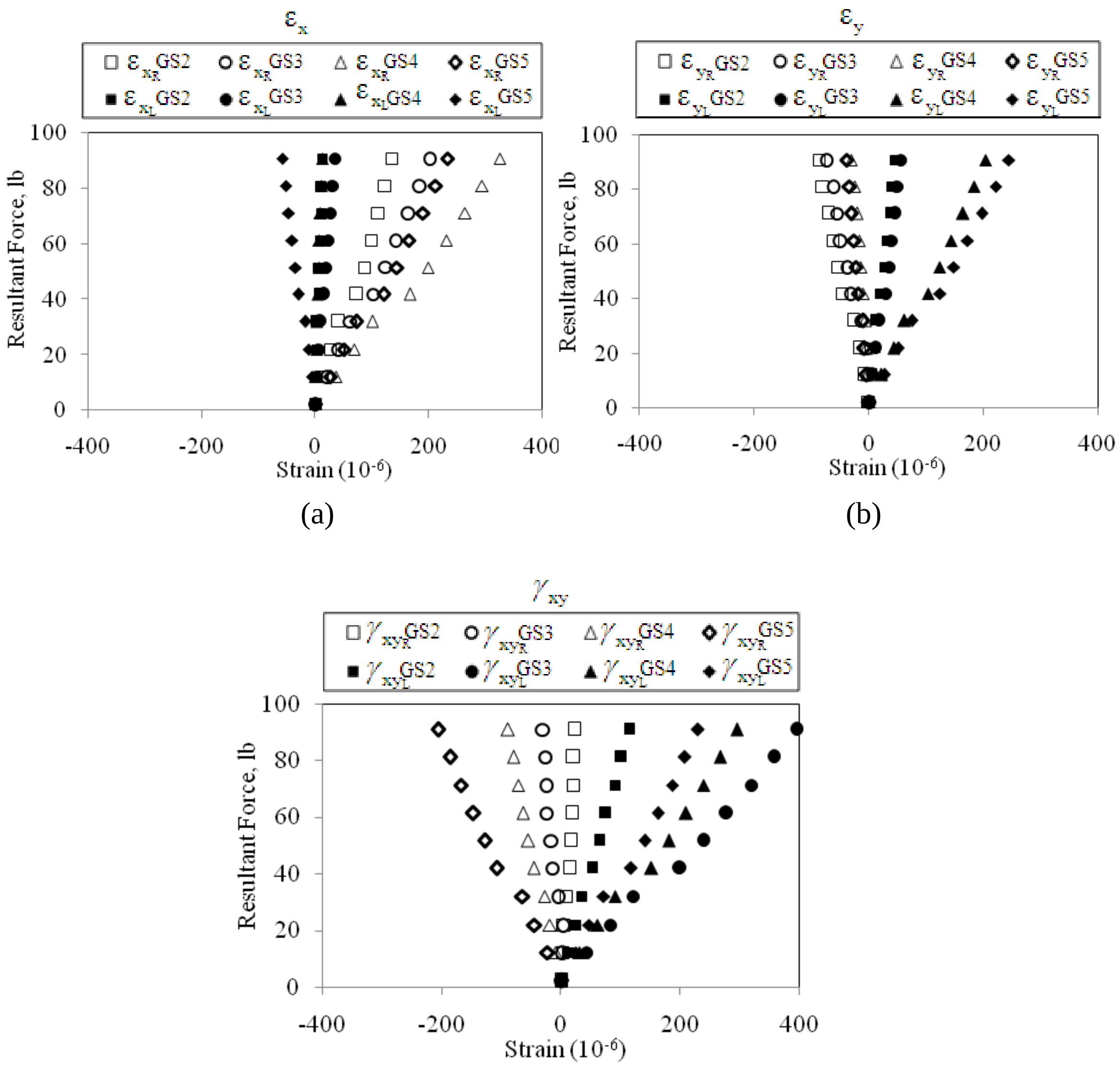

(a) (b)

(c)

Figure 4.28

Measurements of (a) ε_x ,(b) ε_y , and (c) γ_{xy} from eccentric pull-down loading

Table 4.7

Maximum strain readings at 100 lb eccentric pull-down loading

Strain		Strain value (10^{-6})	Station
Right	ε_x	324.6	GS4
	ε_y	-87	GS2
	γ_{xy}	-205.6	GS2
Left	ε_x	57.8	GS5
	ε_y	244.8	GS5
	γ_{xy}	395.2	GS3

All plots show linear trends and the right side longitudinal strains remain positive, with a maximum value of approximately $324.6\text{x}10^{-6}$ strain at GS4. The left side longitudinal strains are seen to progress from positive to negative, achieving a maximum magnitude of $57.8\text{x}10^{-6}$ strain at GS5.

All transverse strains of the right gauges are found to be negative, having similar readings at GS4 and GS5, whereas the left side transverse strains are positive and increase to the maximum value of $244\text{x}10^{-6}$ strain at GS5. It is seen that the trends of shear strains are similar to those of transverse strains where all left strains are negative and all right strains are positive.

Figure 4.29 shows the response from the rosette strain gauges for eccentric push-up loading at the five gauge stations. As seen in the plots, the longitudinal strain of right gauges slightly shifts from negative to positive. Although the left longitudinal strains remain negative at all gauge stations, their magnitude increases from GS2 to GS4 before decreasing at GS5. Also at this gauge station, GS5, the transverse strains from the right gauges are at the maximum values of $-243.9\text{x}10^{-6}$ strain, similar in magnitude to the longitudinal strain of the left gauges and shear strain of the right gauges. The transverse strains from the left side are positive at all gauge stations and continue to increase from GS1 to GS5 achieving a maximum of 244x10^{-6} strain. The shear strain of right gauges are at their maximum at GS3 but their magnitude decreases at GS4 and GS5.

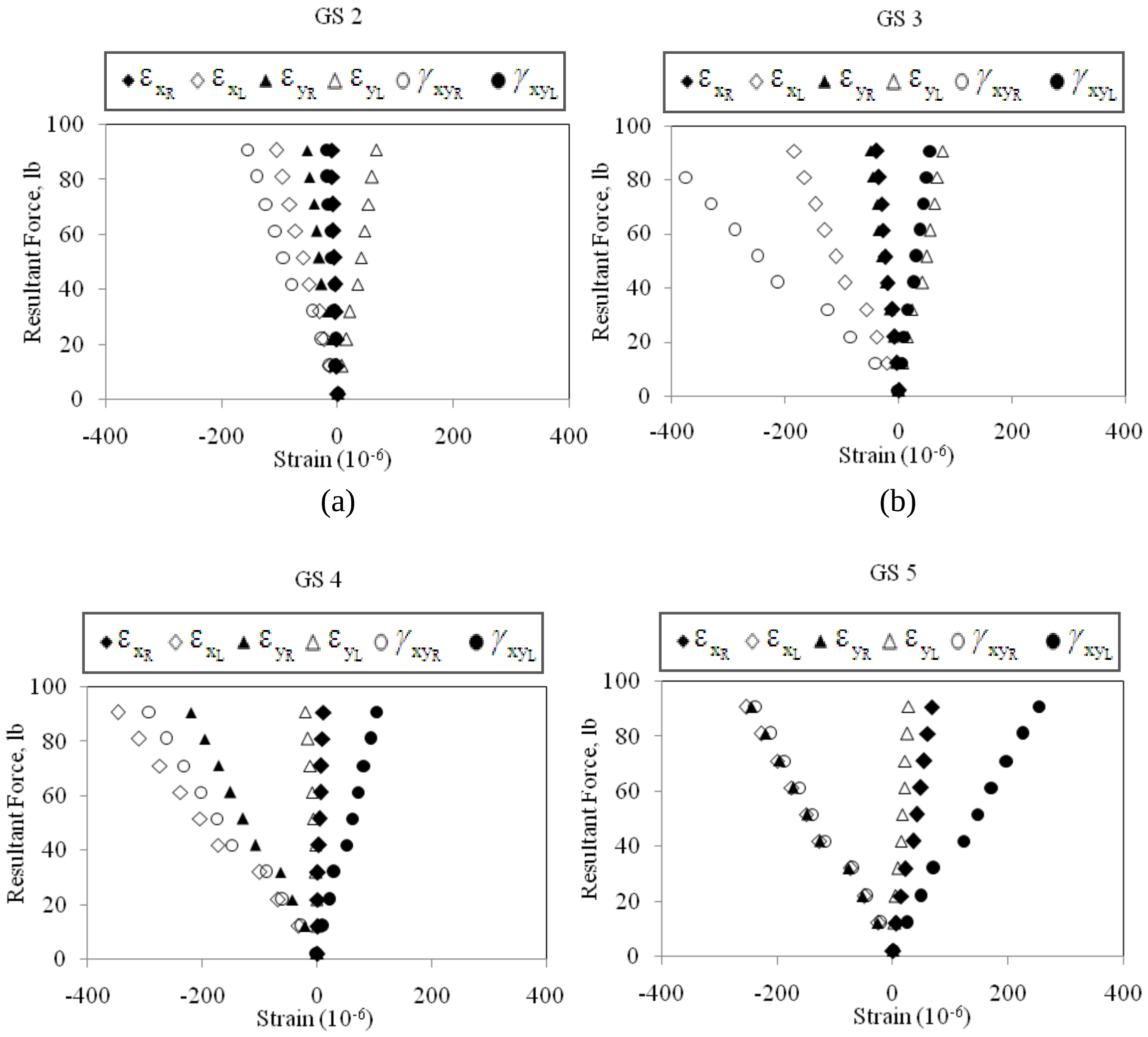

(a)

(b)

(c)

(d)

Figure 4.29

Strain measurements from eccentric push-up loading at (a) GS2, (b) GS3, (c) GS4, and (d) GS5

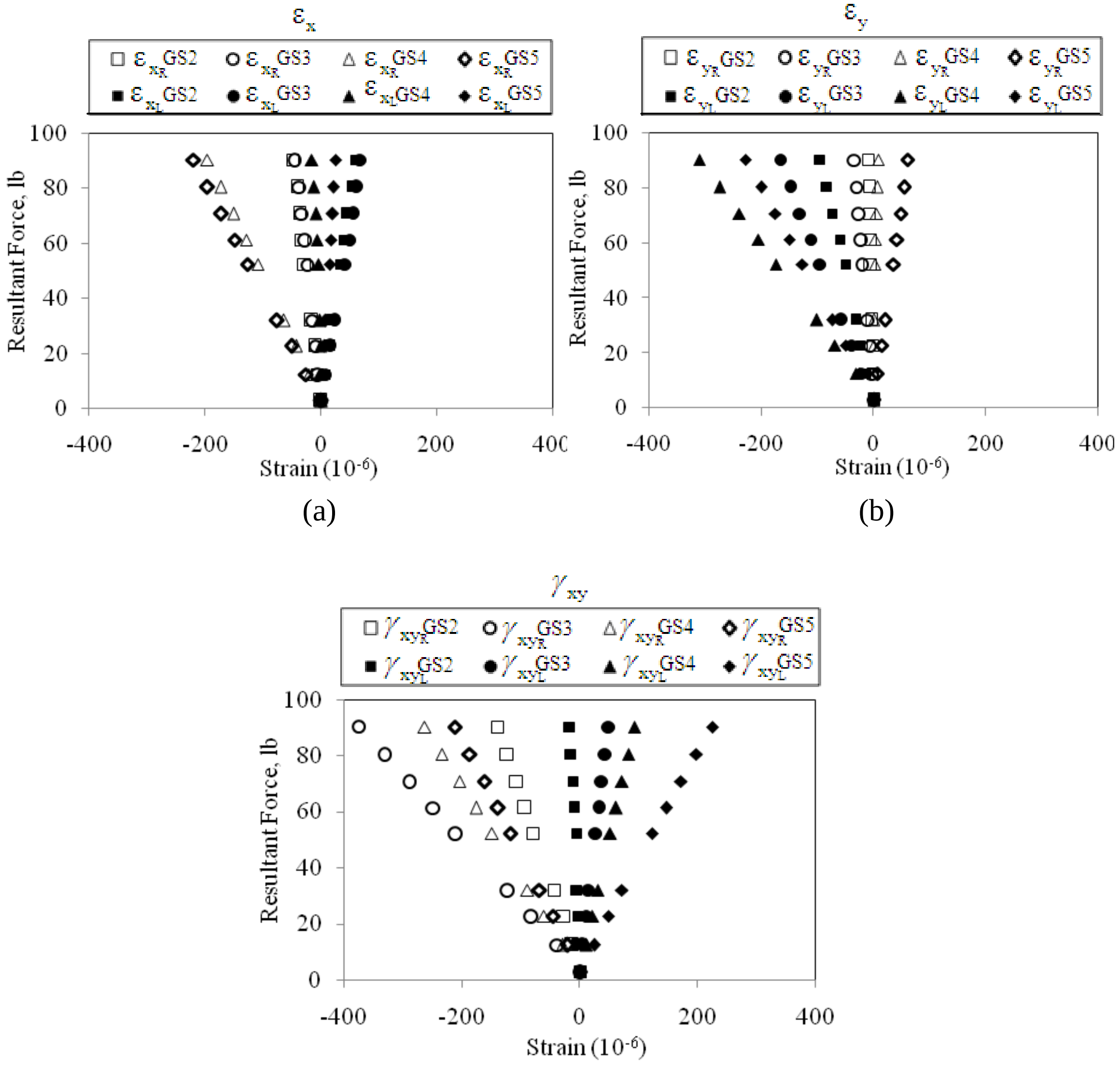

(a)

(b)

(c)

Figure 4.30

Measurements of (a) ε_x ,(b) ε_y , and (c) γ_{xy} from eccentric push-up loading

Table 4.8

Maximum strain readings at 100 lb eccentric push-up loading

Strain		Strain value (10^{-6})	Station
Right	ε_x	60	GS5
	ε_y	-243.9	GS5
	γ_{xy}	-418.1	GS3
Left	ε_x	-347.3	GS4
	ε_y	76.7	GS3
	γ_{xy}	252.4	GS5

To observe the relationship between the static responses of the fuselage/tail structure subjected to the eccentric pull-down and push-up loadings, the strain data is plotted at each gauge station at 10 loading increments from 10 lb to 100 lb. The comparisons between the strains from both loadings are conducted and some selected cases are shown. For example, the left longitudinal strains from the eccentric pull-down loading are compared to the right longitudinal strains from push-up loading (Figure 4.31), the right transverse strains from pull-down loading are compared to the left transverse strains from push-up loading (Figure 4.32), and the right shear strains from pull-down loading are compared to the left shear strains from push-up loading (Figure 4.33). The straight lines connecting the makers are added to these plots to aid in the visualization of the symmetric trend of the data for the two cases.

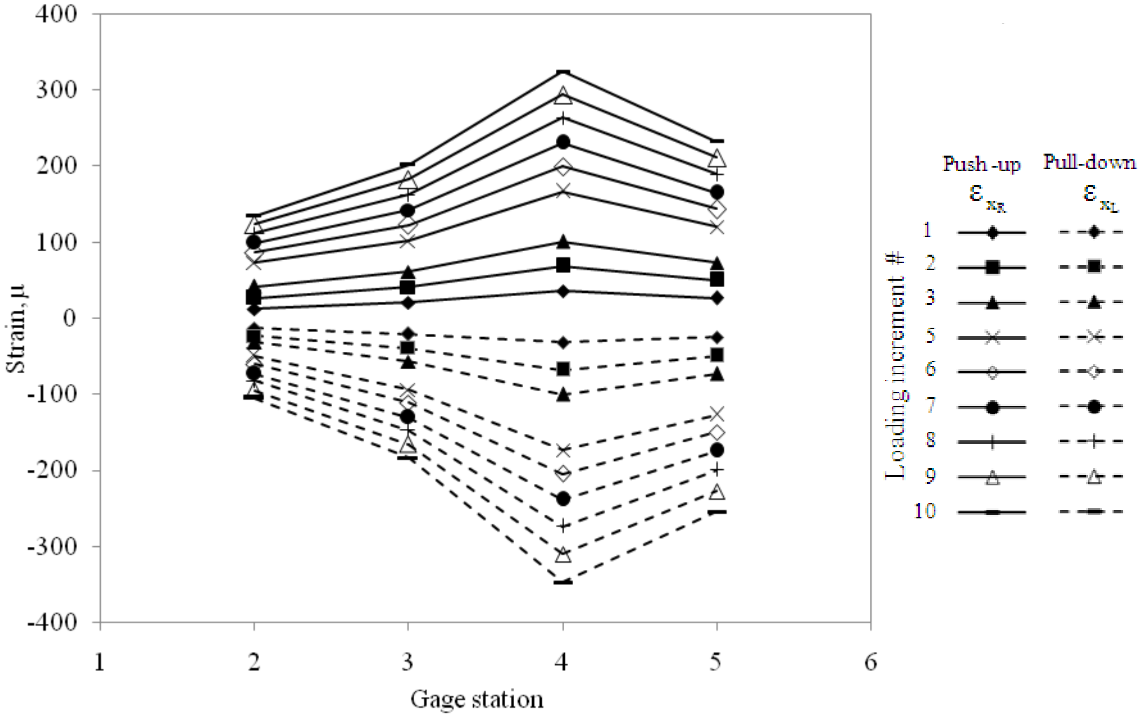

Figure 4.31

Comparison between the left longitudinal strains from pull-down and the right longitudinal strains from push-up loading

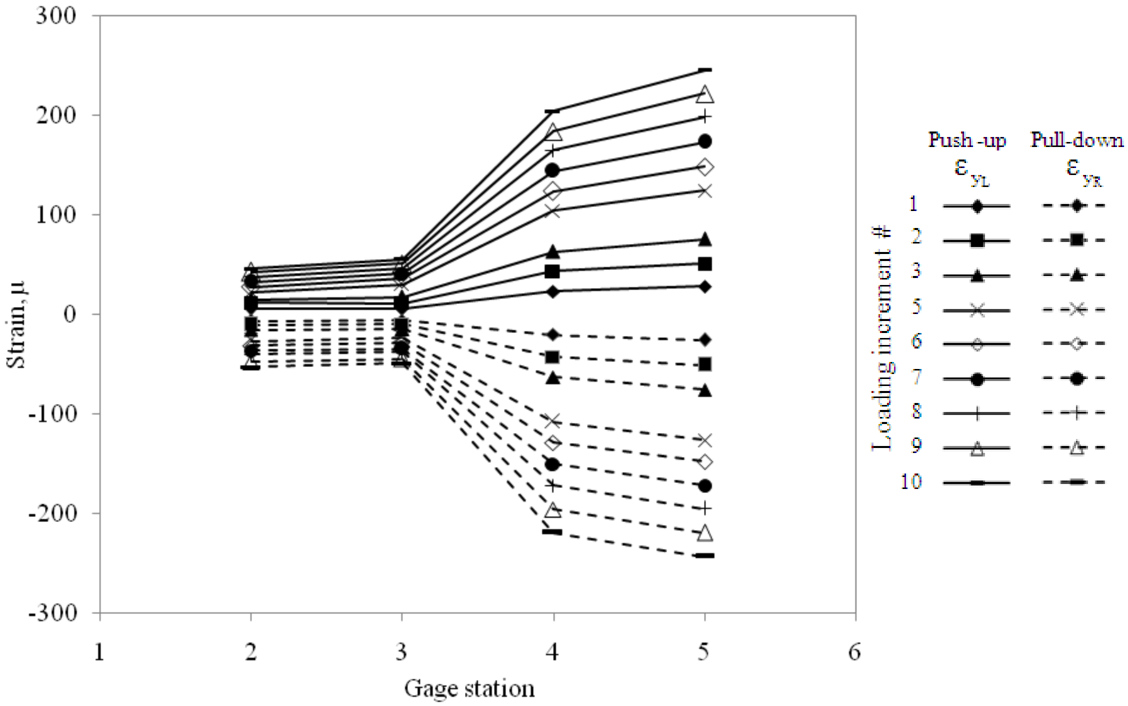

Figure 4.32

Comparison between the right transverse strains from pull-down loading and the left transverse strains from push-up loading

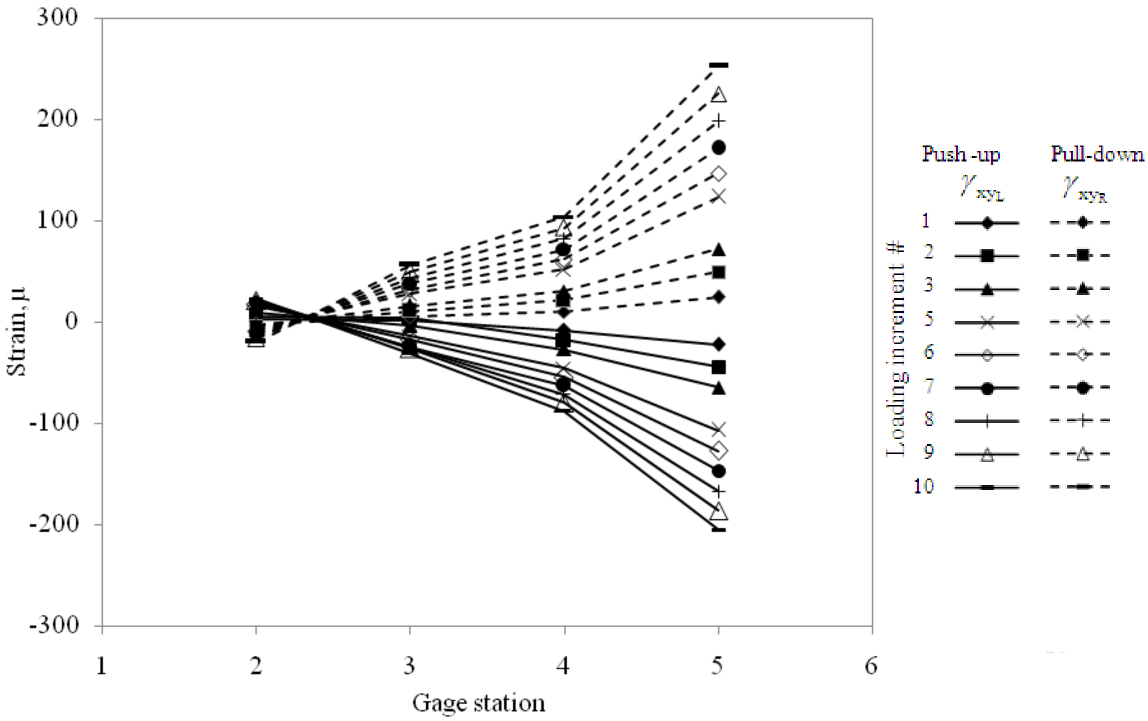

Figure 4.33

Comparison between the right shear strains from pull-down loading and left shear strains from push-up loading

It is interesting to see the comparison in these figures; the magnitudes are found to be similar at each loading increment at each gauge station but with opposite direction. The similarity of the two distinct sets of data (strain reading of the push-up and pull-down loadings) attests the consistency of the strain gauge placement as well as the loading methodology. The maximum strains are easily observed in these plots. In Figure 4.31, it is apparent that the largest longitudinal strains for both push-up and pull-down loadings occur at GS4, which is expected as explained earlier in the simple strain analysis of a tapered cantilevered beam (see Figure 4.26). Because the eccentric loads are applied to the left side of the test structure, all strain readings from the left side of the fuselage are slightly larger than those from the right side. As proven in these figures, minimal responses at all loading increments are also expected at GS2, which locates close to the fixed point (fuselage-wing interconnection region). Also, it appears that non-linearity along the gauge stations increases as the load increases for all strain responses. The changing in strain direction is also visible as seen in Figure 4.33.

CHAPTER 5

VIBRATION TESTING

The vibration tests of an ultralight UAV composite wing and fuselage/tail are conducted to obtain the modal characteristics, which includes the resonant frequencies, modal shapes, and damping coefficients. A shaker-table approach is used for the vibration testing of the wing which uses a specially designed track system to shake the wing to induce lateral and chord-wise oscillations. The modal characteristics of the fuselage structure are determined for a free-free configuration, which is simulated by suspending the test structure from its wing attachment points through the use of springs.

5.1 Analytical Methodology

One of the tools used for obtaining modal properties of a structure is through the use of transfer functions in the frequency domain called frequency response functions (FRFs)[22-25]. These functions can be based on the displacement (admittance, compliance, or receptance), velocity (mobility) or acceleration (inertance or accelerance) response of the system. In this study, the resulting transfer function, based on the acceleration response known as the accelerance, is depicted by the linear model shown in Figure 5.1.

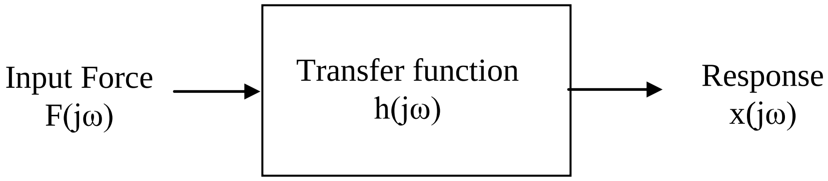

Figure 5.1

Linear model for FRF

The functions shown in Figure 5.1 are complex functions that can be represented by real and imaginary components or in terms of magnitude and phase. From this model, it is seen that the transfer function h(jω), is simply the ratio of the spectrum of the response signal x(jω) to the spectrum of the applied force signal F(jω), and can be expressed as

$$\mathrm{h}(\mathrm{j}\omega) = \frac{\mathrm{x}(\mathrm{j}\omega)}{\mathrm{F}(\mathrm{j}\omega)} \tag{5.1}$$

Two types of vibration measurement techniques, frequency sweep and frequency dwell at the sampling rate of 500 Hz and traversed rate of 0.8 Hz, are conducted to obtain the modal characteristics of the structure. Using the acceleration data at zero voltage and the accelerometer’s calibration value, g load data is calculated. To obtain the frequency spectrums x(jω) and F(jω), the discrete frequency transform (DFT) of the input signal (applied force) and the output response (acceleration) from each channel is computed from

$$c_j = \frac{1}{n}\sum_p d_p e^{i\left(\frac{2\pi j}{n}\right)p} \tag{5.2}$$

where

n = number of elements in d_p vector

d_p = input or output response vector, $x(j\omega)$ or $F(j\omega)$

c_j = complex Fourier coefficient

The amplitude of the signal can be extracted from the magnitude of the complex Fourier coefficients. The frequency corresponding to the pth element in the calculated transfer function is given by

$$f_p = \frac{p}{n} f_s \tag{5.3}$$

where

f_s = the sampling frequency of the original signal

Once the DFT of each signal is obtained, the transfer function is computed. Both the resonant frequencies and the corresponding mode shapes are obtained from the plot of the imaginary component of the resulting FRFs. The deflection shape at each natural frequency can also be determined by using the double integration technique on the response signal. In this, the frequency dwell time-domain response at each resonant frequency for each channel is integrated twice to obtain the displacement at a single moment in time to obtain the mode shapes.

The damping ratio ξ, which is defined as the natural tendency of the structure to return to an equilibrium state after being oscillated, is determined for each resonant frequency. Half power points, which correspond to frequencies ω_1 and ω_2 as shown in Figure 5.2, can be used to determine the damping ratio using

$$\xi = \frac{\omega_2 - \omega_1}{2\omega_n} \tag{5.4}$$

where

ω_n = resonant frequency of the structure

$\omega_2 - \omega_1$ = frequency bandwidth that is located at 0.707 times the peak amplitude

The structural damping coefficient, which is simply twice the damping ratio, is also computed.

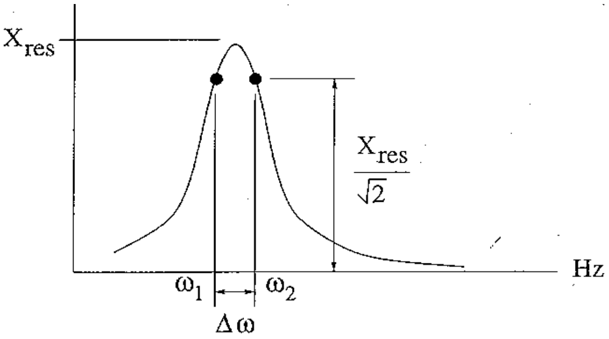

Figure 5.2

Frequency bandwidth of half power points method

5.2 Wing Assembly Testing

5.2.1 Experimental Set Up and Procedure

A shaker-table approach was used for the vibration testing of the wing structure. The wing was cantilevered at the stub spar (carry through structure) using the specially designed vibration fixture that consists of the support fixture (Figure 5.3a) and track systems (Figure 5.3b and 5.3c). This vibration fixture is designed to travel over the smooth track system during testing. Due to the vertical placement of the wing, the load requirement on the shaker is minimized because it only needs to overcome the friction force at the support rollers.

Because the main spar is tapered, a wooden wedge was used to properly mount the wing in the support fixture. Two large bolts were used to secure the spar and wooden piece to the support fixture. The support fixture, shown in Figure 5.3a, was placed on the appropriate track system (Figure 5.3b or 5.3c) to excite the test article in the desired direction. The dynamic response of the wing is obtained from the x direction for the in-plane (chordwise) excitation and in the y direction for the out-of-plane (lateral) excitation, as illustrated by the coordinate system in Figure 5.3a.

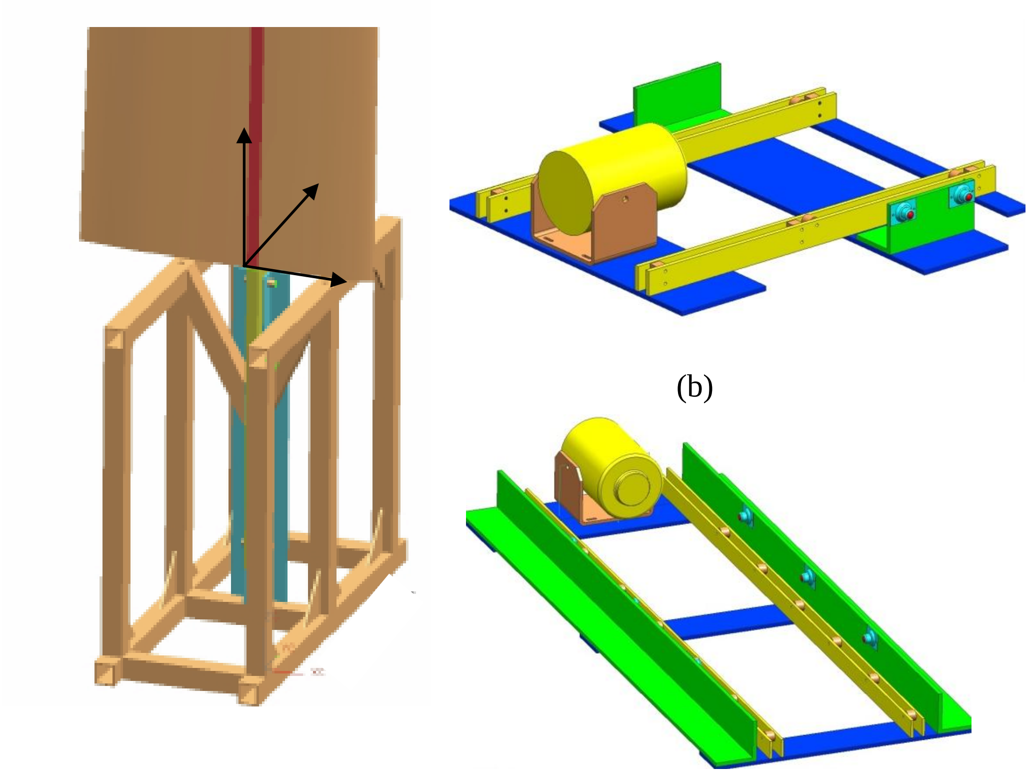

(b)

(a)

(c)

Figure 5.3

(a) Support fixture (b) Track system for in-plane excitation
(c) Track system for out-of-plane excitation

The set up of the vibration test assembly is further illustrated in Figure 5.4 and 5.5 for the in-plane and the out-of-plane vibration, respectively. Shown in these figures, the excitation to the structure is induced by a single shaker unit that is mounted on the ground at the center between the two tracks. The shaker unit, with a vibration isolation mount, is connected to a load cell through a thin steel rod and located at the center of gravity of the wing-support fixture. It is critical for the shaker unit to be perfectly aligned in both x and z directions (using coordinate system in Figure5.3a) to avoid damaging the shaker system during testing.

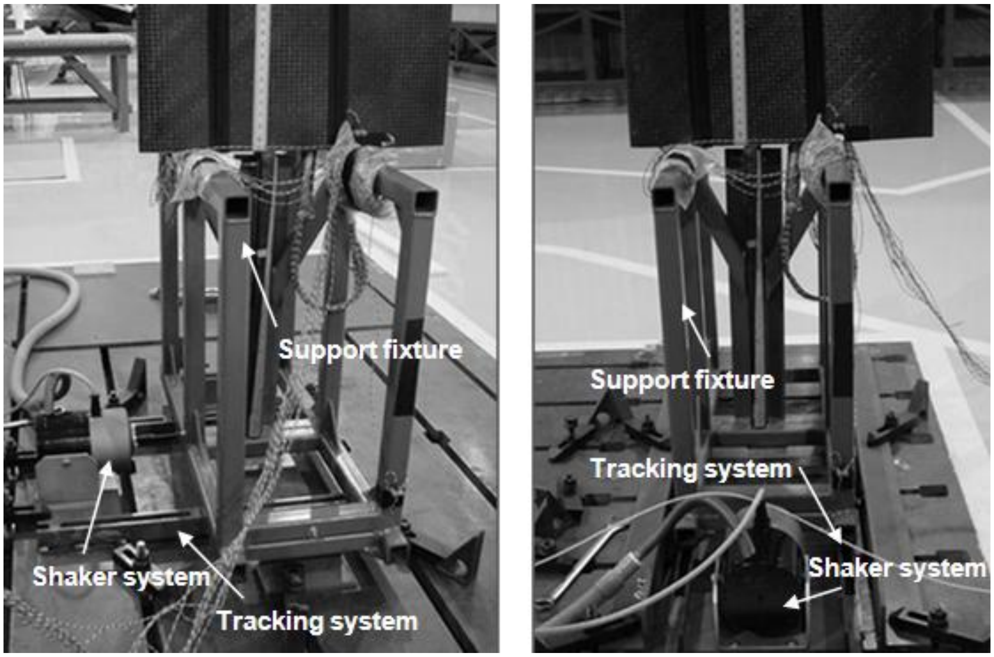
Support fixture
Shaker system
Tracking system
Support fixture
Tracking system
Shaker system

(a) (b)

Figure 5.4

Wing vibration test fixture for (a) in-plane excitation (b) out-of-plane excitation

The vibration testing is performed on two sets of wings. Both wings are right wings and nearly identical except that wing #1 (Figure 5.5a) has the aileron and spoiler cutouts while wing #2 (Figure 5.5b) is painted and has no aileron cutout. To obtain the vibration characteristics, the wing is instrumented with 19 dual-axis accelerometers (ADXL321), which have an average sensitivity of 0.057 mV/g and a range of ±18 g. Prior to testing, each accelerometer is calibrated to determine its sensitivity and mounted onto a composite angle bracket. Using double-sided adhesive tape, these dual axis lightweight accelerometers are attached to the wing surface with one axis of the accelerometers along the chordwise direction and the other axis normal to the surface of the wing. Much care was taken to insure proper alignment and mounting of the sensors to the wing surface. To identify the location of the sensors, an adhesive ruler was attached on the wing surface over the main spar, from the root to the wing tip. Seventeen accelerometers, identified by A1 through A17 in Figure 5.5, were mounted at nine spanwise stations on the wing surface. These were evenly spaced from the root to the tip of the wing, while the remaining accelerometers (A18 – A19) were located on the fixture. Therefore, a total of thirty-eight discrete-point accelerations were measured and recorded. The swept sine technique is used and frequency sweeps from 2 Hz to 100 Hz were conducted at a sampling rate of 500 Hz.

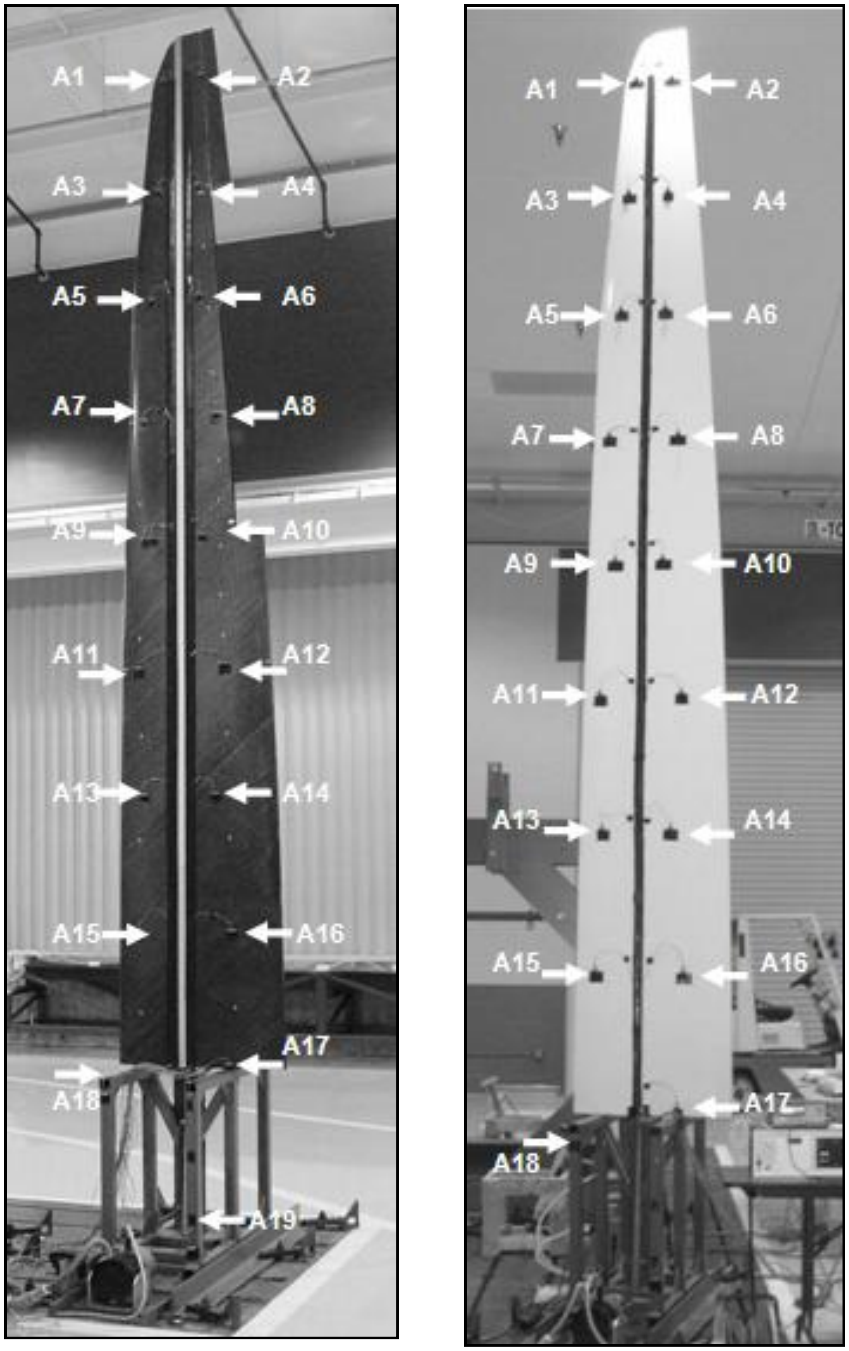
A1
A2
A3
A4
A5
A6
A7
A8
A9
A10
A11
A12
A13
A14
A15
A16
A17
A18
A19
A1
A2
A3
A4
A5
A6
A7
A8
A9
A10
A11
A12
A13
A14
A15
A16
A17
A18

(a) (b)

Figure 5.5

Vibration test set up with accelerometers for (a) Wing #1 (b) Wing #2

5.2.2 Data Acquisition System

The data acquisition set up for the vibration testing of both wing and fuselage structures is shown in Figure 5.6. Single input excitation, provided by the arbitrary waveform function generator at the specified frequencies, was used to activate the shaker amplifier and excite the 110 lb capacity shaker unit. A load cell and a dynamic force transducer were connected in series with the shaker to obtain the input force signal to the test structure. Careful consideration was taken to properly balance and mount the test structure because excessive lateral movement of the test article can cause damage to the delicate shaker unit and force transducer. The open loop system records the acceleration data for either a range of frequencies or a particular frequency at user selected sampling rates through a LabVIEW® program.

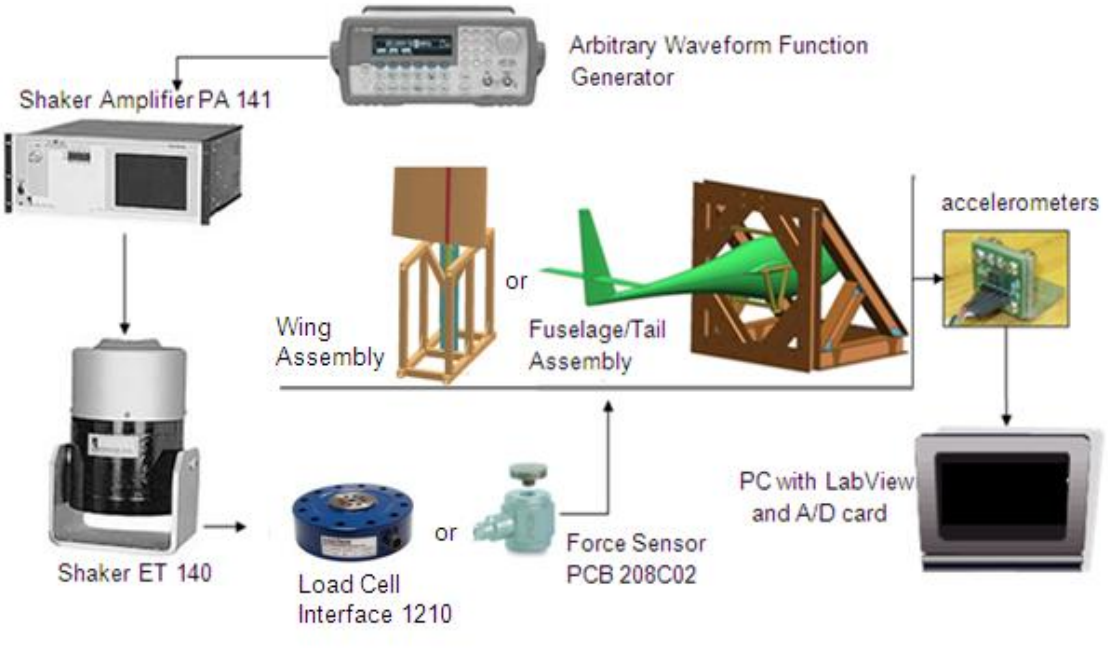
Arbitrary Waveform Function Generator
Shaker Amplifier PA 141
accelerometers
or
Wing Assembly
Fuselage/Tail Assembly
PC with LabView and A/D card
or
Shaker ET 140
Load Cell Interface 1210
Force Sensor PCB 208C02

Figure 5.6

Vibration data acquisition system

To obtain the modal parameters, the input force signal and the response from each sensor is recorded for later processing. Detailed description of each apparatus used in vibration data acquisition is given in the Appendix A.

5.2.3 Results and Discussion

Using the accelerometers calibration data, frequency data at zero Hz, and output signals, the g-load data for two frequency ranges are computed. The frequency ranges were 0 Hz to 50 Hz and 50 Hz to 100 Hz, which were obtained from 19 accelerometers from Wing #1 and 18 accelerometers from Wing #2. Initial results from the vibration testing of Wing #2 showed that accelerometer A19 was not working properly due to its inconsistency of output data, and therefore, it was eliminated. Therefore, the data from the remaining 18 accelerometers was analyzed for Wing #2.

The Discrete Fourier Transform (DFT) from the frequency sweep time-domain data was performed on the g-load data to calculate the amplitude of each accelerometer signal. The natural frequencies were then extracted from the peak amplitudes of the frequency spectrum of each channel. The frequency responses from the wing lateral vibration testing are depicted in Figure 5.7 through 5.10. Figure 5.7 shows the in-plane (chordwise) response of accelerometers A1 and A2, which were located close to the wing tip (see Figure 5.5), and accelerometers A5 and A6, which were located about midspan. Figure 5.8 shows the out-of-plane response of the accelerometers A1, A2, A5 and A6. Similarly, for Wing #2, the frequency spectrums of the accelerometers (A1, A2, A5, and A6) are illustrated in Figures 5.9 and 5.10. Similar plots showing the response of the accelerometers obtained from the chordwise vibration testing of both wings can be found in Appendix C.

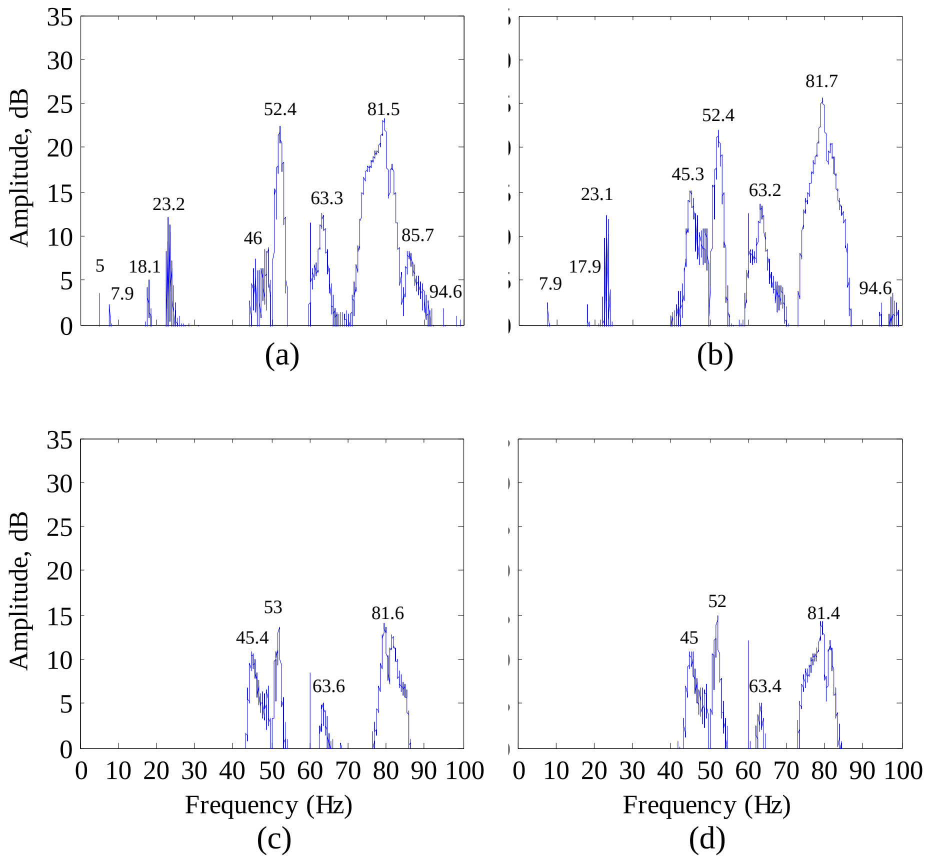

(a) (b)

(c) (d)

Figure 5.7

Frequency spectrum based on in-plane (chord-wise) acceleration measurements at accelerometer location (a) A1, (b) A2, (c) A5, and (d) A6 of Wing # 1

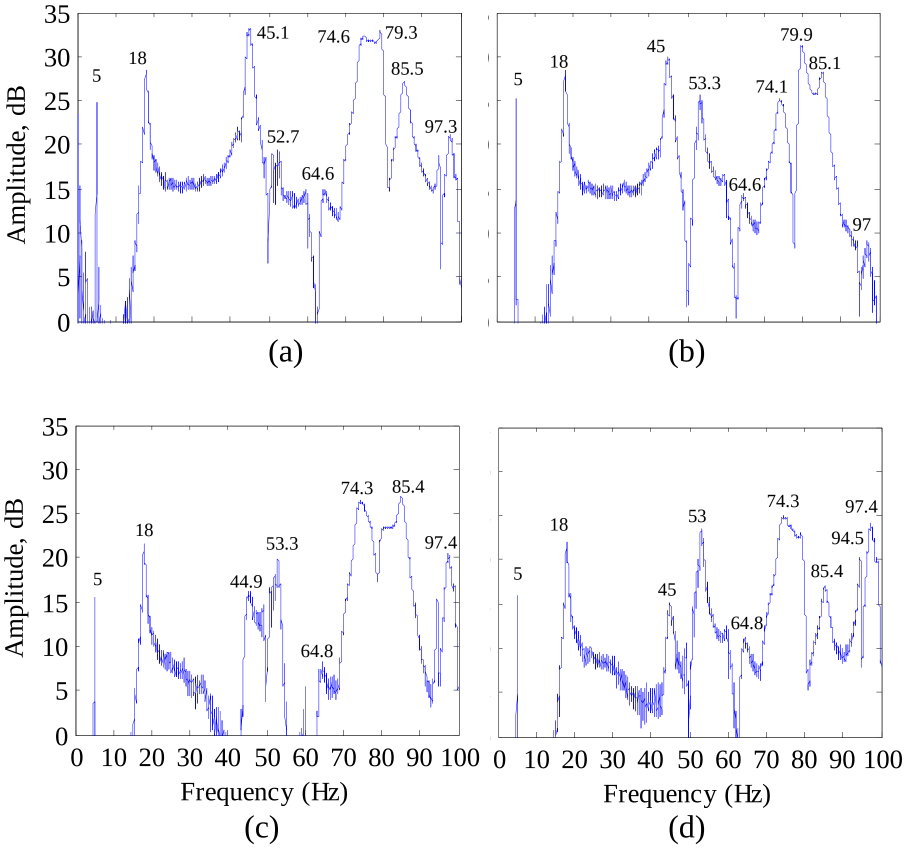

Figure 5.8

Frequency spectrum based on out-of-plane acceleration measurements at accelerometer location (a) A1, (b) A2, (c) A5, and (d) A6 of Wing # 1

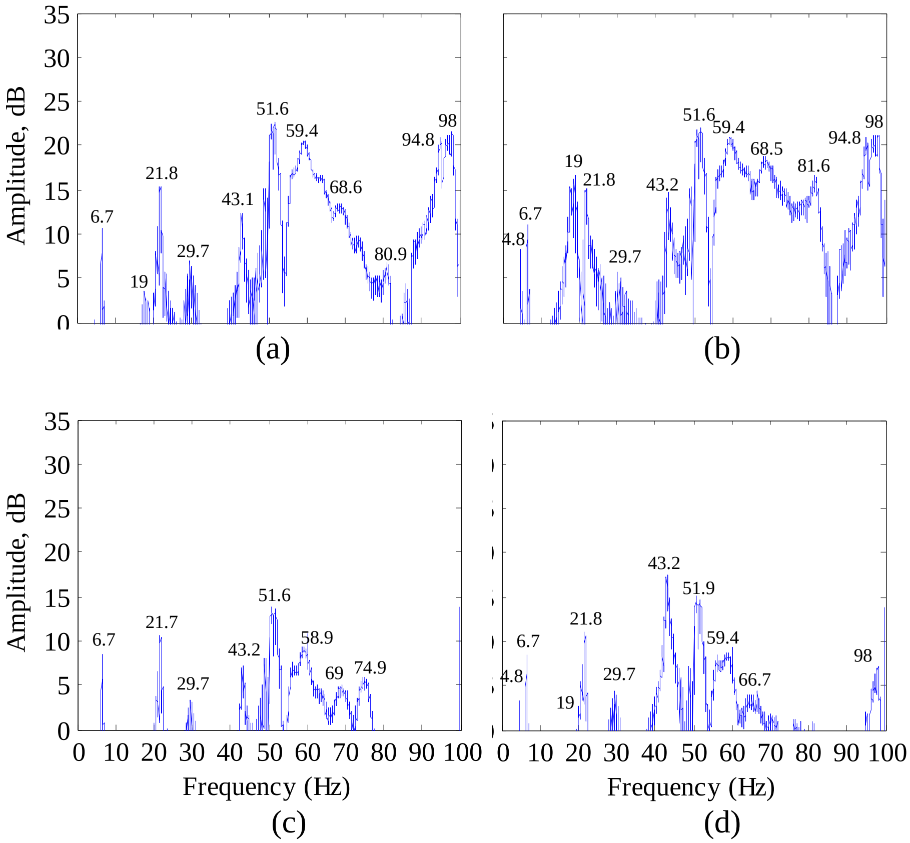

Figure 5.9

Frequency spectrum based on in-plane (chord-wise) acceleration measurements at accelerometer location (a) A1, (b) A2, (c) A5, and (d) A6 of Wing # 2

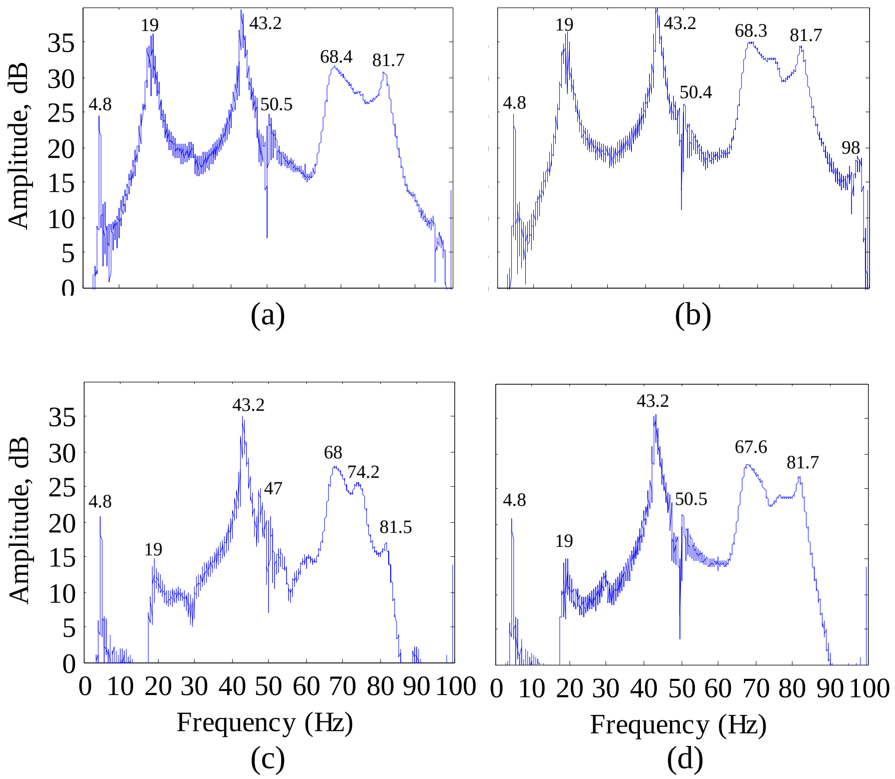

Figure 5.10

Frequency spectrum based on out-of-plane acceleration measurements at accelerometer location (a) A1, (b) A2, (c) A5, and (d) A6 of Wing # 2

As expected, the maximum response occurs at the location of accelerometer A1 and A2, which are mounted at the wing tip. The peaks in Figures 5.7 through 5.10 correspond to the natural frequencies of the system. The frequency response plots of other sensors, which are obtained from g-load data in both the chordwise and normal to spanwise directions, are similar to these figures. While some peaks are present in all figures, others appear in only a few. For example, the first natural frequency of Wing #1 at 5.03 Hz is evident primarily in all the channels that are oriented normal to the surface of the wing; therefore, 5.03 Hz is the first structural vertical bending frequency. On the other hand, the first chordwise (horizontal) bending of 7.92 Hz appears only in the in-plane channels. Both of these frequencies can be visually observed. Other peak frequencies, such as around 53 Hz of Wing #1, appear in both in-plane and out-of-plane channels indicating a combination of modes. The list of peak frequencies found from each sensor based on in-plane and out-of-plane acceleration measurements below 100 Hz are tabulated in Tables 5.1-5.2 for Wing #1 and Table 5.3-5.4 for Wing #2.

Table 5.1

List of peak frequencies of in-plane channels of Wing #1

Accel #	**Peak Frequency (Hz)**											
1	5.0	7.9	18.1	23.2	46.0	52.4	63.3		81.5	85.7	94.6	
2		7.9	17.9	23.1	45.3	52.4	63.2		81.7		94.6	
3		7.9		23.2		53.0			82.0	85.0		
4		7.9		23.3	45.0	53.0						
5					45.4	52.0	63.6		81.6			
6					45.0	52.0	63.4		81.4			
7					45.1	52.0	63.5		81.3	85.6	94.6	97.3
8					45.2	52.0	63.4		81.7	85.1		
9					45.2	52.0	63.3		81.4			
10				23.2		52.1			81.3			
11	5.0	7.9		23.3	45.4	52.4	63.6		81.7			97.3
12		7.9		23.0	45.2	52.7	63.5					
13				22.8	45.4	52.0	63.6	73.7	81.9	85.4	94.6	
14				23.1	45.1	52.0	63.5		81.5			
15					45.1	52.0	63.6		81.6			97.7
16					45.2	52.0	63.6		81.5			
17				23.2	45.3	52.0		74.3		84.6	94.5	97.2
18					46.0	52.0				85.1	94.6	97.3

Table 5.2

List of peak frequencies of out-of-plane channels of Wing #1

Accel #	**Peak Frequency (Hz)**									
1	5.0	18.0	45.1	52.7	64.6	74.6	79.3	85.5	94.5	97.3
2	5.0	18.0	45.0	53.3	64.6	74.1	79.9	85.1	94.2	97.0
3	5.0	17.9	44.9	53.0	64.6		79.4	85.0	94.6	97.7
4	5.0	18.0	45.5	53.0	64.4	75.1	80.1	85.3	94.5	97.7
5	5.0	18.0	44.9	53.3	64.8	74.3	79.3	85.4	94.6	97.4
6	5.0	18.0	45.0	53.0		74.7	79.3	85.2	94.5	
7	5.0	18.0	45.0	53.0		74.5	79.7	85.3	94.4	97.7
8	5.0	18.0	44.9	53.0	64.8	74.5	79.2	85.2		97.4
9		17.9		53.0	64.7	74.2		85.4	94.5	97.1
10	5.0	18.0	45.0	53.2	64.8	74.3	79.7	85.3	94.5	
11	5.0	18.0	45.2	53.0	64.6	74.7	79.3	85.5		97.4
12	5.0	18.0	45.0	53.2		74.7	79.1	85.4	94.5	
13	4.9	18.0	44.9	53.0		74.3	80.1	85.2		97.7
14	5.0	18.0	44.9	52.7	64.2	73.6	79.6		94.5	97.4
15	5.0	18.0	45.1	53.3	64.8	74.2	79.7	85.0	94.5	97.4
16	5.0	17.9	45.0	53.3	64.4	74.7		85.1	94.6	97.4
17		17.9	44.6	53.3	64.8	73.8	79.7	85.2	94.5	97.3
18		17.9			64.4	74	79.6	85.3		97.4

Table 5.3

List of peak frequencies of in-plane channels of Wing #2

Accel.	**Peak Frequency (Hz)**												
1		6.7	19.0	21.8	29.7	43.1	51.6	68.6		80.9	86.0	94.8	98.0
2	4.8	6.7	19.0	21.8	29.7	43.2	51.6	68.5		81.6		94.8	98.0
3	4.8	6.7		21.8	30.1	43.2	51.5	69.0	75.1	81.7		94.8	98.1
4	4.8	6.7	19.0	21.8	29.7	43.2	51.6	64.4		81.9	88.2	94.8	97.3
5		6.7		21.7	29.7	43.2	51.6	69.0	74.9				
6	4.8	6.7	19.0	21.8	29.7	43.2	51.9	66.7					98.0
7								67.8		81.5			
8	4.8	6.7	19.0	21.6	29.7	43.1		68.4		81.9		94.9	98.0
9	4.8	6.7		21.8	30.1	43.2	51.6			82.7	86.0	94.8	98.0
10	4.8	6.7	19.0		29.8	43.4	51.6	66.9		82.5		94.9	98.0
11		6.7	19.0			43.2	51.9	68.5		82.6		94.8	98.0
12	4.8	6.7	18.8			43.2	51.6	64.4		81.8		94.8	98.0
13		6.7		21.6			51.5			82.7		94.8	98.0
14		6.7		21.7		43.2		68.7		81.7		95.2	97.9
15		6.5		21.7			51.6			82.2		94.9	98.0
16		6.7		21.7		43.2	51.6	68.4		81.8		95.1	98.0
17		6.7		21.7			51.5	67.8					
18				21.6	29.7	43.2	52.0	67.8				95.3	

Table 5.4

List of peak frequencies of out-of-plane channels of Wing #2

Accelerometer	**Peak Frequency (Hz)**								
1	4.8	19.0	43.2	50.5	68.4		81.7		
2	4.8	19.0	43.2	50.4	68.3	74.4	81.7		98.1
3	4.8	19.0	43.2	50.5	68.0	74.0	81.8		97.3
4	4.8	19.0	43.2		67.9		81.8		98.0
5	4.8	19.2	43.2	47	68.0	74.2	81.5	89.6	
6	4.8	19.0	43.2	50.2	67.6		81.7		
7	4.8	19.0	43.2		68.4		81.7		98.0
8	4.8	19.0	43.2	50.5			81.6		
9	4.8		43.2	50.9	67.8	74.8	81.9		97.9
10	4.8	19.0	43.2		67.6		81.7		98.0
11	4.8	19.0	43.2		67.5	73.6	81.8		97.9
12	4.8	19.0	43.2		67.6	76.0	82.2		97.3
13	4.8	19.0	43.2				81.9		98.0
14	4.8	19.0	43.2			74.1	81.9		98.0
15			43.2		67.7		81.7		97.9
16			43.2		68.5		81.6		98.0
17			43.2		67.7				97.9
18			43.2						97.9

Using Equation 5.1, the frequency response functions (FRF) for all accelerometers are computed. To obtain the mode shapes, the magnitude and direction of the imaginary components of the resulting FRFs of each natural frequency at each acclerometer location were determined and plotted. The vibration modes of wing structures at selected natural frequencies of both wings are shown in Figure 5.11.

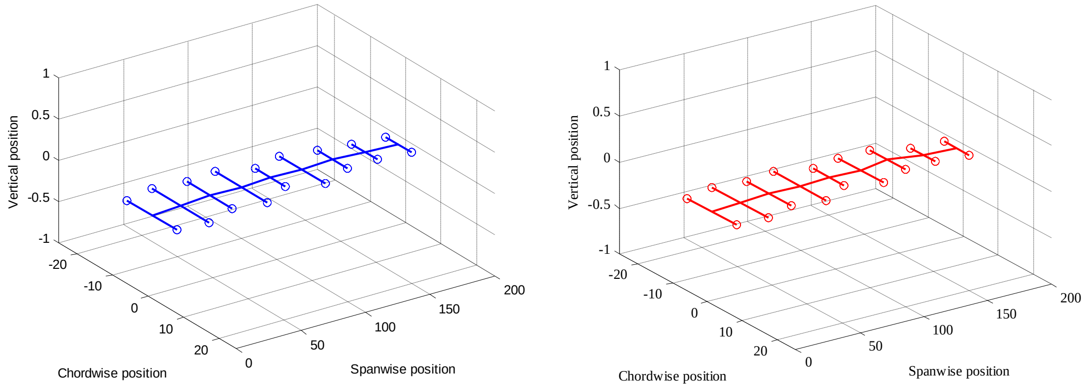

(a) Left: Wing #1 at zero Hz, right: Wing #2 at zero Hz

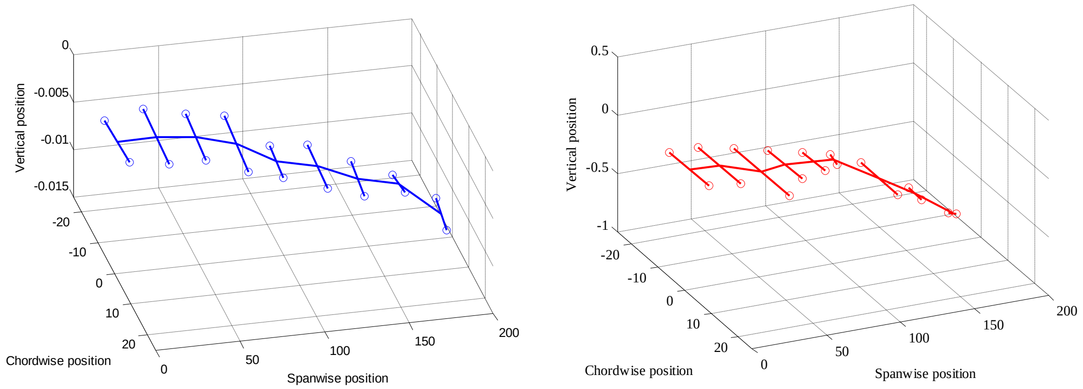

(b) Left: Wing #1 at 5.03 Hz, right: Wing #2 at 4.77 Hz

Figure 5.11

Vibration modes of wing structures at selected natural frequencies

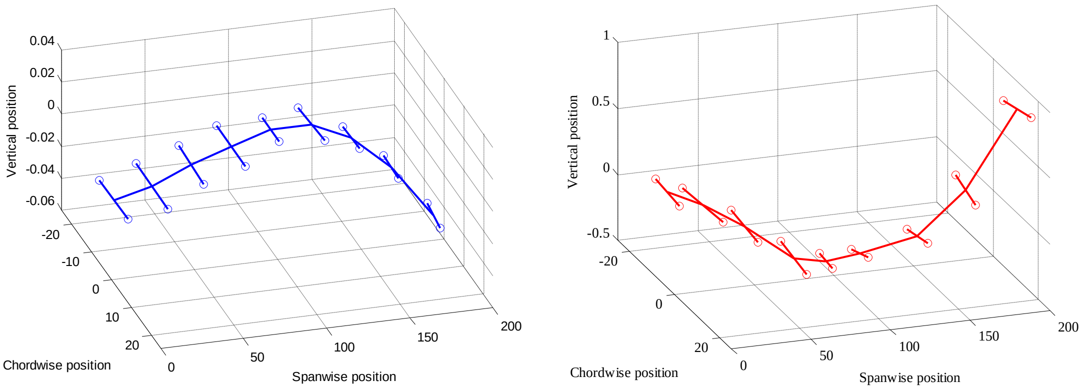

(c) Left: Wing #1 at 23.05 Hz, right: Wing #2 at 21.78 Hz

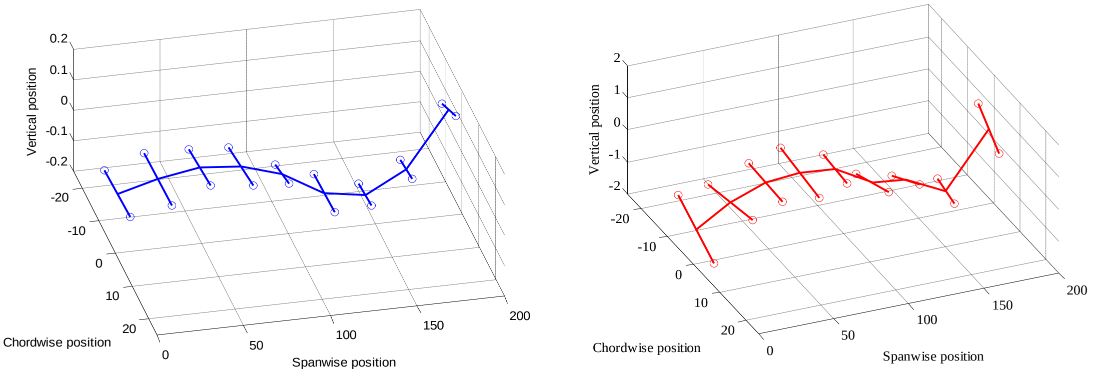

(d) Left: Wing #1 at 44.77 Hz, right: Wing #2 at 43.15 Hz

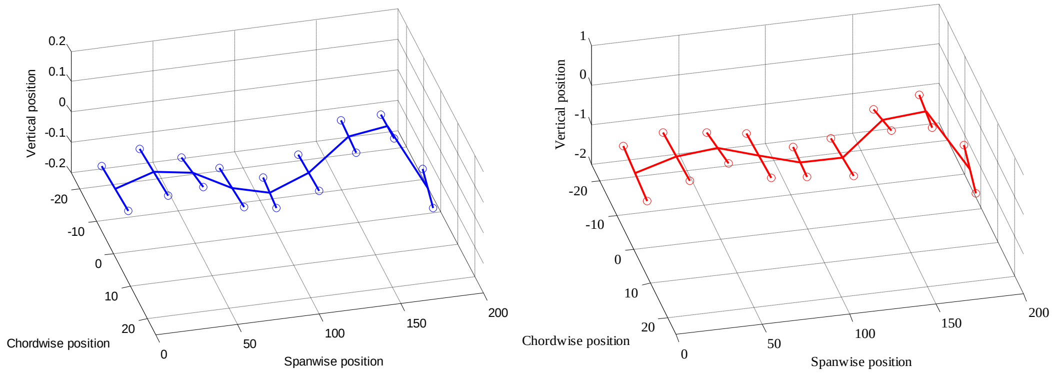

(e) Left: Wing #1 at 74.8 Hz, right: Wing #2 at 74.85 Hz

Figure 5.11 (continued)

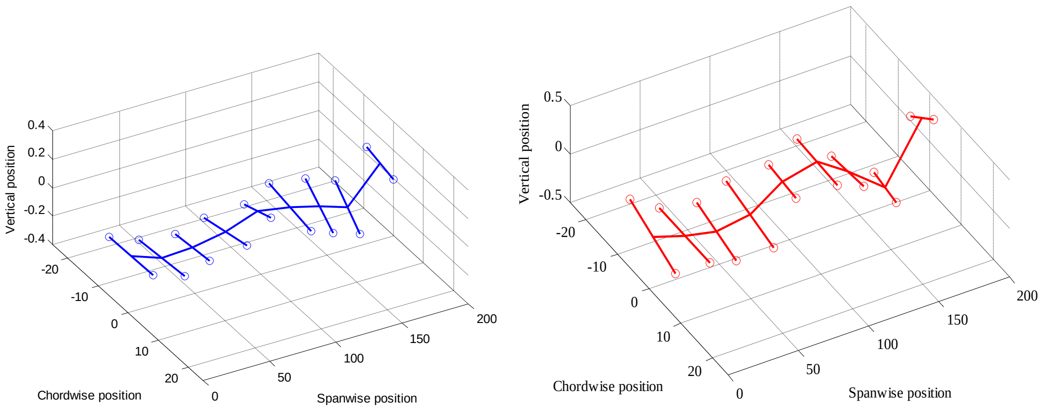

(f) Left: Wing #1 at 85.43 Hz, right: Wing #2 at 81.8 Hz

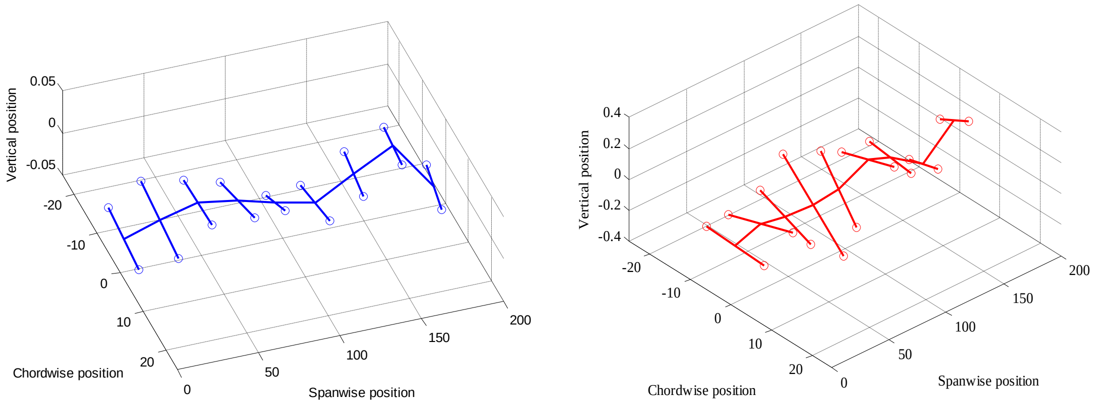

(g) Left: Wing #1 at 97.05 Hz, right: Wing #2 at 97.98 Hz

Figure 5.11 (continued)

As expected, due to the wing geometry and material system, the vibration modes reveal some combination of bending and torsion in the majority of modes. The first mode (Figure 5.11b) is clearly observed during testing and also easily verified. However, for some frequencies, the slight differences of the mode shape between both wings are apparent. For example, at 44 Hz (Figure 5.11d) the vertical bending is indicated as the predominant mode; however, a node location in the mid span of Wing #2 also suggests a lateral bending.

To verify the mode shapes, the frequency dwell testing at selected natural frequencies at the sampling rate of 500 Hz was performed. The g-load data from each channel is integrated twice to obtain the magnitude as well as the direction of the displacements for each channel at a single instant in time. The plots of the mode shapes for three natural frequencies of Wing #2 using the double integration method are compared to those obtained by FRF are shown in Figure 5.12.

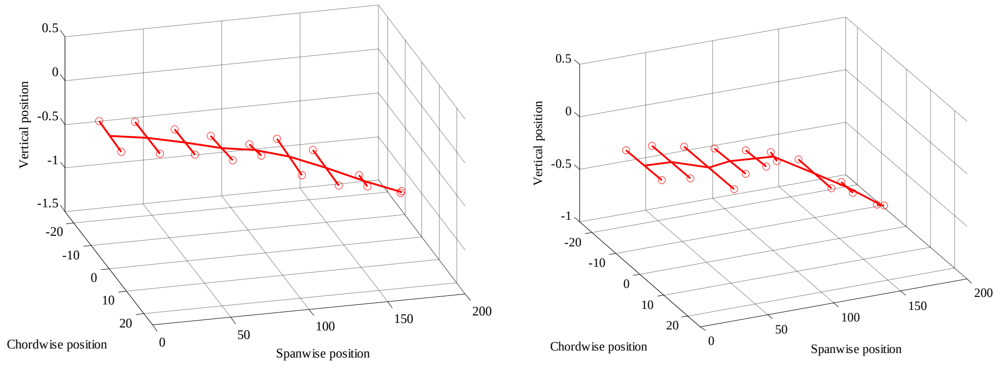

(a) 4.77 Hz

Figure 5.12

Vibration modes of Wing #2 at selected natural frequencies using (left) double integration method and (right) FRF method

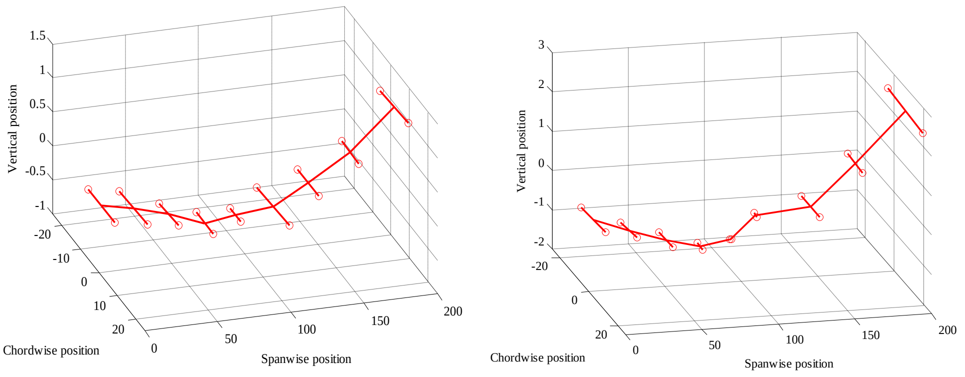

(b) 19 Hz

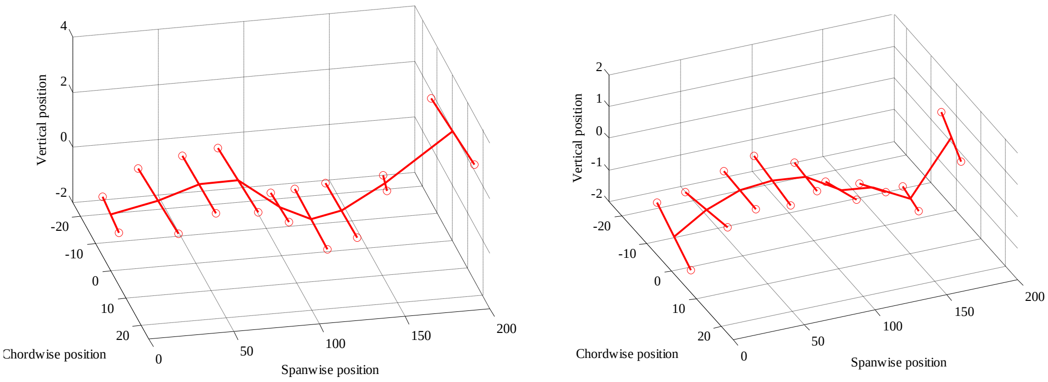

(c) 43.15 Hz

Figure 5.12 (continued)

The mode shapes obtained from both techniques are in a good agreement, thus validating the FRF method. The wing vibration characteristics extracted from the frequency response of all channels are shown in Tables 5.5 and 5.6 for Wing#1 and Wing#2, respectively. The structural damping coefficient is computed for each natural frequency and the deduced dominating mode is also listed in the tables.

Table 5.5

Vibration characteristics of Wing #1

Mode No.	**Observed Mode Shape**	**Natural Frequency, Hz**	**Damping Coefficient**
1	1st vertical bending	5.03	0.023
2	1st horizontal bending	7.92	0.029
3	2nd vertical bending	17.98	0.012
4	3rd vertical bending	23.05	0.058
5	1st torsion	44.77	0.018
6	mixed	53.28	0.069
7	mixed	63.23	0.021
8	mixed	73.8	0.032
9	mixed	79.32	0.037
10	mixed	85.43	0.01
11	mixed	97.05	0.022

Table 5.6

Vibration characteristics of Wing #2

Mode No.	**Observed Mode Shape**	**Natural Frequency, Hz**	**Damping Coefficient**
1	1st vertical bending	4.77	0.059
2	1st horizontal bending	6.68	0.025
3	2nd vertical bending	19	0.036
4	3rd vertical bending	21.78	0.032
5	mixed	29.7	0.010
6	1st torsion	43.15	0.095
7	mixed	51.55	0.049
8	mixed	68.28	0.029
9	mixed	74.85	0.033
10	mixed	81.8	0.025
11	mixed	89.6	0.013
12	mixed	97.98	0.031

5.3 Fuselage/tail Testing

5.3.1 Experimental Set Up and Procedure

The modal characteristics of the fuselage structure are determined for a free-free configuration which is simulated by suspending the fuselage structure from the wing attachment points. Figure 5.13 shows the fuselage body mounted in the UTS.

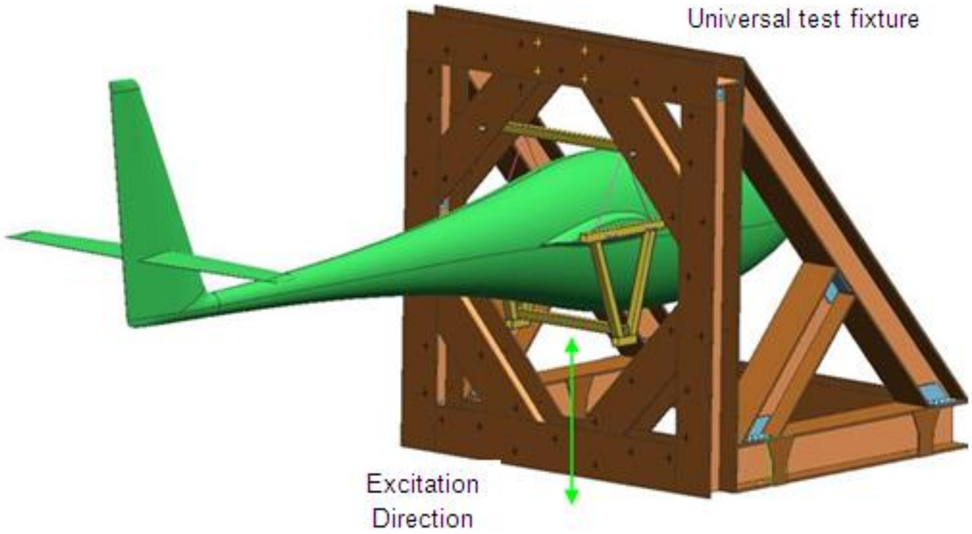

Figure 5.13

Fuselage vibration test set up

Designed to match the wing/ fuselage connection points, the test fixture is suspended from the support beam of the UTS by two large springs, which are connected to the fixture through turnbuckles as shown in Figure 5.14 The shaker system, which is centrally attached to the bottom member of the test fixture via a steel stinger rod, is used to induce vertical oscillations in the structure.

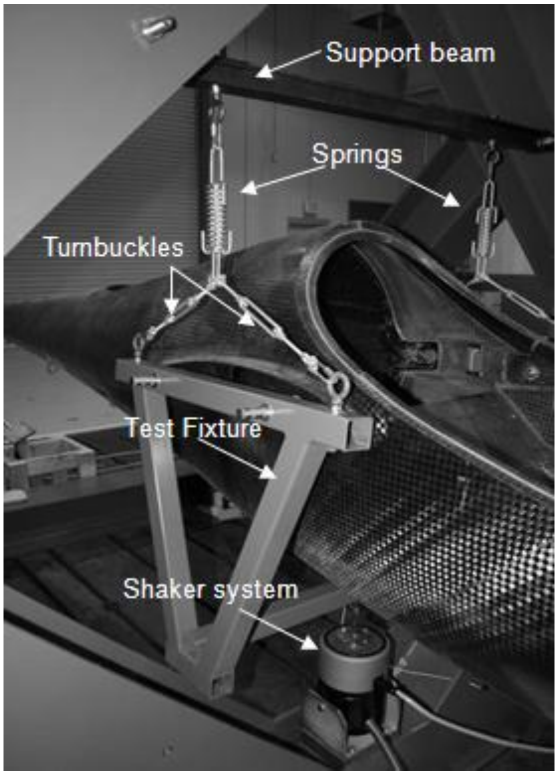

Figure 5.14

Fuselage vibration test fixture

The signal measurement system for the wing vibration testing was also utilized for the fuselage/tail structure, which was also instrumented with 19 dual axis accelerometers. In the wing vibration testing, the wing is essentially considered as a flat surface; therefore, the responses were obtained in the chordwise and in the normal directions. However, each accelerometer on the fuselage/tail structure has two axes of measurement direction (lateral, vertical up and down, or chordwise), which entirely depend on the accelerometer placement. Various sensor configurations were considered to ensure that the responses of the test structure were fully obtained. In the first configuration, shown in Figure 5.15, the first 11 sensors (A1-A11) were located along the bottom of the fuselage body, equidistantly spaced from nose to tail. The next four accelerometers (A12-A16) were mounted on the left aft side of the fuselage and the remaining three accelerometers (A17-A19) were mounted on the left side of the vertical tail. Vibration tests were also conducted for an additional three sensor configurations (Figure 5.15-5.18) to verify the modal data obtained from configuration #1. From the preliminary results, some of these sensors were relocated to the area of interest. For example, in sensor configuration #2 as shown in Figure 5.16, five accelerometers (A12-A16) were relocated to the horizontal tail, whereas accelerometers A1-A11 remained at the same location. To further obtain the responses from the aft fuselage and horizontal tail, the vibration tests were performed using sensor configuration #3 (Figure5.17) and sensor configuration #4 (Figure 5.18), respectively. While these figures only show the location of the sensors on the bottom and left side of structure, it is to be noted that the accelerometers which are underlined represent the mirror image location on the right side of the structure. For example, in Figure 5.17, A12 is located on the right side of the horizontal tail at the same location as A14. In each configuration, a total of 38 discrete-point accelerations are measured and recorded. The frequency sweeps from 5 Hz to 100 Hz were conducted at a sampling rate of 500 Hz.

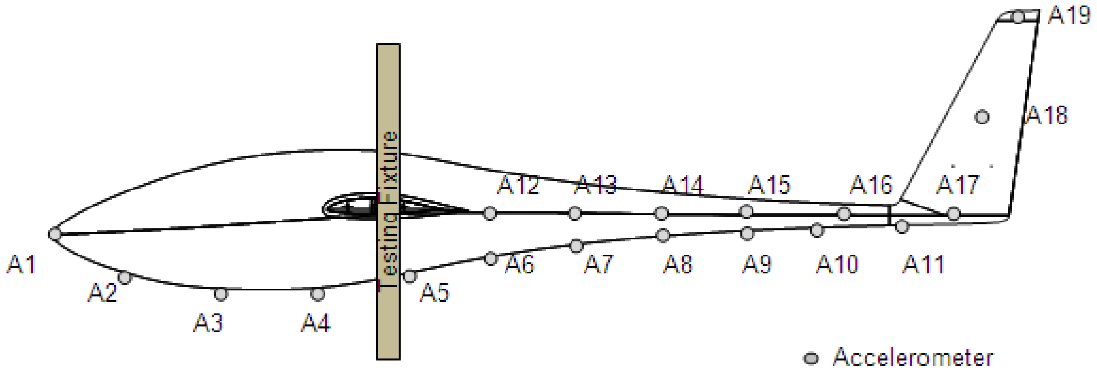
A19
A18
A12
A13
A14
A15
A16
A17
Testing Fixture
A1
A2
A3
A4
A5
A6
A7
A8
A9
A10
A11
Accelerometer

Figure 5.15

Fuselage vibration testing configuration #1

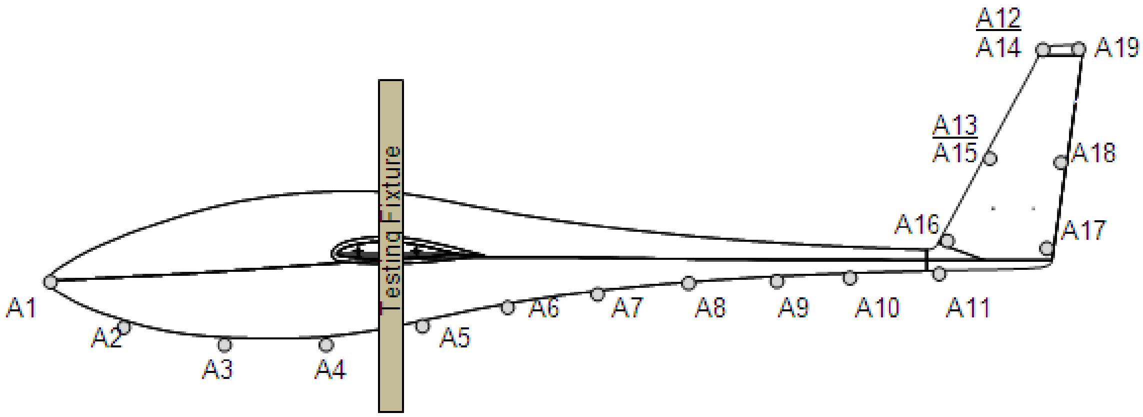
A12
A14
A19
A13
A15
A18
A16
A17
Testing Fixture
A1
A2
A3
A4
A5
A6
A7
A8
A9
A10
A11

Figure 5.16

Fuselage vibration testing configuration #2

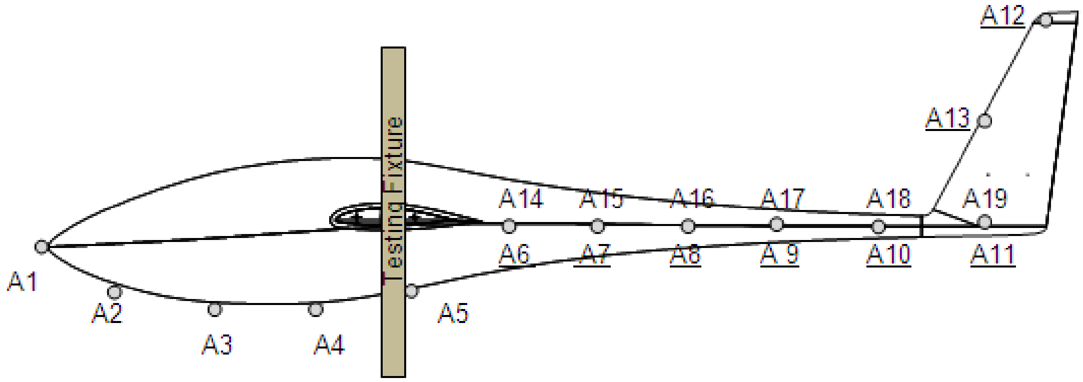
A12
A13
Testing Fixture
A14
A15
A16
A17
A18
A19
A6
A7
A8
A 9
A10
A11
A1
A2
A3
A4
A5

Figure 5.17

Fuselage vibration testing configuration #3

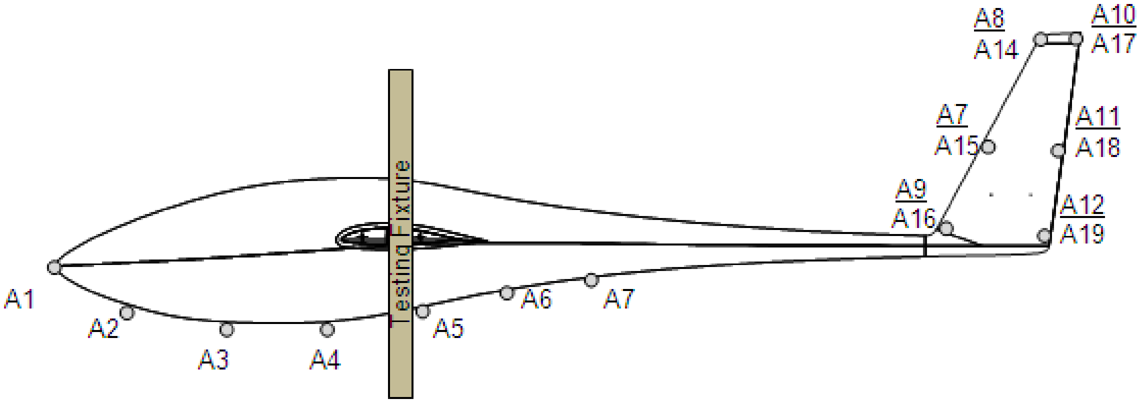
A8
A14
A10
A17
A7
A15
A11
A18
A9
A16
A12
A19
Testing Fixture
A1
A2
A3
A4
A5
A6
A7

Figure 5.18

Fuselage vibration testing configuration #4

5.3.2 Results and Discussion

The acceleration data from all sensors and configurations is analyzed and the frequency response functions are computed by using the spectrum of the input (applied force) and output signals (acceleration). Figure 5.19 shows the FRF of accelerometer

A19, which is located at the tip of the vertical stabilizer (see Figure 5.6). Similar FRF plots for all accelerometers were computed and the magnitude and direction at each resonant frequency was determined to obtain the mode shape associated with each natural frequency.

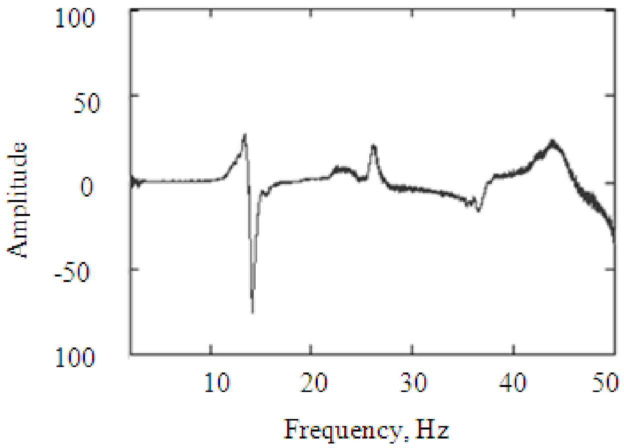

Figure 5.19

Frequency response function of accelerometer A19

Although frequency sweeps are conducted in the range of 3 Hz to 100 Hz, only data up to 50 Hz is shown as there are no resonant frequencies that appear in the 50 Hz to 100 Hz range. In the figures depicting the modal data, the coordinate system shown in Figure 5.20 is used. The two axes of measurement for the accelerometers on the bottom of the fuselage (A1-A11) are the x-axis (lateral) and the y-axis (vertical/ up-down), whereas the two axes of measurement for accelerometers on the left aft side of the fuselage (A12-A16) are the x-axis (lateral) and z –axis (longitudinal) and for the accelerometers on the tail (A17-A19), the lateral axis is represented by the x-axis and the chordwise (in-plane) direction is described by the z-axis.

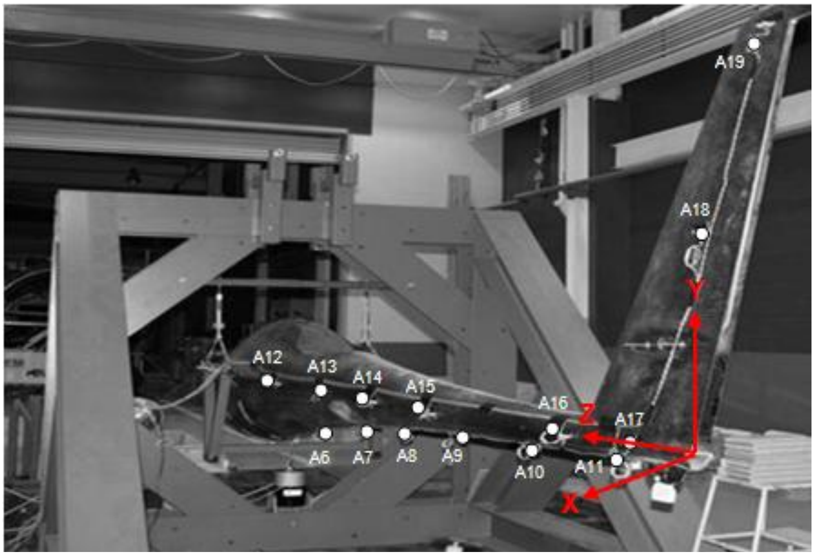

Figure 5.20

Displacement direction of the test structure

Figures 5.21a and 5.21b show the frequency spectrums computed from the acceleration data for accelerometers A1, A8 and A10, in the x and y-directions, respectively. As can be seen from both figures, all three sensors depict most of the same natural frequencies but with varying amplitudes. Again, the presence of resonant frequencies in both axes indicates a combination of modes. For example, the amplitude at the first resonant frequency of 13.5 Hz is greatly diminished in the y direction when compared to the x-direction which is indicative of the predominance of a lateral bending mode simultaneously with slight vertical bending. Conversely, at 25.4 Hz, the amplitude of the data in the y-direction is much larger, which indicates the predominance of a vertical bending mode.

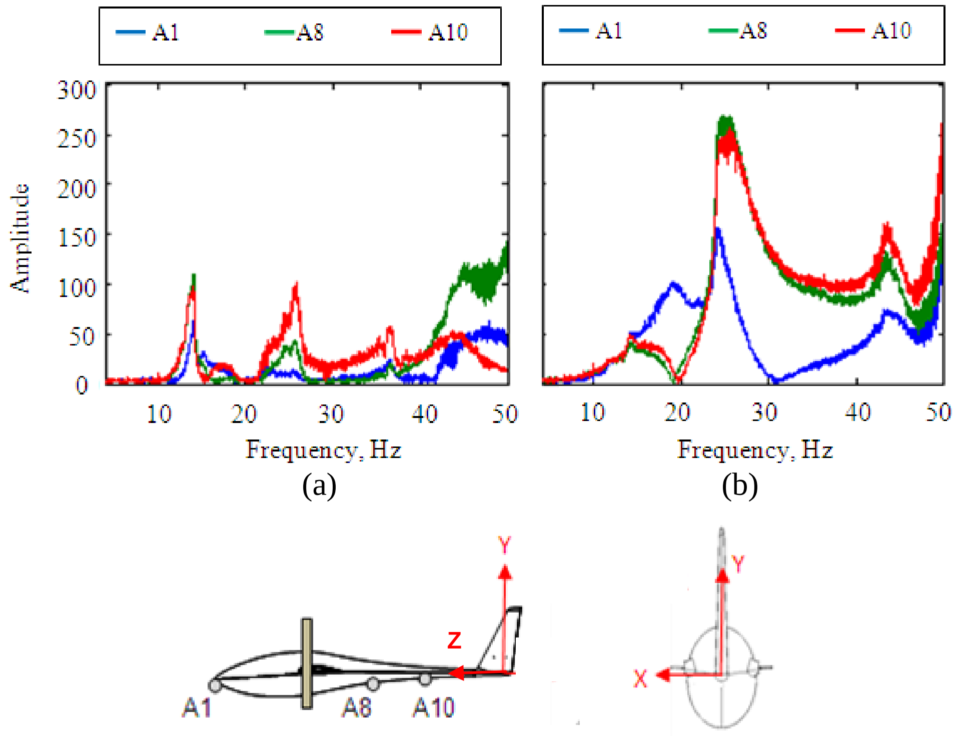

(a)

(b)

(c)

Figure 5.21

Frequency spectrums for A1, A8, and A10 in the (a) x-direction and (b) y- direction using (c) the coordinate system

Figures 5.22a and 5.22b show the frequency spectrums for the x and z directions for accelerometers A14 and A16. These accelerometers are located on the aft side of the fuselage. Minimal response is obtained from the out-of-plane (x-axis) channels (Figure 5.22a), but in the z-direction (Figure 5.22b), which is the longitudinal axis of the fuselage, the spectrums show small amplitude peaks at all the natural frequencies.

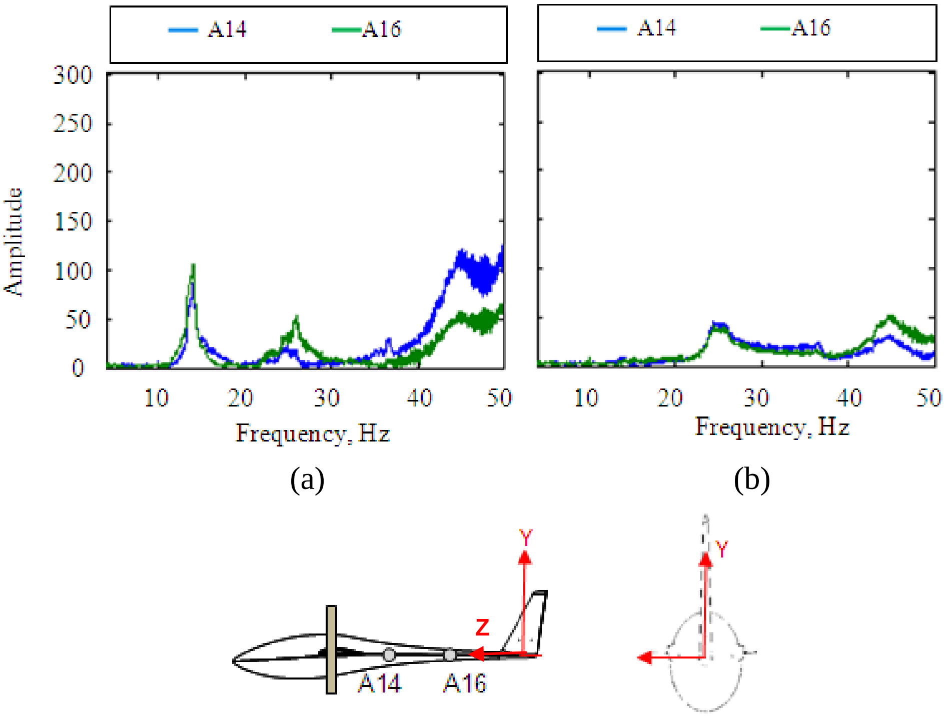

(a) (b)

(c)

Figure 5.22

Frequency spectrums of A14 and A16 in the (a) x-direction and (b) z- direction using (c) the coordinate system

The frequency spectrums in the x and z directions for accelerometers A17, A18, A19, located on the left side of the vertical stabilizer, are shown in Figures 5.23a and 5.23b, respectively. As expected, amplitudes at the resonant frequencies on the vertical stabilizer are much larger in magnitude than those obtained from the fuselage body. It is seen that although the first natural frequency of 13.5 Hz appears in both directions, the peak amplitude in the x –direction is much larger than the amplitude in the z –direction, indicating lateral bending of the tail as the predominant mode, which is clearly observed during test. It is also noted that the second peak at approximately 25 Hz is significant in the z-direction, indicating a chordwise motion, which is also visible during testing. Figures 5.23a and 5.23b also show the minimal response of A17, which is expected since it is located at the root of the vertical stabilizer.

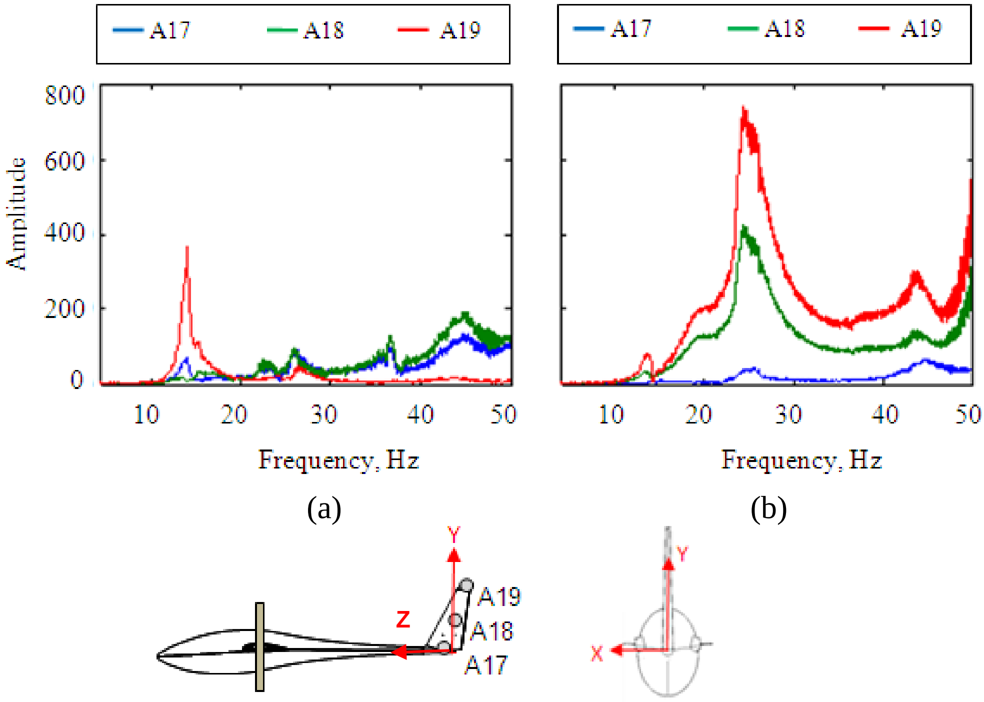

(a)

(b)

(c)

Figure 5.23

Frequency spectrums of A17, A18, and A19 in (a) x direction and (b) z-direction using (c) the coordinate system

The resulting mode shapes at 13.5 Hz, 24.6 Hz, 36.3 Hz and 45.2 Hz are shown in Figure 5.24. The lateral bending of the tail at the first frequency as well as the chordwise motion at the second frequency is evident from these figures. As expected, due to the complex geometry of the structure, all vibration modes are mixed modes having some combination of bending and torsion.

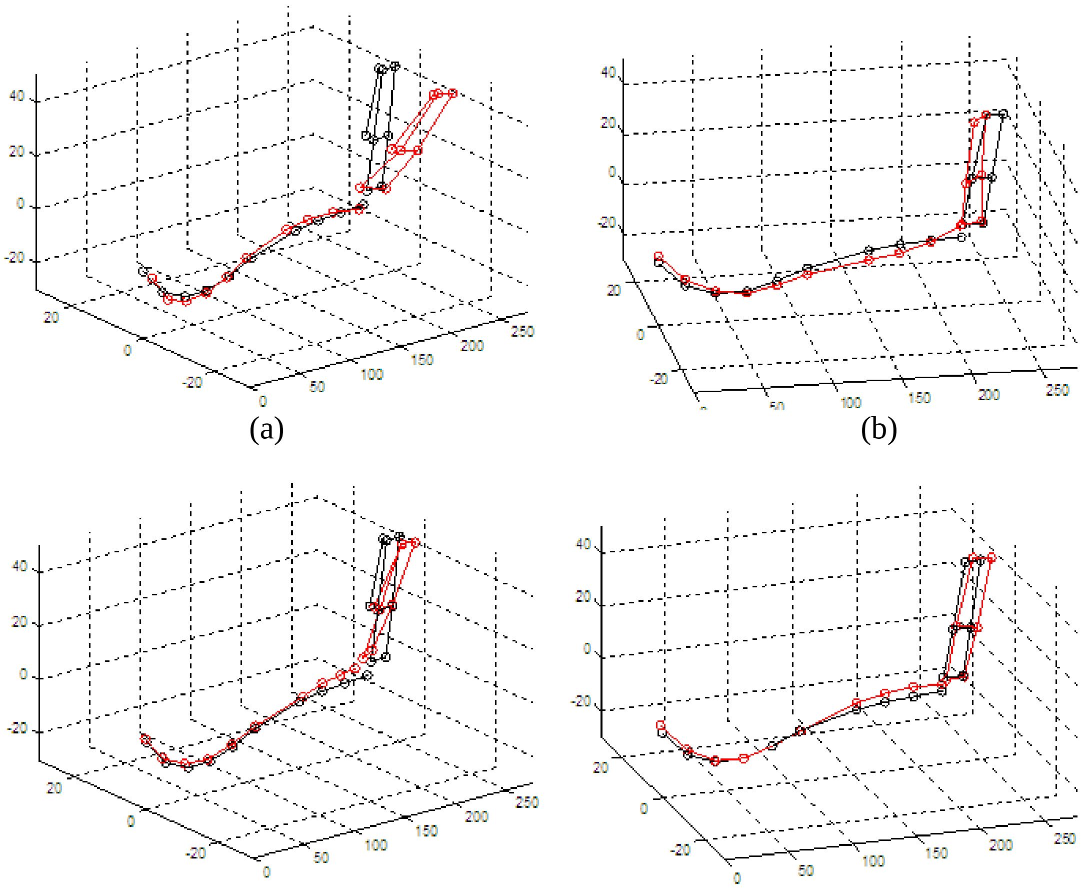

(a) (b)

(c) (d)

Figure 5.24

Red-mode shape at (a) 13.5 Hz (b) 24.6 Hz (c) 36.3 Hz (d) 45.4 Hz
Black-mode shape at 0 Hz

Table 5.7 summarizes the modal characteristics (resonant frequencies, mode shapes, and associated damping ratios) of the fuselage/tail structure obtained from the

FRFs of each sensor channel. All data was post–processed using Mathcad and MATLAB programs.

Table 5.7

Vibration characteristics and observed mode shape of fuselage/tail structure

Mode No.	Natural Frequency	Damping Coefficient	Observed Primary Mode
1	13.5 Hz	0.07	Lateral bending
2	24.6 Hz	0.04	Vertical tail - chordwise bending Fuselage - vertical bending
3	26.1 Hz	0.15	Lateral bending
4	36.3 Hz	0.21	Vertical tail - lateral bending Fuselage - vertical bending
5	45.4 Hz	0.17	Vertical tail - lateral bending Fuselage - vertical bending

CHAPTER 6

CONCLUSIONS

In this study, the results of an investigation examining the static and vibration characteristics of carbon composite wing and fuselage/tail structures of an ultralight UAV are presented. A whiffletree system proved effective in loading the wing structure with a distribution based on a high-g pull-up maneuver condition. The use of tail loading fixture to simulate the combination of symmetric and unsymmetric loadings during various flight maneuvers was relative simple to design and implement. The load-deflection and load-strain data were collected using a computerized data acquisition system and examined. The responses from the right and left wings were generally consistent with most deviation being in the fore spar at GS1. The wing is found to be very stiff and strong, with the structure supporting more than forty times its weight at the point of failure. From the fuselage/ tail structure testing, the static measurements from the pull-down and push-up loadings were found to be in good agreement for most part, with the greatest discrepancy appearing in the GS2.

A shaker-table approach was used for wing vibration testing, whereas the fuselage/tail structure was mounted in a free-free configuration and vertically excited. Both approaches provided a simple and reliable method for excitation of the structures with minimal shaker force requirement. The placement of dual-axis accelerometers enabled the measurement of acceleration in in-plane and out-of-plane direction. Using the swept sine technique, g load data were obtained for a range of desired frequencies. FRFs were computed to determine the resonant frequencies and the associated mode shapes and damping coefficients. The vibration methodology presented here proved to be a simple and effective procedure from which the modal characteristics of large structures are determined.

REFERENCES

[1] L. Dickerson, "UAVs on the Rise," in *Aviation Week and Space Technology*. vol. 166 New York: McGraw-Hill Companies, 2007, pp. 114-116.

[2] K. Stewart, J. Wagener, G. Abate, and M. Salichon, "Design of the Air Force Research Laboratory Micro Aerial Vehicle Research Configuration," Reston, VA 20191-4344, United States, 2007, pp. 8086-8097.

[3] E. M. Cardenas, P. J. Boschetti, A. Amerio, and C. D. Velasquez, "Design of an Unmanned Aerial Vehicle for Ecological Conservation," Reston, VA 20191-4344, United States, 2005, pp. 1309-1318.

[4] R. Sullivan, M. Rais-Rohani, T. Lacy, and N. Alday, "Structural Testing of An Ultralight UAV Composite Wing," in *Proceedings of the 47th AIAA/ASME/ASCE/AHS/ASC Structures, Structural Dynamics, and Materials Conference*, Newport, RI, 2006.

[5] T. R. Robert, "A History of Structural Testing: Instruments and Devices, Methods and Techniques," *Experimental Techniques,* vol. 14, pp. 24-26, 1990.

[6] H. W. Smith, "Static Test of an Ultralight Airplane," *Journal of Aircraft,* vol. 25, pp. 37-40, 1988.

[7] S. F. Ma and T. K. Shiue, "Aircraft Airworthiness Certification: Static Bench Testing of an Airfoil Elevator," *Experimental Techniques,* vol. 27, pp. 32-35, 2003.

[8] M. J. D'Costa and F. M. Bartlett, "Design of a Static-equivalent Wind-load Test for a Full Scale Corrugated Fibreboard Shelter," Montreal, H3H 2R9, Canada, 2000, p. 213.

[9] J. Paquette, J. Van Dam, and S. Hughes, "Structural Testing of 9 m Carbon Fiber Wind Turbine Research Blades," Reston, VA 20191-4344, United States, 2007, pp. 9922-9932.

[10] J. B. Kosmatka and A. Valdes, "Development and Testing of the Extended Composite Wing for the Hunter UAV," Reston, VA 20191-4344, United States, 2007, pp. 4500-4509.

[11] H. T. Wong, J. G. Teng, and Z. C. Wang, "A Pulley-S system for the Simulation of Distributed Loading on Shell Roof Structures," *Experimental Techniques*, vol. 27, pp. 21-27, 2003.

[12] S. M. Belotserkovskii, *The Theory of Thin Wings in Subsonic Flow*. New York: Plenum Press, 1967.

[13] D. L. Brown and R. J. Allemang, "The Modern Era of Experimental Modal Analysis," *Sound and Vibration*, vol. 41, p. 16, 2007.

[14] R. E. D. Bishop and G. M. L. Gladwell, "An Investigation into the Theory of Resonance Testing," *Philosophical Transactions of the Royal Society of London. Series A, Mathematical and Physical Sciences (1934-1990)*, vol. 255, pp. 241-280, 1963.

[15] C. C. Kennedy and C. D. P. Pancu, "Use of Vectors in Vibration Measurement and Analysis," *Journal of the Aeronautical Sciences*, vol. 14, pp. 603-625, 1947.

[16] R. J. Allemang, D. L. Brown, and L. Air Force Flight Dynamics, *Experimental Modal Analysis and Dynamic Component Synthesis*: Flight Dynamics Laboratory, Air Force Wright Aeronautical Laboratories, Air Force Systems Command, 1987.

[17] M. Kehoe, "Aircraft ground vibration testing at the NASA Dryden Flight Reseach Facility-1993," 1994.

[18] W. G. Halvorsen and D. L. Brown, "ImpulseTechnique for Structural Frequency Response Testing," *Sound and Vibration*, vol. 11, pp. 8-21, 1977.

[19] R. W. Sullivan, Y. Hwang, M. Rais-Rohani, and T. Lacy, "Structure Analysis and Testing of an Ultralight UAV Carbon Composite Wing," *Sumitted for the Journal of Aircraft*, 2009.

[20] F. De Florio, *Airworthiness: An Introduction to Aircraft Certification; A Guide to Understanding Jaa, Easa and FAA Standards*: Butterworth-Heinemann, 2006.

[21] J. M. Gere and S. P. Timoshenko, *Mechanics of Materials*: Brooks/cole London, 2004.

[22] P. Avitabile, "Experimental Modal Analysis – A Simple Non-Mathematical Presentation," *Sound and Vibration*, 2001.

[23] T. Irvine, "The Steady-state Response of a Single-degree-of-freedom System Subjected to a Harmonic Force," Vibrationdata.com Publications, 1990.

[24] S. Rao, *Mechanical Vibrations*, 4th ed. New Jersey: Prentice Hall, 2003.

[25] W. T. Thomson and M. Dahleh, *Theory of Vibration with Applications*, 4th ed. New Jersey: Prentice Hall, 1993.

APPENDIX A

APPARATUS

Table A.1: Static testing apparatus

Item	Quality	Manufacturer	Model Number	Serial Number	Capacity	Notes
Power Supply	1	DC Tracking Power Supply	LPS152	5030091	120V 50/60 Hz	-
Load Cell	2	Interface	1210 AF–10K	-	10,000 lb.	Tension or compression
Digital Voltmeter	1	Fluke	Fluke 83		-	-
Data Acquisition Board	1	National Instruments	NI-PCI-6225, M Series	779295-01	-	80 Channels
Load Actuator	2	Enerpac	SPH 235 P 84N	-	8 Ton	-
cable-extension position transducers	6	Celesco	PT1DC 3	-	-	-
Signal Conditioning	3	Analog Devices	3D Series Signal Subsystem	-		-
Signal Conditioning	2	Dataforth	SCMPB01	14886-7 14886-9	-	-
Strain Gauge Input	25	Analog Devices	3B 18-000 WB	-	-	exc 10 V. 3.3V
Strain Gauge Input	34	Dataforth	SCM 5B38	-	-	exc 3.3 V @ 10mv/v

Table A.2: Vibration testing apparatus

Item	Quality	Manufacturer	Model Number	Serial Number	Capacity	Notes
Signal Generator	1	Agilent	33220A	MY44010728	20MHz	Function/Arbitrary Waveform Generator
Linear Power Amplifier	1	Vibration Research Corporation	PA-141	FS-140-486	-	Linear Power Amplifier
Electrodynamics Shaker	1	Vibration Research Corporation	ET-140	286	110 lbs	-
Accelerometer	20	Analog Devices, Inc.	ADXL 321EB	-	±18 g	Dual Axis Micromachined
Load Cell	1	Interface	1210 AF–10K	-	10,000 lb.	Tension or compression
Digital Voltmeter	1	Fluke	Fluke 83		-	-
Power Supply	1	DC Tracking Power Supply	LPS152	5030091	120V 50/60 Hz	-
Data Acquisition Board	1	National Instruments	NI-PCI-6225, M Series	779295-01	-	80 Channels
Blower Assembly	1	Vibration Research Corporation	VR 12		-	-
Dynamic Force Sensor	1	PCB Piezotronics	208C02	25882	± 100 lbs	-
Signal Conditioning	1	PCB Piezotronics	482A21	1648	-	Single-channel, unity gain, line-powered

APPENDIX B

LABVIEW PROGRAM

Figure B.1: LabVIEW program for static testing of wing structure (front panel)

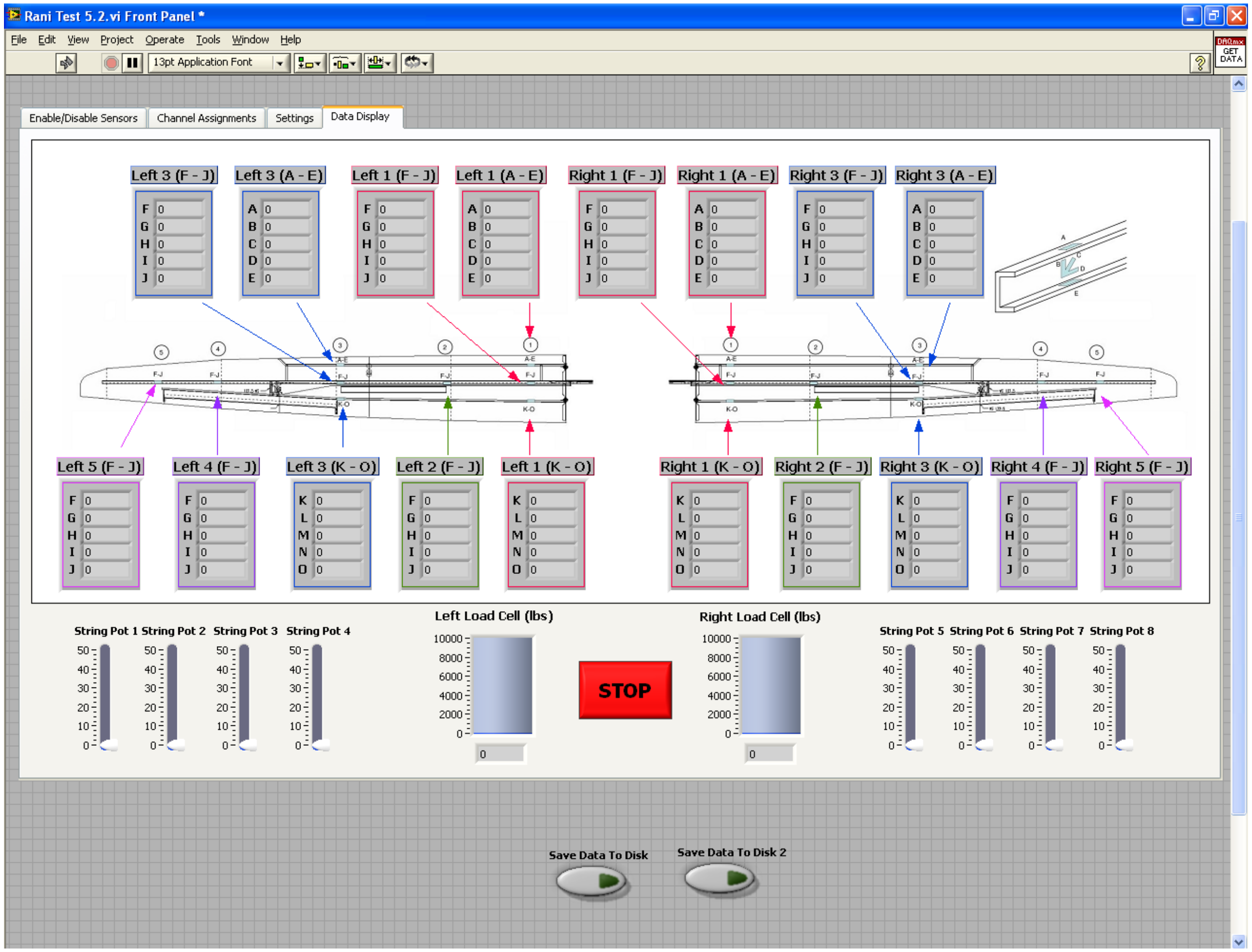
Rani Test 5.2.vi Front Panel *
File Edit View Project Operate Tools Window Help
13pt Application Font
GET DATA
Enable/Disable Sensors
Channel Assignments
Settings
Data Display
Left 3 (F - J)
Left 3 (A - E)
Left 1 (F - J)
Left 1 (A - E)
Right 1 (F - J)
Right 1 (A - E)
Right 3 (F - J)
Right 3 (A - E)
Left 5 (F - J)
Left 4 (F - J)
Left 3 (K - O)
Left 2 (F - J)
Left 1 (K - O)
Right 1 (K - O)
Right 2 (F - J)
Right 3 (K - O)
Right 4 (F - J)
Right 5 (F - J)
String Pot 1
String Pot 2
String Pot 3
String Pot 4
Left Load Cell (lbs)
STOP
Right Load Cell (lbs)
String Pot 5
String Pot 6
String Pot 7
String Pot 8
Save Data To Disk
Save Data To Disk 2

Figure B.2: LabVIEW program for static testing of fuselage structure (front panel)

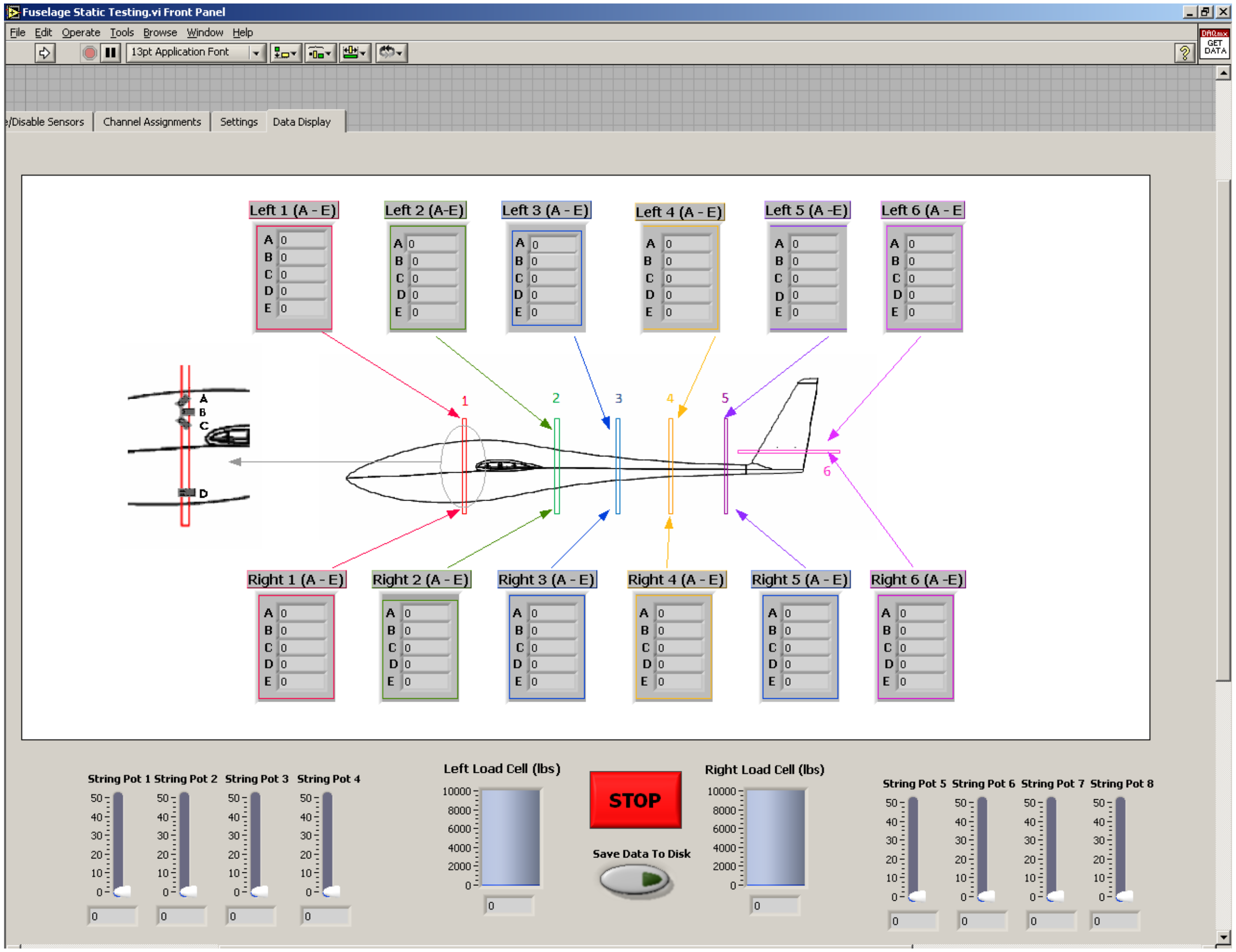
Fuselage Static Testing.vi Front Panel
File Edit Operate Tools Browse Window Help
13pt Application Font
GET DATA
/Disable Sensors
Channel Assignments
Settings
Data Display
Left 1 (A - E)
Left 2 (A-E)
Left 3 (A - E)
Left 4 (A - E)
Left 5 (A -E)
Left 6 (A - E
A B C D E
1 2 3 4 5 6
Right 1 (A - E)
Right 2 (A - E)
Right 3 (A - E)
Right 4 (A - E)
Right 5 (A - E)
Right 6 (A -E)
String Pot 1
String Pot 2
String Pot 3
String Pot 4
String Pot 5
String Pot 6
String Pot 7
String Pot 8
50 40 30 20 10 0
Left Load Cell (lbs)
Right Load Cell (lbs)
10000 8000 6000 4000 2000 0
STOP
Save Data To Disk

Figure B.3: LabVIEW program for static testing (block diagram)

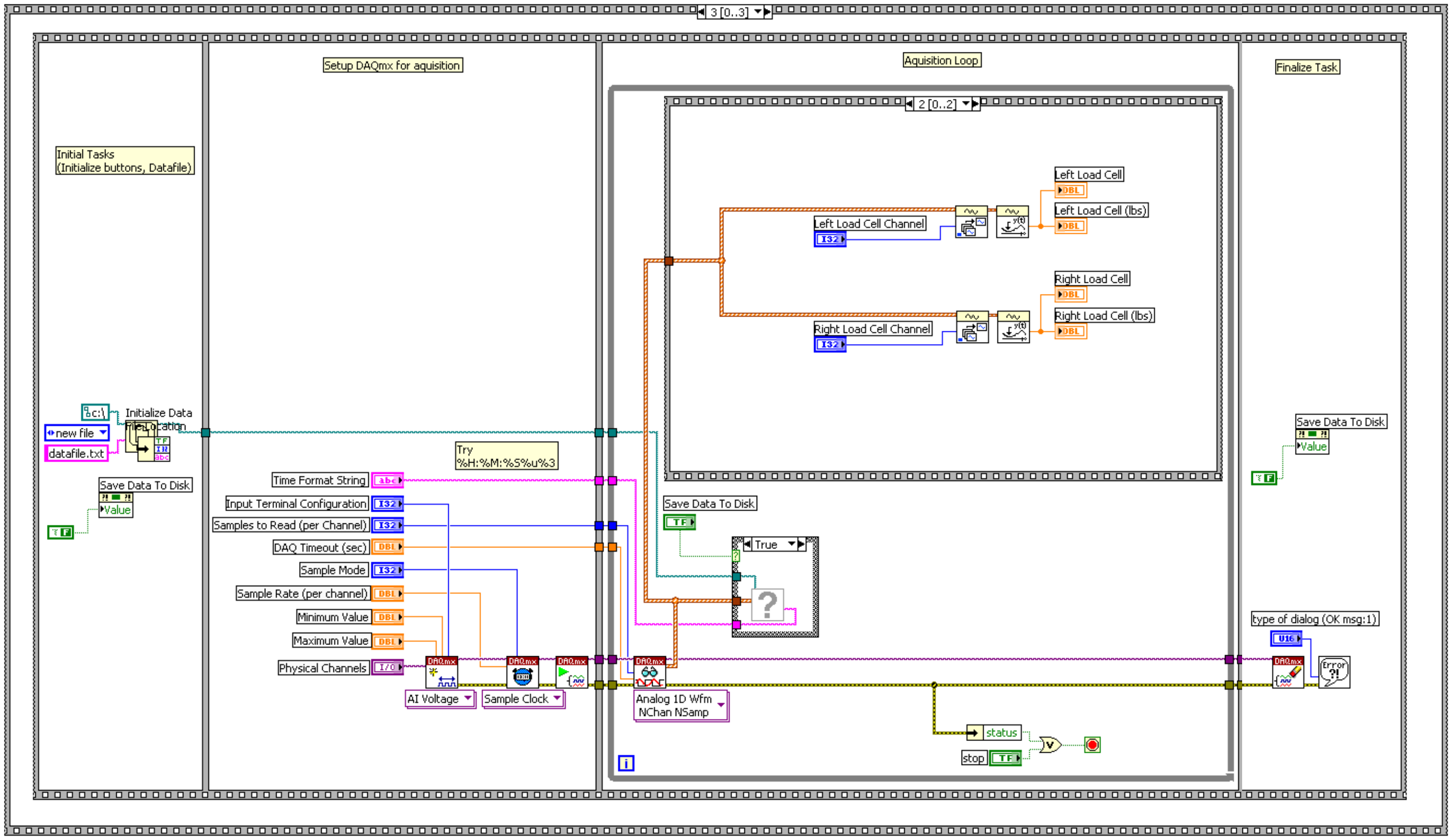

3 [0..3]
Initial Tasks (Initialize buttons, Datafile)
c:\
new file
datafile.txt
Initialize Data File Location
Save Data To Disk
Value
Setup DAQmx for aquisition
Try %H:%M:%S%u%3
Time Format String
Input Terminal Configuration
Samples to Read (per Channel)
DAQ Timeout (sec)
Sample Mode
Sample Rate (per channel)
Minimum Value
Maximum Value
Physical Channels
DAQmx
AI Voltage
Sample Clock
Aquisition Loop
2 [0..2]
Left Load Cell Channel
Left Load Cell
Left Load Cell (lbs)
Right Load Cell Channel
Right Load Cell
Right Load Cell (lbs)
Save Data To Disk
True
Analog 1D Wfm NChan NSamp
status
stop
i
Finalize Task
Save Data To Disk
Value
type of dialog (OK msg:1)
U16
Error ?!

Figure B.4: LabVIEW program for vibration testing (front panel)

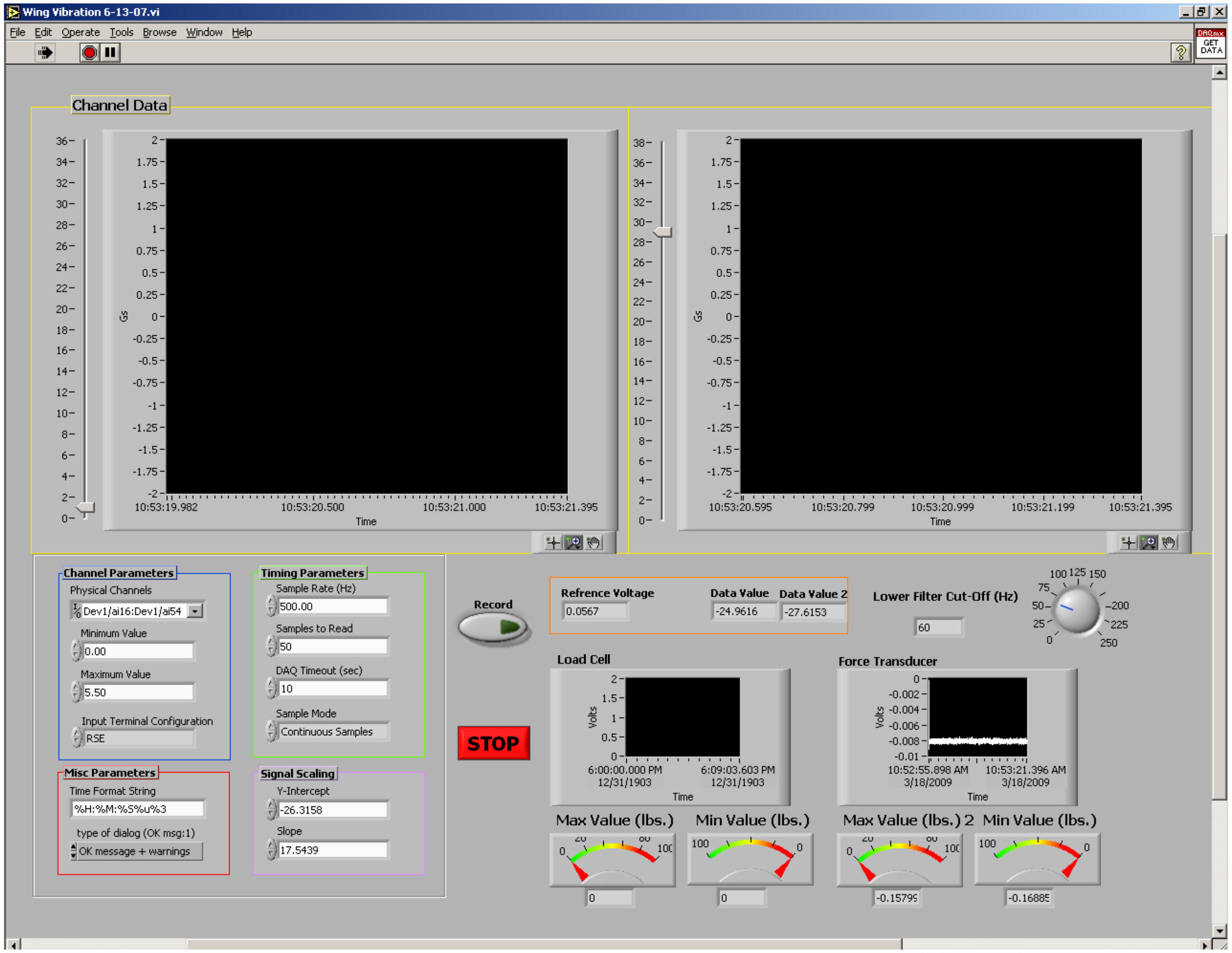
Wing Vibration 6-13-07.vi
File Edit Operate Tools Browse Window Help
GET DATA
Channel Data
Gs
Time
10:53:19.982
10:53:20.500
10:53:21.000
10:53:21.395
10:53:20.595
10:53:20.799
10:53:20.999
10:53:21.199
Record
STOP
Load Cell
Volts
6:00:00.000 PM 12/31/1903
6:09:03.603 PM 12/31/1903
Force Transducer
10:52:55.898 AM 3/18/2009
10:53:21.396 AM 3/18/2009
Max Value (lbs.)
Min Value (lbs.)
Max Value (lbs.) 2
Min Value (lbs.)

Channel Parameters
Physical Channels: Dev1/ai16:Dev1/ai54
Minimum Value: 0.00
Maximum Value: 5.50
Input Terminal Configuration: RSE

Timing Parameters
Sample Rate (Hz): 500.00
Samples to Read: 50
DAQ Timeout (sec): 10
Sample Mode: Continuous Samples

Misc Parameters
Time Format String: %H:%M:%S%u%3
type of dialog (OK msg:1): OK message + warnings

Signal Scaling
Y-Intercept: -26.3158
Slope: 17.5439

Refrence Voltage: 0.0567
Data Value: -24.9616
Data Value 2: -27.6153
Lower Filter Cut-Off (Hz): 60

Max Value (lbs.): 0
Min Value (lbs.): 0
Max Value (lbs.) 2: -0.15799
Min Value (lbs.): -0.16885

Figure B.5: LabVIEW program for vibration (block diagram)

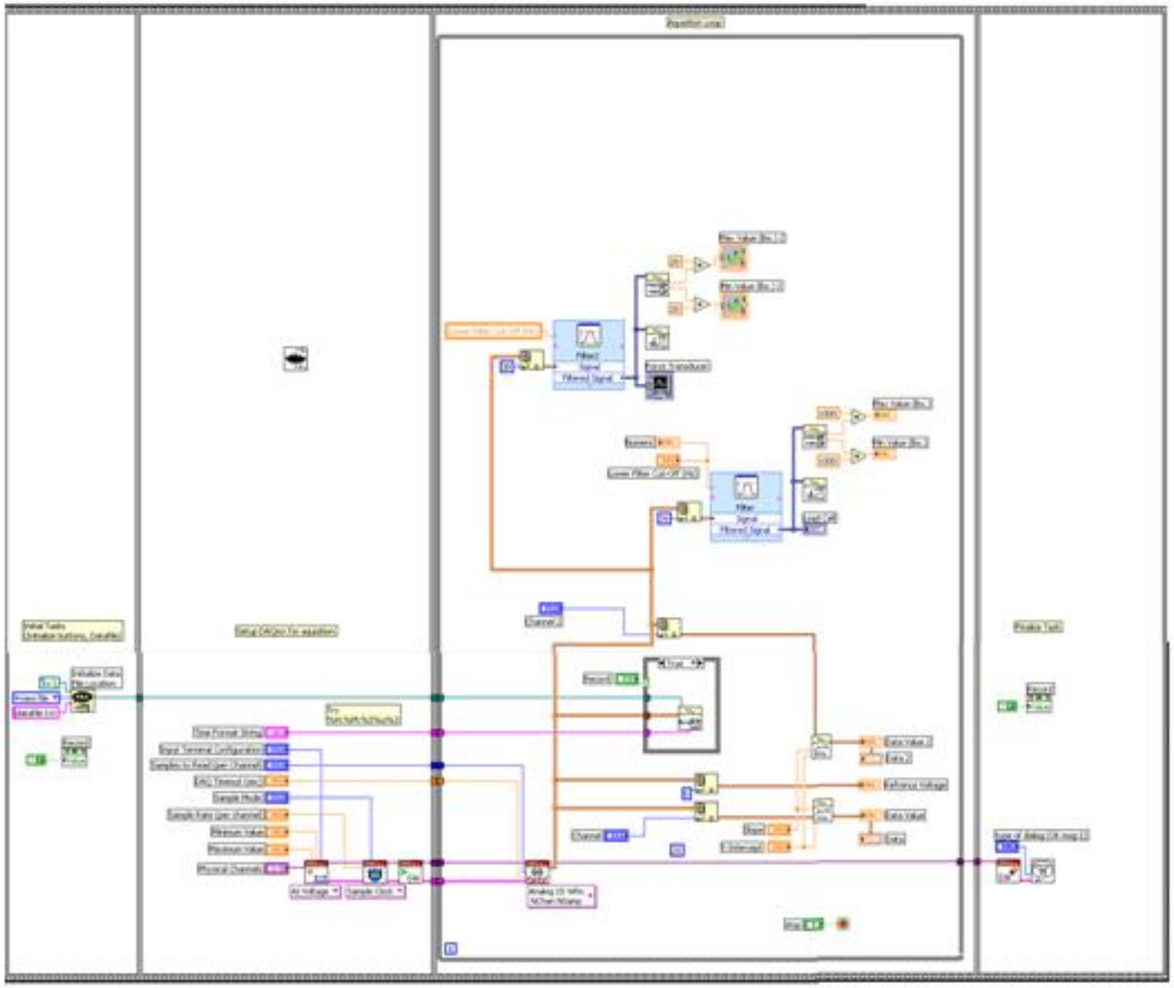

APPENDIX C

RESULTS FROM CHORDWISE VIBRATION TESTING OF WING STRUCTURE

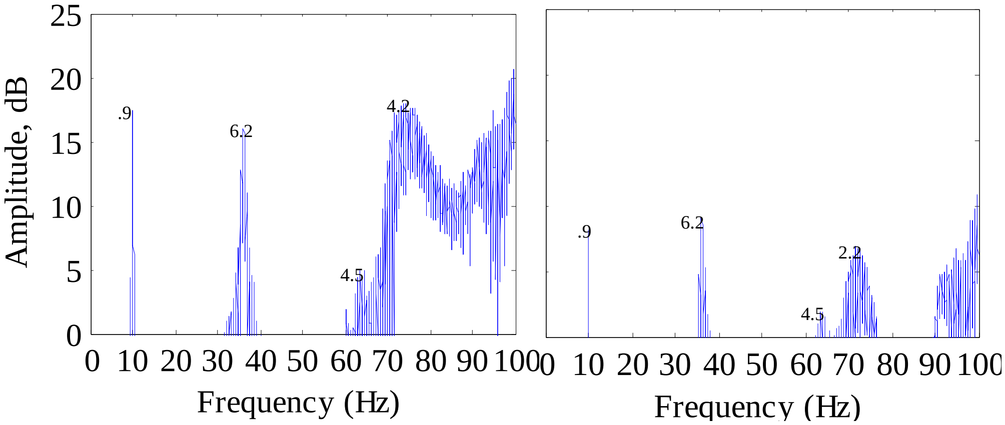

(a) (b)

Figure C.1: Frequency spectrum based on out-of-plane acceleration measurements at accelerometer location (a) A1 and (b) A5 of Wing #1

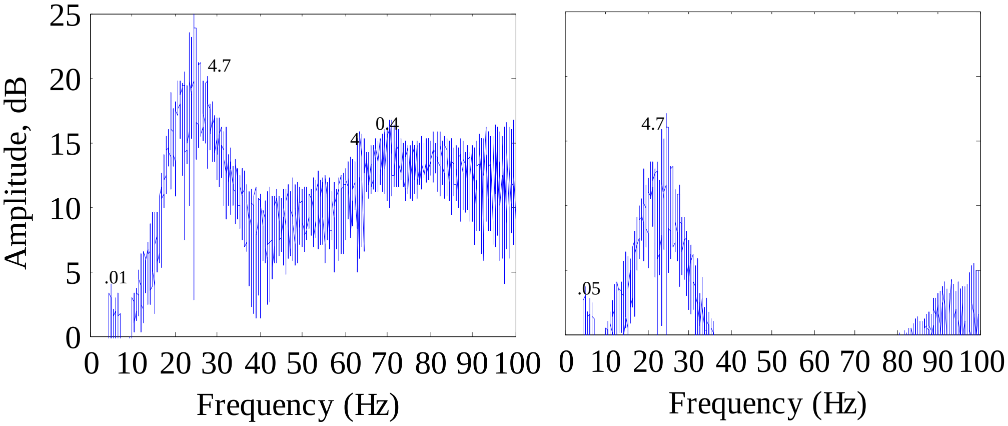

(a) (b)

Figure C.2: Frequency spectrum based on in-plane (chord-wise) acceleration measurements at accelerometer location (a) A1 and (b) A5 of Wing #1

Table C.1: List of peak frequencies of in-plane channels of Wing #1

Accelerometer #	**Peak Frequency (Hz)**			
1	5.02	24.68	64.03	70.35
2	5.07	24.67	63.95	70.80
3	5.02	24.68	63.78	71.25
4	5.02	24.68	63.62	70.80
5	5.05	24.67		
6	5.05	24.68		
7	4.98	24.68		
8	5.03	24.68		
9	5.08	24.67		
10	5.08			
11	5.03	24.68	63.95	70.80
12	4.98	24.68	63.53	70.80
13	5.12	24.68		
14	5.08	24.68		
15	4.98	24.68		
16	5.08	24.67		
17	5.02	19.12		
18	5.07	19.33		71.77

Table C.2: List of peak frequencies of out-of-plane channels of Wing #1

Accelerometer #	**Peak Frequency (Hz)**				
1	9.93		36.20	64.53	74.17
2	9.92	24.68	36.20	63.62	
3	9.92			64.37	73.82
4	9.92	24.68			
5	9.88		36.20	64.03	72.22
6	9.90		36.20		72.28
7			36.20		73.82
8			36.20		74.17
9	9.92		36.18		71.77
10					73.32
11	9.90		36.20		
12	9.93		36.20		
13	9.90		36.20	63.60	73.32
14	9.93		36.20		74.17
15	9.90		36.22		
16	9.90		36.22		
17					73.32
18					73.82

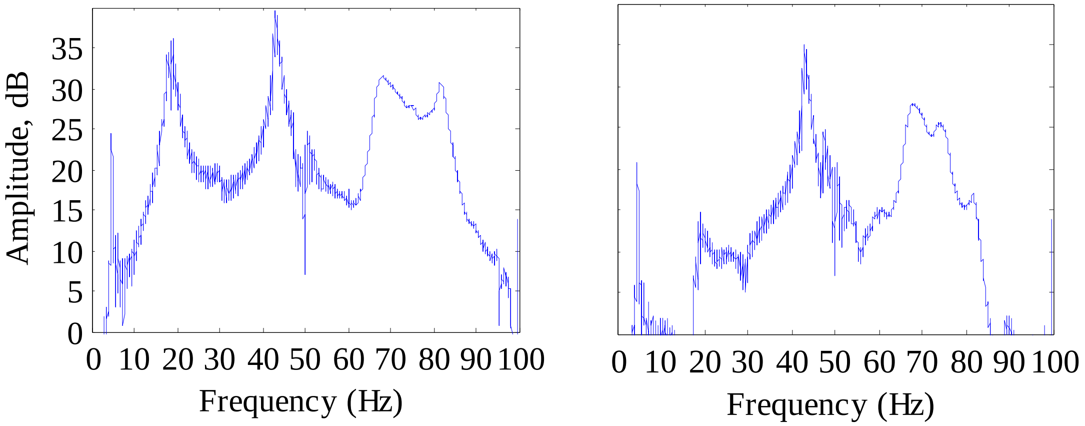

(a) (b)

Figure C.3: Frequency spectrum based on out-of-plane acceleration measurements at accelerometer location (a) A1 and (b) A5 of Wing # 2

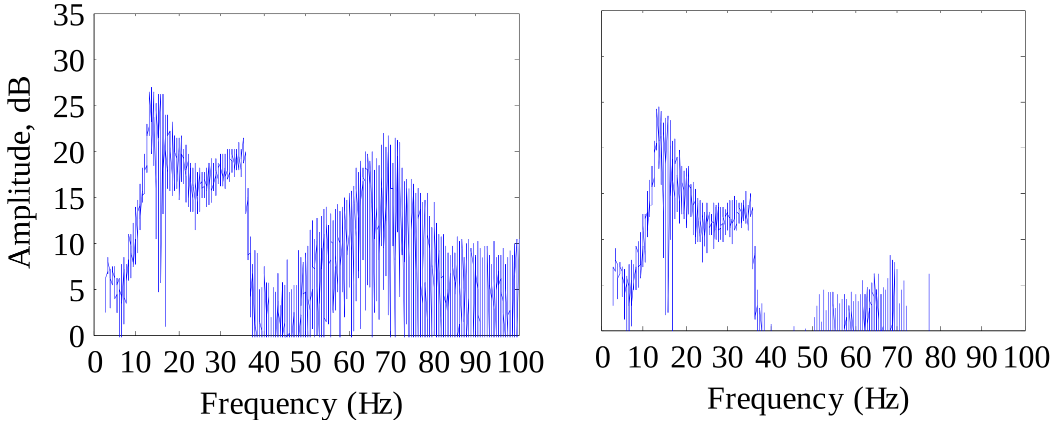

(a) (b)

Figure C.4: Frequency spectrum based on in-plane (chord-wise) acceleration measurements at accelerometer location (a) A1 and (b) A5 of Wing # 2

Table C.3: List of peak frequencies of in-plane channels of Wing #2

Accelerometer #	**Peak Frequency (Hz)**		
1	13.5	35.5	68.2
2	13.3	35.5	71.0
3	13.5	35.5	68.2
4	13.5	35.5	68.2
5	13.3	34.5	68.2
6	13.3	35.5	68.2
7	13.3		71.5
8	14.0		71.0
9	13.5		71.0
10	13.5		71.0
11	13.3		71.0
12	13.3		71.0
13	13.3	35.5	71.0
14	13.3	35.5	71.0
15	13.5	35.2	71.0
16	13.3	35.5	71.0
17	13.3	35.5	71.0
18	13.5	35.5	71.0

Table C.4: List of peak frequencies of out-of-plane channels of Wing #2

Accelerometer #	**Peak Frequency (Hz)**			
1	6.4	23.0	48.3	70.2
2	6.4	23.0	47.3	69.7
3	6.4	23.0		69.7
4	6.4	23.0		70.2
5	6.4		48.3	68.2
6	6.4		48.3	70.2
7	6.4	23.0	47.3	69.7
8	6.4	23.0	47.3	70.2
9	6.4	23.0		70.2
10	6.4	23.0		70.2
11	6.4	23.0		70.2
12	6.4	23.0		
13	6.4	23.0	47.3	70.2
14	6.4	23.0		
15		23.0	48.3	70.2
16		23.0		
17				70.2
18				70.2